March 6, 2018

UTRECHT UNIVERSITY

Msc THESIS

A journey through two-dimensional subduction modelling

by

Janneke de Laat[1]

3830888

Supervisors:
Dr. Cedric Thieulot[1]
Prof. dr. Wim Spakman[1]

1: Utrecht University, Department of Geosciences,
Group of Mantle dynamics & theoretical geophysics

The Netherlands

Abstract

In this research we aim to reconstruct a fully functioning numerical model that can represent the evolution of the South Sandwich Trench from its initiation 80 Myr to its present day position. To do so we constructed a two-dimensional numerical model in the finite element code ELEFANT. We constructed a visco-plastic subduction model constraining a viscosity field based on the flow laws of the dominant deformation mechanisms in the lithosphere and mantle: diffusion creep, dislocation creep and Peierls creep. To represent brittle or plastic yielding we implemented Byrelees law. This research is divided into two sections. In section 1 an intra-oceanic subduction zone is constructed, tuning the viscosity parameters and implementing a plate velocity. Rollback and subduction was observed by the formation of a ridge in both the subducting plate (SP) and overriding plate (OP). In section 2 a setup similar to the South-Sandwich Trench was implemented. As the OP is continental, the plates had to decouple for subduction to evolve as no ridge could form in the OP. When decoupled, the SP could freely subduct and roll back. The limited decoupling between the SP and the surface however prevented the slab from rolling back further than maximal 250 km. Further subduction was only possible through the input of a plate velocity. However, together with the fact that the upper-lower mantle (ULM) boundary was deformable, the obstruction of trench motion caused cessation of the subduction and instabilities at the surface. To further confine this model and create a numerical model that can represent the evolution of the South-Sandwich trench, two main problems remain to be fixed: the SP should be able to decouple further at the surface so the trench is free to move, and the ULM boundary should become underformable and semipermeable, as observed by geophysical observations.

Contents

1 Introduction

The subduction of a negatively buoyant lithospheric plate beneath an overriding plate is one of the key processes in the cycle of plate tectonics. It concerns lithospheric plates sinking into the underlying mantle, showing that plate tectonics in an integral part of global mantle dynamics. Since the theory of plate tectonics was first presented, much research has been done concerning the dynamics of subduction, either by observations or laboratory and numerical experiments. Here, I first briefly review main aspect of subduction and subduction modelling and then focus on the main target of my research which is to investigate in 2D geometry the effects of plate motions on subduction evolution motivated by the natural example of the South-Sandwich subduction evolution.

1.1 Subduction evolution

The evolution of subduction is strongly dependent on the balance between the driving forces and the resisting forces (e.g., Billen, 2008). The driving forces include the slab pull due to the negatively buoyant slab and and surface motion of the subducting and overriding plates. The resisting forces include the drag of the mantle and the resistance at the boundary between the overriding plate and subducting plate (Hall et al., 2003, Gurnis et al., 2004, Billen, 2008). This zone is known as the shear zone. If the driving forces can overcome the resisting forces, subduction can evolve. The kinematic responses to these forces are largely determined by the rheology of the lithospheric plates and the mantle, and the plate motions. In recent literature, the evolution subduction can be divided into three phases:
1) The initiation of subduction, where the slab tip starts sinking into the mantle. There are two contrasting theories on how subduction can initiate: spontaneous subduction, where the negative buoyancy of the plate is enough to overcome the resisting forces and cause the slab to sink (Stern and Bloomer, 1992, Turcotte et al., 1977), and forced subduction, where an external force is needed to overcome the resisting forces (McKenzie, 1977, Toth and Gurnis, 1998).
2) the transient period, where the subduction is continuing and eventually the slab starts to interact with the 660 km upper-lower mantle (ULM) boundary.
3) the long-term subduction, where a particular mode of subduction emerges and it remains stable (Stegman et al., 2010). Particular modes of subduction have recently also been described for the transient period by Garel et al. (2014) and may also influence which mode will develop in phase three.

By three-dimensional fluid dynamic laboratory simulations Schellart (2008) observed 5 different modes of subduction. These were confirmed by three-dimensional numerical models of Stegman et al. (2010). The regimes are classified based on slab strength (both the viscosity of the slab and the thickness) and buoyancy of a freely sinking slab with the absence of an overriding plate (Figure 1). Also the influence of the lower mantle is limited as this is either absent (Schellart, 2008) or impermeable (Stegman et al., 2010).

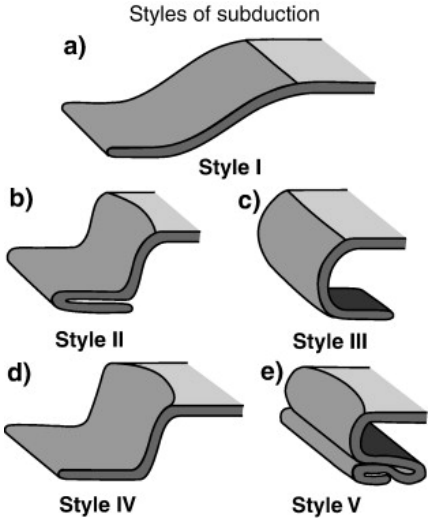

Figure 1: Subduction regimes as obtained by Schellart (2008).

Garel et al. (2014) reevaluated these regimes with numerically model various modes of subduction in the presence of an oceanic OP of varying age and and a lower mantle with increased viscosity. Combining these experiments leads to the following subduction styles:
1) Viscous Beam Mode (VBM)/Inclined-strong retreat (ISR): Rapid sinking and continuing trench retreat, leading to an inclined slab, partially flattening on ULM boundary causing a draped geometry. Trench retreat slows down when the slab hits the lower mantle and characterized by OP extension. This mode is observed slabs with large flexural stiffness in Stegman et al. (2010) and for old SP (> 60 Ma) and young OP (< 40 Ma) in Garel et al. (2014).
2) Advance-fold-retreat mode (AFR)/Bent then inclined and retreat (BIR): Low sinking and retreat rate approaching the 660 boundary with a rolled-over shape. Interaction with the boundary causes unbending through trench retreat resulting in an inclined slab. Characterized by episodic trench migration. Observed for observed for heavy, strong slabs by Stegman et al. (2010) and old SP and OPs (both > 60 Ma).
3) Advancing mode (AM): the trench advances and the slab forms a rollover geometry. This mode is observed for strong slabs. This mode is not observed by Garel et al. (2014) with the presence of an OP and is not observed at present time on Earth (Schellart, 2008).
4) Retreating mode (RM)/Horizontally deflected slabs (HD): steep initial descend of the slab followed by flattening at the ULM boundary creating a backwards draping slab morphology. Exhibit mild trench retreat and is observed for young SPs (<40 Ma) and OPs (<60 Ma) by Garel et al. (2014) and for heavy, weak slabs by Stegman et al. (2010).
5) Folding mode (FM)/Vertical folding (VF): slow sub-vertical sinking through the UM, folding on top of the lower man-

tle. A quasi-stationary trench is observed throughout. Is observed for very young (< 40 Ma, Garel et al., 2014)/ weak (Stegman et al., 2010) subducting plates.

Although the various experiments agree with these 5 different regimes, these regimes are purely experimentally obtained and do not fully represent the complex subduction zones observed today on earth. This is partly due to the simplifications and assumptions made when constructing a numerical model. For example, the influence of a continental overriding plate, which is common in natural situations, is absence in these regimes. Also these styles of subduction have been observed experimentally for freely moving plates for which slab pull is the main driver of subduction. This is not the case on Earth where plate motion is also governed by remote forces (Forsyth and Uyeda, 1975). It is thus of great importance to fully understand the interaction between tectonic plates and mantle and slab dynamics for the various variations of natural subduction found on Earth. Equally, it is important that numerical models are constructed that represent the evolution of natural subduction, as reconstructed by tectonic and geological evidence. In this way further understanding of the rheology of the mantle and dynamics of subduction zones can be obtained and can substantiate or reject the styles of subduction and their dependencies as determined by Schellart (2008), Stegman et al. (2010) and Garel et al. (2014).

1.2 South Sandwich trench

One of the thoroughly investigated subduction systems is the South Sandwich (SoSa) trench, located at the eastern margin of the Scotia Sea, a tectonic complex area between the South American plate (SAM) and the Antarctic plate (ANT, fig 2). This area links the southernmost Andes to the Antarctic Peninsula (ANTP, Dalziel et al., 2013) and is an important area in terms of oceanography, tectonics and biogeography (Eagles et al., 2005).

Recently, Kosters et al. (2015) tectonically reconstructed the evolution of South Sandwich by combining a wide range of available geological and magnetic anomaly data in the open-source program GPLATES. This reconstruction is shown in Figure 3. In the following paragraphs I will briefly describe this reconstruction and put forward the complex dynamic controls which could be assessed using geodynamic modelling.

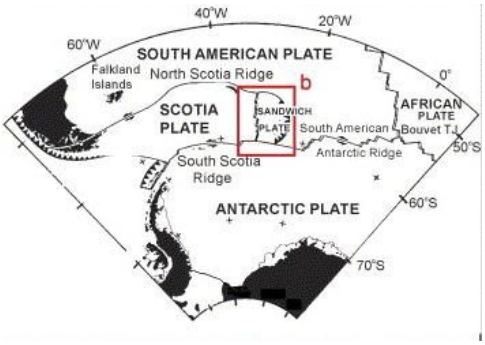

Figure 2: Tectonic setting of the Scotia Sea.

The initiation of the South Sandwich subduction system was reconstructed to be originated roughly 80-70 Myr ago at an E-W striking passive margin within the SAM connecting the continental Patagonia-Falkland Plateau in the north to the 80 Myr old Cretaceous oceanic lithosphere of the Weddell Sea in the south (Figure 3A). The passive margin was weakened by the spreading ridge separating the Aluk plate from the Farallon plate (Figure 3B) subducting eastward beneath the SAM plate. Subduction initiation was then triggered in this weakened zone by a short period of roughly N-S convergence between SAM and ANTP around 80-70 Ma, seemingly enough to trigger self-sustaining subduction. Over time this intra-plate immature subduction zone lengthened towards the NE and SW, consuming a total of 150 km of oceanic lithosphere over a time frame of roughly 80-50 Ma.

From 50 Ma onwards, the subducting oceanic lithosphere starts to sink more rapidly. As it sinks the trench remains stationary with respect to the mantle while the subducting and overriding plate both move with an absolute velocity of 2 cm/yr to the NW. As the absolute velocity is parallel to the direction of subduction, the amount of slab consumption along the mantle stationary trench is similar to the amount of pre-drift continental extension in the overriding plate. In a time frame of 50-25 Ma 300 km slab is consumed and thus a similar 300 km of pre-drift continental extension is created in the OP.

Around 27 Ma the continental extension evolves into the creation of a spreading ridge, the West Scotia Ridge, and the first oceanic lithosphere is created (Figure 3C). From 25 Ma the trench is no longer stationary and roll back starts towards the south. This causes the opening of the Scotia Sea and creates a new microplate: the Scotia Plate. Over time rollback gets redirected to the SE/E as the subduction zone interacts with the South Scotia Ridge, separating the SAM plate from the ANT plate in the south (Figure 2).

Roughly 16 Ma the spreading in the West Scotia Ridge slows down and a new spreading ridge is formed: the East Scotia Ridge. The creation of this ridge caused a second microplate to form East of the Scotia Plate: the Sandwich plate (Figure 2). Up until today this ridge remains active and SAM plate continues to subduct underneath this young plate towards the west with a velocity of 5 cm/yr (Figure 3D).

The reconstruction of Kosters et al. (2015) is conceptually and kinematically well understood, however the geodynamic controls on this complex interaction between the evolution of the slab, the motion of the lithospheric plates and the underlying mantle remain unknown. Especially the onset of subduction in an intra-plate setting with only little convergence is a big issue of debate, as well as the cessation and redirection of subduction on interaction with the South Scotia Ridge,

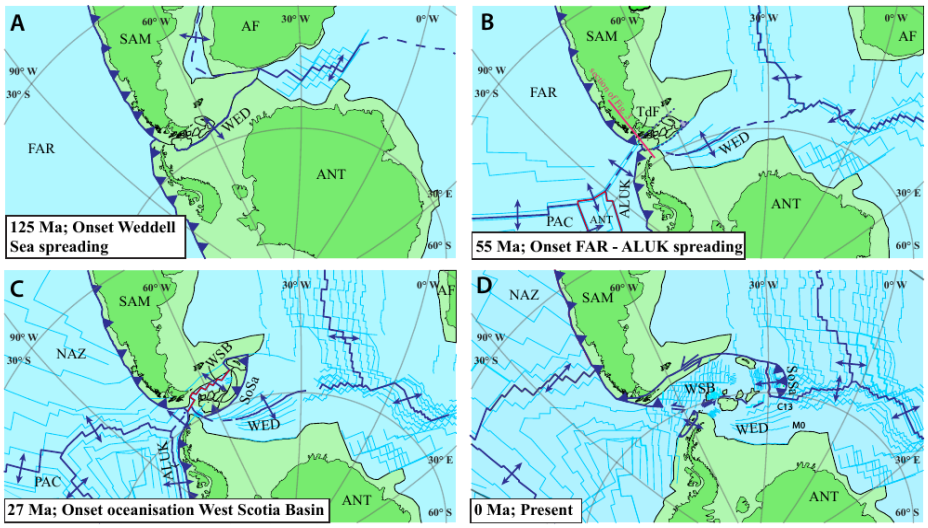

Figure 3: Tectonic reconstruction of the Scotia region by Kosters et al 2015 from 125 Ma to present. ANT=Antarctica plate, SAM= South America Plate, WED=Weddell Sea, TdF=Tierra del Fuego, SoSa=South Sandwich Trench, WSB= West Scotia Basin (Kosters et al., 2015).

which are both geodynamically challenging. To get a better understanding of the geodynamic controls, assessment of the geodynamic forcing controlling this evolution is required. Reconstructing evolution of the subduction system by Kosters et al. (2015) in a numerical model will help to obtain new knowledge of the forcing of this subduction system, and thus to subduction systems in general, and the interaction between plates, mantle and slab. The rheology of the mantle and lithosphere plays a key role in this interaction and I aim to put new constrains on the viscosity of the mantle, allowing for the tectonic evolution of the Scotia Sea as observed.

1.3 Research goal and setup

The initial goal of this research was to reconstruct the evolution of the Scotia Sea in a two-dimensional numerical dynamic visco-elastic subduction model as shown in Figure 8. As the direction of roll-back changes direction over time, a three-dimensional model would be preferred. This however outside the scope of this study. To construct the model the finite element code ELEFANT is used, created to solve large scale viscous problems. A viscosity field is implemented based on the experimental flow laws, allowing various deformation mechanisms to contribute to the composite viscosity. This research is divided into two sections. In the first section I aim to create an intra-oceanic subduction zone, similar to the setup used by Garel et al. (2014) to obtain the various slab evolutions in a intra-oceanic subduction system. To do so the flow laws are implemented and the parameters are tuned to obtain a plausible subduction evolution.

In the second section the setup is changed to one similar to the Scotia Sea region. This is done by replacing the oceanic overriding plate by a continental overriding plate and implementing a weak zone between the plates, allowing for extension in the OP. These adaptations, however, caused unexpected difficulties concerning the decoupling of the slab at the surface preventing any trench motion. Together with the problems concerning the behavior of the upper- lower mantle (ULM) boundary, this has prevented us from creating a fully functioning continent-ocean subduction system. The lack of a fully functioning reference model I was unable to further model the evolution of the Scotia Region and put constrains on the conditions necessary to make this evolution possible.

This thesis will thus focus on the production of a fully functioning two-dimensional numerical subduction system for both an intra-ocean and continent-ocean setting in the finite element code ELEFANT and the numerical difficulties I encountered. First our current knowledge and uncertainties of the rheology of the mantle will be set out, as a dominant factor determining the evolution of subduction. In the methods I will describe the two different setups, the governing equations used to create a mantle-representative model and the numerical implementation of these equations. The results will be divided into two separate sections. The first section will present the result of the runs concerning an intra-oceanic subduction system, the second section will present the runs concerning the Scotia Region setup. In both sections our process of creating a plausible subduction model will be set out, describing the various attempts and their flaws. In the discussion the models and their flaws will be compared to other studies and suggestions for further research will be put forward.

2 Rheology

2.1 Viscous deformation

The mineralogical composition of the mantle is given in Figure 4. The main minerals composing the upper mantle are olivine, orthopyroxene (opx), clinopyroxene (cpx) and garnet (grn), as given in Figure 4. From these the most abundant mineral is olivine. By laboratory studies and microstructural analysis it is shown that olivine is also probably the weakest mineral under a wide range of conditions (Karato and Wu, 1993). For this reason the rheology of the upper mantle is assumed to be dominated by olivine. Based on material studies on high-temperature creep deforming olivine under mantle conditions, the important mechanisms of deformation in the Earth are suggested to be (1) dislocation creep, (2) diffusion creep and (3) Peierls creep (e.g., Stocker and Ashby, 1973, Goetze and Evans, 1979, summarized in Karato, 2010).

(1) Dislocation climb creep, also known as power law creep, involves the movement of dislocations through the crystal lattice of the material causing deformation of the crystals and thus the material. Dislocation creep is highly sensitive to the stress on the material, resulting in a non-Newtonian viscosity (Ranalli, 2001). It is the dominant deformation mechanisms for high stresses and relatively high temperatures (Figure 5). Dislocation creep is insensitive to grain size.

(2) When deformation is caused by diffusion creep, crystalline solids deform by the diffusion of vacancies through their crystal lattice. Diffusion creep is sensitive to grain size and temperature and insensitive for stress. It dominates for low stresses and high temperatures (Figure 4) and results in Newtonian viscosity (Ranalli, 2001).

(3) Peierls creep is a low temperature dislocation glide deformation mechanism and depends on the stress needed to move a dislocation within a plane of atoms (Peierls stress). It is believed to be the stress limiter at low temperatures and has a strong exponential dependence on stress (Kameyama et al., 1999).

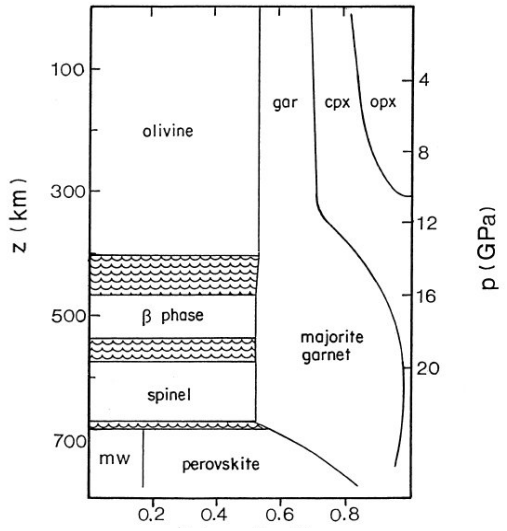

Figure 4: Mineralogical composition mantle of the mantle vs depth (z, km). gar=garnet, cpx=clinopyroxene and opx= orthophyroxene. From Putnis, 1992.

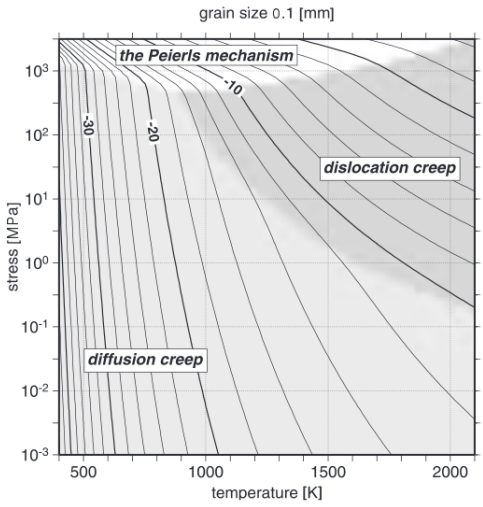

Figure 5: Deformation mechanism vs temperature (K), stress (MPa) and strain rate (s^{-1}, solid lines). Grain size is set constant at 0.1 mm. From Kameyama et al., 1999.

All three deformation mechanisms are active in deforming polycrystals and the macroscopic strain rate is thus a sum of the three mechanisms. The relative importance of the mechanism depends on the stress, strain rate, grain size, temperature, pressure, material parameters and chemical environment (Ranalli, 2001). Based on many laboratory data and theoretical microphysical models (see Karato, 2010) a generic form of flow laws have been constructed for these three deformation mechanisms relating strain rate to stress, material parameters, pressure and temperature:

$$\dot{\epsilon}_{II} = A\sigma^n d^{-m} \exp\left(\frac{Q+PV}{RT}\right) \tag{1}$$

Using the definition of viscosity, $\mu = \frac{\sigma}{2\dot{\epsilon}_{II}}$,the viscosity equation can be written as:

$$\mu_{disl/diff} = A^{-\frac{1}{n}} \dot{\epsilon}_{II}^{\frac{1-n}{n}} d^m \exp\left(\frac{Q+PV}{nRT}\right) \tag{2}$$

where $\dot{\epsilon}_{II}$ is the second invariant of the strain rate, σ the stress, d the grain size, T the temperature, P the pressure and R the gas constant (8.15, table 3). A, n, m, Q and V are the material parameters whose values remain poorly

constrained. A is the prefactor, n the sensitivity to stress σ, m the sensitivity to grain size d, Q the activation energy and V the activation volume.

As diffusion creep is not dependent on strain rate, $n = 1$ for diffusion creep. Dislocation creep is independent on grain size so $m = 0$.

The equations separately then become: dislocation creep:

$$\mu_{disl} = A^{-\frac{1}{n}} \dot{\epsilon}_{II}^{\frac{1-n}{n}} \exp\left(\frac{Q+PV}{nRT}\right) \tag{3}$$

diffusion creep:

$$\mu_{diff} = A d^m \exp\left(\frac{Q+PV}{RT}\right) \tag{4}$$

For Peierls creep the activation energy Q is actually not a constant but depends on stress (Karato, 2010), and the following flow law is more appropriate (Kameyama et al., 1999):

$$\mu_{disl}(\dot{\epsilon}_{II}) = A^{-\frac{1}{n}} \dot{\epsilon}_{II}^{\frac{1-n}{n}} \exp\left(-\frac{Q}{RT}(1-\frac{\sigma}{\sigma_p})^q\right) \tag{5}$$

where σ_p is Peierls stress and q an exponent.

2.2 Viscosity constraints

The values of the material parameters for the deformation mechanisms are obtained by either laboratory experiments or theoretical models and vary greatly between studies. Table 1 gives the values obtained for olivine, garnet and perovskite for diffusion creep and dislocation creep obtained by several authors. Values for Peierls creep remain highly uncertain as laboratory experiments are difficult (Karato, 2010).

The values presented in table 1 also only partly represent the composition of the mantle. As seen in Figure 4, the UM only partly consists of olivine (roughly 55%, Ranalli, 2001). The rest is a mixture of garnet (gar), clinopyroxene (cpx) and orthophyroxene (opx). Also, laboratory experiments can only be done in a limited temperature and pressure range, although improvements have been made throughout the years and pressures up to 17 GPa and temperatures up to 2200 K (1927 °C) have been reached recently(Karato, 2012). However the large difference in timescale remains a large issue. As seen in Figure 4, olivine transforms to spinel around 410 km. Little is known about the properties of spinel and commonly values of olivine are used until the transition to perovskite at 660 km.

Additionally the values are based on dry olivine. However when oceanic lithosphere subducts, this brings water into the mantle, hydrolizing the mantle material. When olivine is hydrated dislocation slide becomes easier resulting in strain weakening. This allows for a more vigorous mantle flow and promotes localization of strain (Quinquis and Buiter, 2014). Hydrated olivine is know as wet olivine and experimental studies have shown that wet olivine has lowered material parameters, especially activation energy (Karato and Jung, 2003), and it increases the water fugacity f_{OH}. Water fugacity in equation 28 taken as a constant in to prefactor A. f_{OH} can thus instead be taken out of the prefactor A and become a variable parameter (Hirth and Kohlstedt, 2003).

The parameters determining the viscosity in the lower mantle, composed of primarily perovskite (Figure 4), are even less constrained. Because the pressure and temperature is so high in the lower mantle, laboratory experiments are almost impossible and all data is based on geophysical constraints (Billen and Hirth, 2007).

These geophysical constrains have produced a variety of 1D viscosity-depth profiles over the mantle. Figure 6a gives the three-layer and five-layer viscosity profile obtained by Lambeck and Johnston (1998) by analysis of postglacial rebound data. Figure 6b gives viscosity profiles obtained by various authors based on joint inversion of the geoid (M&F=Mitrovica and Forte, 2004), mineral physics (S&C= Steinberger and Calderwood, 2006) and global sea level data related to postglacial rebound (P= Peltier, 1999, F&M= Forte and Mitrovica, 1996) up to 3000 km deep.

Although the viscosity profiles vary greatly, there are similarities that are widely agreed on. The viscosity of the upper mantle is roughly between $10^{20} Pa.s$ and $5 \cdot 10^{21} Pa.s$ and there is a jump in viscosity around 660 km depth. The viscosity of the lower mantle however ranges between $10^{21} Pa.s$ and almost $10^{24} Pa.s$ and the jump at the ULM varies from a factor 3 to 100. The majority of the models however agree on a viscosity jump around 10-30 (Ranalli, 2001).

These 1D viscosity profiles do not include the lateral variations in rheological properties as they assume radial symmetry (Karato, 2010). No difference is for example made between continental and oceanic upper mantle and local variations due to subducting slabs are not included.

Additionally, information is obtained by seismological studies. Shear wave splitting has shown that the lower mantle is highly isotropic while in the upper mantle anisotropy of ±10% has been observed (Meade et al., 1995). Both olivine (dominant mineral in the UM) and silicate perovskite (dominant mineral in the LM) are however elastically anisotropic

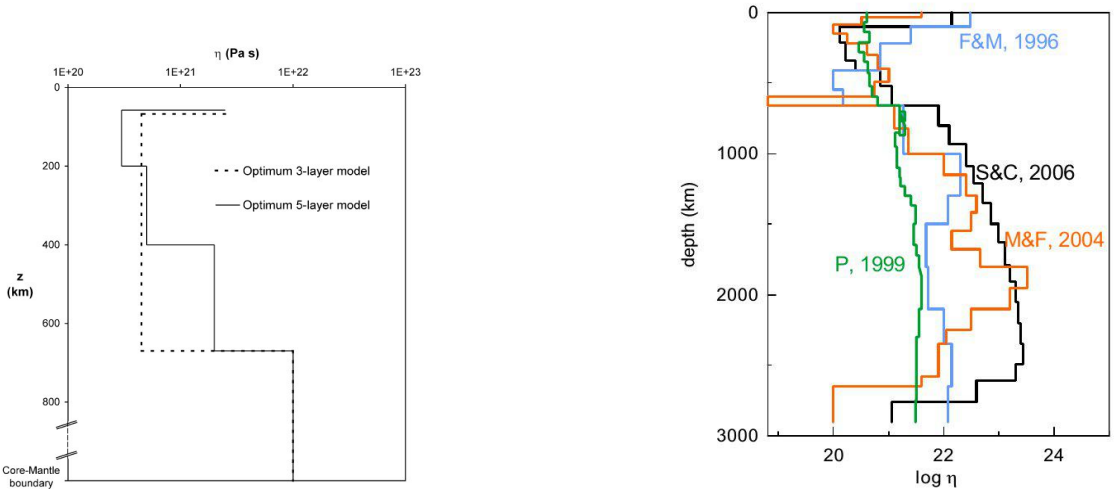

Figure 6: a) three-layer and five-layer viscosity profile obtained by Lambeck and Johnston (1998). b) Viscosity profiles obtained by joint inversion of the geoid (M&F=Mitrovica and Forte (2004)), mineral physics (S&C= Steinberger and Calderwood (2006)), global sea level data (P= Peltier (1999)) and post glacial rebound (F&M= Forte and Mitrovica, 1996) vs depth. From Čížková et al. (2012).

(Meade et al., 1995). Deformation by dislocation creep would thus result into an anisotropic structure. As diffusion creep results in an isotropic structure, it is suggested that deformation in the lower mantle is mainly by diffusion creep (Karato et al., 1995). Also the grain-size reduction at the ULM boundary favors for diffusion creep as diffusion creep is dependent on grain size (Ito and Sato, 1991).

Put together, although there has been a lot of laboratory and geophysical research about the rheology and deformation mechanisms in the earth's mantle, a lot of disagreement and uncertainty remains. Numerical model studies are thus important to tune and test the plausibility and put constrains on these obtained values.

2.3 Yielding

Besides viscous deformation, material can also deform when its yield strength (the strength at which the material will fail or undergo plastic yielding) is exceeded. The yield strength determines the maximum shear stress a material can hold before it will brittle or plastically deform (Billen and Hirth, 2007). At shallow depth the material will deform by brittle processes while with an increase of pressure and a relatively low temperature plastic yielding will take over brittle yielding. Yielding is particularly important at the trench and in the cold interior of the slab as it sinks, weakening the slab in areas of high curvature (Royden and Husson, 2006). The transition to viscous deformation generally occurs around temperatures of 700-850 °C (Billen and Hirth, 2007).

The yield strength is calculated using the Drucker-Prager yield criterion (Drucker and Prager, 1952):

$$\tau_y = Psin(\phi) + Ccos(\phi) \tag{6}$$

The Drucker-Prager yield criterion determines the yield strength of the material τ_y under a certain lithostatic pressure P. It depends on the the cohesion C (the yield strength at the surface), and the angle of friction ϕ. If the yield strength is exceeded, all deformation will be accommodated by brittle or plastic yielding (Billen and Hirth, 2007).

The upper bound of the yield strength is determined by a maximum yield strength $\tau_{y,max}$. 1000 MPa is used in most models as it is similar to the stress predicted for low-T plasticity at 600-700 °C (Billen and Hirth, 2007). However, 1 GPa has been used for models implementing Peierls creep as a dominant deformation mechanisms at low temperatures and high stresses (eg Garel et al., 2014).

Implementing the maximum yield strength $\tau_{y,max}$, the yielding viscosity is determined by the yield strength and the second invariant of the strain rate following the yield-stress law:

$$\mu_y = \frac{min(\tau_y, \tau_{y,max})}{2\dot{\epsilon}_{II}} \tag{7}$$

Increasing the strain rate will thus decrease the yielding viscosity, depending on the yield strength of the material and the maximum yield strength.

Table 1: Parameters dislocation creep and diffusion creep from experiments done on dry olivine.

	Prefactor A (Pa^{-n}/s)	Activation energy Q (kJ/mol)	Activation volume V (cm^3/mol)	Exponent n
Dislocation creep				
Dry olivine				
Kawazoe et al., 2009		530	15-20	3.5
Li et al., 2006		470	0 ± 5	3.0
Karato and Rubie, 1997		540	14 ± 1	3
Hirth and Kohlstedt, 2003		530 ± 4	20.5 (14-27)	3.5 ± 0.3
Karato and Wu, 1993	$2.4 \cdot 10^{-16}$	540	15-25	3.5
Ranalli, 1991	$3.2 \cdot 10^{-17}$	520	15	3.5
Hirth and Kohlstedt, 2003	$3.1 \cdot 10^{-17}$	480	11	3.5
Korenaga and Karato, 2008		610 ± 30	13 ± 8	4.94 ± 0.05
Garnet				
Karato et al., 1995	$2.5 \cdot 10^{-10}$	645	2.7	
Perovskite				
Beauchesne and Poirier, 1990	$7.4 \cdot 10^{-17}$	500	-	3.5
Diffusion creep				
Dry olivine				
Hirth and Kohlstedt, 2003	$1 \cdot 10^{-9}$	375 ± 50	6 (2-10)	1
Karato and Wu, 1993	$6.1 \cdot 10^{-19}$	300	6	1 (m=2.5)
Korenaga and Karato, 2008	$10^{5.25 \pm 0.0}$	261 ± 28	6 ± 5	1
Garnet				
Wang and Ji, 2000	$3.5 \cdot 10^{-15}$	347	-	1 (m=2.5)
Perovskite				
Li et al., 1996		750	-	1 (m=2)

Table 2: Parameters dislocation creep and diffusion creep used in numerical subduction models.

	Prefactor A (Pa^{-n}/s)	Activation energy Q (kJ/mol)	Activation volume V (cm^3/mol)	Exponent n
Dislocation creep				
Čızková et al., 2002	$2.42 \cdot 10^{-15}$	540	14	3.5
Billen and Hirth, 2007		480	11	3.5
Čížková et al., 2012	$3.1 \cdot 10^{-17}$	480	11	3.5
Garel et al., 2014	$5.0 \cdot 10^{-16}$	540	12	3.5
Maffione et al., 2015	$2.4 \cdot 10^{-16}$	540	0-20	3-4.7
Chertova et al., 2017	$2 \cdot 10^{-18}$	423-433	8-9	3
Diffusion creep				
Čızková et al., 2002	$6.07 \cdot 10^{-18}$	300	4.5	1
Čížková et al., 2012	10^{-9}	335	4.8	1
Garel et al., 2014	$3.0 \cdot 10^{-11}$	300	4	1
Chertova et al., 2017	$5.3 \cdot 10^{-15}$	240	3-4	1
Lower mantle				
Čížková et al., 2012b	$5 \cdot 10^{-17} - 10^{-15}$	200	1.1	1
Čížková et al., 2012a	$1.8 \cdot 10^{-15} - 2.3 \cdot 10^{-14}$	200	2.2	1
Garel et al., 2014	$2 \cdot 10^{-16} - 2 \cdot 10^{-17}$	200	1.5	1
Peierls creep				
Garel et al., 2014	10^{-150}	540	10	20

3 Methods

3.1 Model setup section 1

The first model is based on the setup of Garel et al. (2014). It is an intraoceanic subduction system as shown in Figure 7. The domain is 9000 km wide and 1400 km deep over a square grid of 800x125 elements. This results in a resolution of 11.25×11.25 km per element (table 3).

The domain consists of 5 different materials: the subducting oceanic lithospheric plate (SP), the overriding oceanic lithospheric plate (OP), the oceanic crust (OC), the upper mantle (UM) and the lower mantle (LM). For each material the properties can be tuned separately.

As initial set up the subducting plate is subducted underneath the overriding plate at *x_trench* curving downwards until an angle of $\beta = 77°$, relative to the vertical (Figure 7). The bending radius of the slab is 250 km. This angle is chosen as, in Garel et al. (2014), it ensures the slab to sink without the requirements of external forces (self-sustaining subduction).

The transition between the lithospheric plates and the UM is defined by the 1473 K (1200°C) isotherm. The transition between the UM and the LM is defined at 660 km depth.

The OC is set at the top 25 km of the subducting plate and represents the weak oceanic crust of the subducting plate. Although an oceanic crust of 6 km would be more realistic, this is thinner than a single element in our domain (11.25 km) so will not be visible. To enable the oceanic crust to function as a weak zone between the OP and SP, a width of 25 km is chosen. In this way the OC covers over two elements.

The initial age of the lithospheric plates can be tuned both at the side boundaries of the domain (*Age SP left* and *Age OP right*) and at the trench (*Age SP trench* and *Age OP trench*) and increases linearly with age towards the trench.

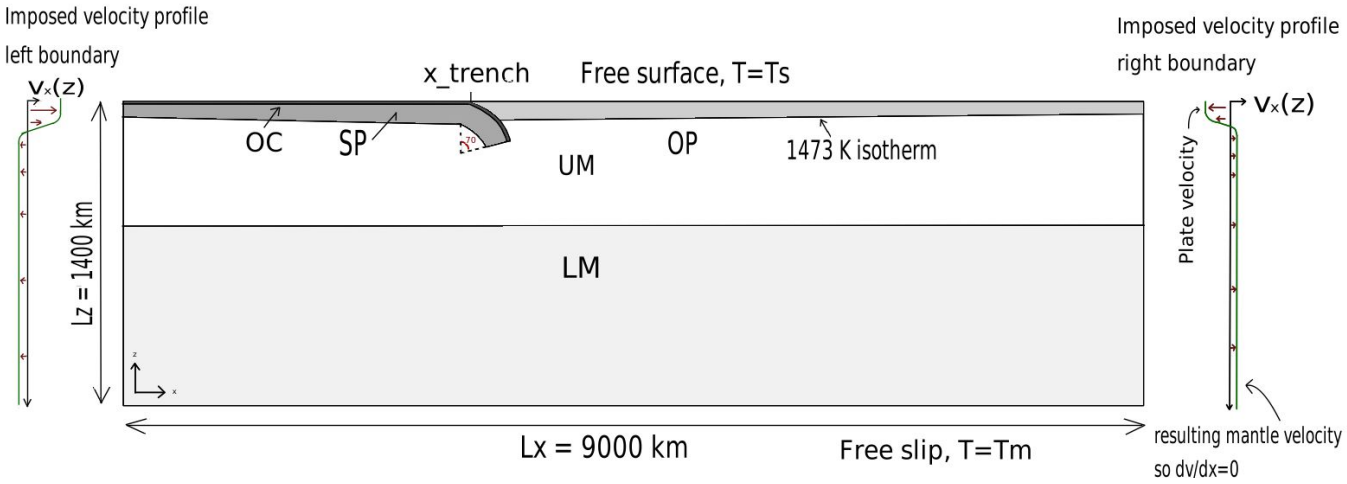

Figure 7: Set up of the model of section 1 with imposed velocity on left and right boundary. WZ= oceanic crust (weak zone), SP=subducting plate (oceanic lithospheric mantle), OP=overriding plate (oceanic lithospheric mantle), UM=upper mantle, LM= lower mantle, Lz= total depth, Lx= total width.

3.2 Model setup section 2

To model a system similar to the Scotia region as discussed in section 1.2, an ocean-continent subduction system is created. The domain is reduced to Lx=3000 km and Lz=900 km. With a squared grid of 450x135 elements of 6.7x6.7km are created.

Creating a N-S profile from left to right, the continental OP is set on the left side of the domain. The set up is shown in Figure 8. Here the oceanic lithospheric plate (subducting plate, SP) subducts underneath the continental lithospheric plate (overriding plate, OP). As the South Sandwich trench retreats roughly in a SE-E direction, the continental OP is set on the left side (NW-W) of the domain and the oceanic subducting plate on the right side (SE-E).

Similar to section 1, the SP is initially curved downwards at a trench until an angle β, which is now set at 90°. An angle of 90°creates an initial subducted slab of 150 km underneath the lithosphere, which is reconstructed condition at 50 Ma for the South Sandwich trench. The oceanic lithosphere has an oceanic crust (OC) of 20 km deep (over 3 elements) upon the lithospheric mantle. The age of the oceanic lithosphere at the trench is set at 80 Myr (as reconstructed) and the age of the oceanic plate at the right boundary is varied from 20-80 Myr. The overriding plate is continental and has

Table 3: Dynamic model parameters

Quantity	Symbol	Unit	Value
Thermal diffusivity	κ	m^2/s	10^{-6}
Thermal expansivity coefficient	α	K^{-1}	3.10^{-5}
Gas constant	R	$J/mol/K$	8.314
Gravity acceleration	g	m/s^2	9.8
Surface density	ρ_s	kg/m^3	3300
Surface temperature	T_s	K	273
Lithospheric temperature	T_l	K	1473
Mantle temperature	T_m	K	1573
Reference density	ρ_{ref}	kg/m^3	3300
Reference density CC	ρ_{refCC}	kg/m^3	2800
Reference viscosity	μ_{ref}	$Pa.s$	10^{21}
Minimum viscosity	μ_{min}	$Pa.s$	10^{19}
Maximum viscosity	μ_{max}	$Pa.s$	10^{25}

a constant age and thus a constant thickness, temperature field and density field. The OP is 100 km thick and consists of a continental crust (CC) of 35 km thick above a lithospheric mantle of 65 km thick. As little is known about the exact thickness of the Patagonia-Falkland Plateau 50 Ma, the thickness is chosen based on average phanerozoic continental crustal and lithospheric thicknesses (Djomani et al., 2001) and which is used in other numerical subduction models (Baes et al., 2011, Nikolaeva et al., 2010, Holt et al., 2015, Nakakuki and Mura, 2013).

In later runs a weak zone (WZ) is implemented at the contact zone between the overriding and subducting plate, promoting decoupling between the plates creating a back-arc basin as the trench is able to rollback. The weak zone is either 20 or 40 km wide. The rheological parameters of the weak zone are set equal to the continental crust or given a constant low viscosity of $10^{19} Pa.s$.

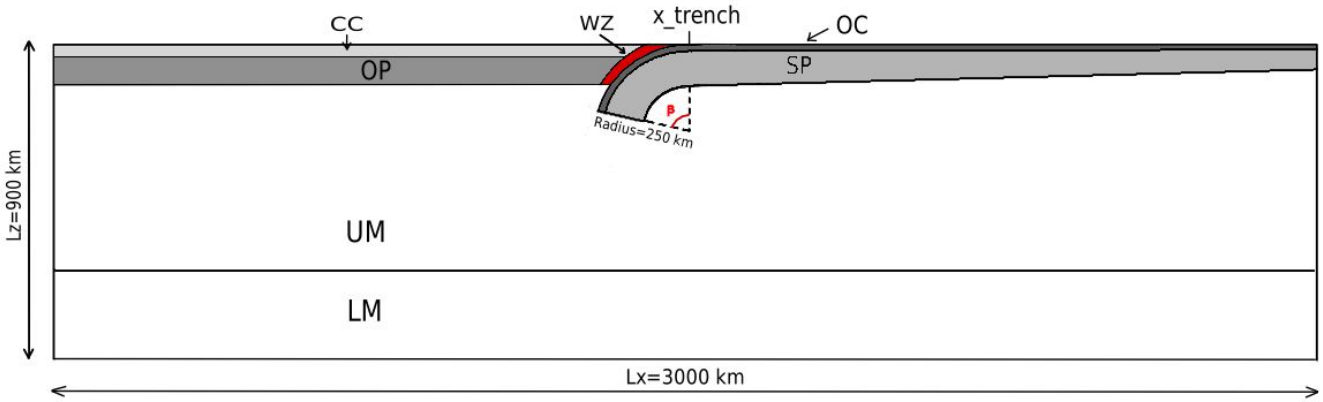

Figure 8: Set up of the model of section 2. OC= oceanic crust, CC= continental crust, WZ= weak zone, SP=subducting plate (oceanic lithospheric mantle), OP=overriding plate (continental lithospheic mantle), UM= upper mantle, LM= lower mantle, Lz= total depth, Lx= total width.

3.3 Governing equations

To produce a numerical model of subduction evolution the mechanical behaviour of the crustal and mantle materials has to be obtained by solving governing equations. As the elastic response of the lithosphere can be ignored over timescales over 1 Myr, the lithosphere can be approximated to behave visco-plastically (Billen, 2008). With this assumption, inertia forces can be neglected and elasticity is not taken into account. This leads to the following form of the stokes equation (Kim and Karrila, 2013):

$$\boldsymbol{\nabla} \cdot \boldsymbol{\sigma} + \rho \boldsymbol{g} = 0 \tag{8}$$

where $\boldsymbol{\sigma}$ is the stress tensor, ρ the mass density and $\boldsymbol{g}$ the gravity acceleration.

To compute the temperature field within a deforming system, heat transport equation is solved (Dai and Nassar, 1999):

$$\rho c_p \left(\frac{\partial T}{\partial t} + \boldsymbol{v} \cdot \boldsymbol{\nabla} T \right) = \boldsymbol{\nabla} \cdot (k \boldsymbol{\nabla} \boldsymbol{T}) + H \tag{9}$$

where c_p is the heat capacity (table 3), T the temperature, t the time, $\boldsymbol{v}$ the velocity, k the thermal conductivity, H the radiogenic heat production and $\boldsymbol{v}$ the velocity.

Additionally, the law for mass conservation has to be met (equation 10, Schubert, 2015).

$$\frac{\partial \rho}{\partial t} + \rho \boldsymbol{\nabla} \cdot \boldsymbol{v} = 0 \tag{10}$$

Here $\frac{\partial \rho}{\partial t}$ is the change in density through time. In our model we assume the material to be incompressible, so $\frac{\partial \rho}{\partial t} = 0$. This results in equation 11. To satisfy this equation the total amount of material in the domain should thus remain equal, also when material is flowing in an out of the domain.

$$\boldsymbol{\nabla} \cdot \boldsymbol{v} = 0 \tag{11}$$

To solve these equations, the stress tensor needs to be related to velocity and pressure. These relations are given by the following equations:

$$\boldsymbol{\sigma} = -p\mathbf{1} + \boldsymbol{s} \tag{12}$$

$$\boldsymbol{s} = 2\mu \dot{\boldsymbol{\epsilon}} \tag{13}$$

$$\dot{\boldsymbol{\epsilon}} = {}^1\!/_2 (\nabla \boldsymbol{v} + (\nabla \boldsymbol{v})^T) \tag{14}$$

where p the pressure, 1 is the unit tensor, $\boldsymbol{s}$ the deviatoric stress, μ the dynamic viscosity, $\dot{\epsilon}$ the strain rate tensor and $\boldsymbol{v}$ the velocity field.

Implementing equations 12, 13 and 14 into equation 8 leads to the following equation:

$$\boldsymbol{\nabla} \cdot (\mu(\boldsymbol{\nabla} \boldsymbol{v} + (\boldsymbol{\nabla} \boldsymbol{v})^T) - \boldsymbol{\nabla} \boldsymbol{p} + \rho \boldsymbol{g} = \mathbf{0} \tag{15}$$

which is known as the strong form of the Stokes equation.

3.4 Initial conditions

3.4.1 Temperature field

The initial temperature field in the lithospheric oceanic plates is defined by a half-space cooling model (equation 16, Turcotte and Schubert, 2002):

$$T(x, y, t = 0) = T_s + (T_m - T_s) erf \left(\frac{Lz - z}{2\sqrt{\kappa Age^0(x)}} \right) \tag{16}$$

Here T_s is the temperature at the surface, T_m is the mantle temperature, $Lz - z$ the depth ($z = 0$ is at the bottom of the domain), κ the thermal diffusivity ($10^{-6} m^2/s$, table 3) and $Age^0(x)$ the initial age of the lithospheric plate at location x. The age of the lithospheric plates increases linearly from the side of the domain until x_{trench}, which is the location of the trench at the surface.

Assuming the temperature field in the lithospheric slab is equal to that of the subducting plate, equation 16 can also be used for the initial slab. However instead of cooling towards the bottom the temperature cools towards the midpoint of the circle around which the slab bends. Equation 16 can then be rewritten to:

$$T(x, y, t = 0) = T_s + (T_m - T_s)erf\left(\frac{radius - C_M}{2\sqrt{\kappa Age^0(x)}}\right) \tag{17}$$

Where *radius* is the bending radius, C_M is the distance between location (x, y) and the midpoint (x_c, y_c). As this formula only concerns the slab it is only valid for $x > x_c$, $y > y_c$ and $\beta_M < \beta$. Where β_M is the angle between the location (x, y) and the vertical at (x_c, y_c).

For continental lithosphere a steady state geotherm is created from 0 to 1300 °C over the thickness of the lithosphere (Baes et al., 2011). No difference is made between the temperature gradient in the crust and in the lithosphere. Radiogenic heat production in the continental crust is neglected as it is outside the span of this study. The weak zone follows the same geothermal gradient as the continental lithosphere.

The upper and lower mantle are set to a constant temperature of 1300 °C. No temperature gradient is present in the mantle for simplification.

3.4.2 Density field

The initial density field of the domain is dependent on the temperature and defined by equation 18.

$$\rho(T) = \rho_0(1 - \alpha(T - T_s)) \tag{18}$$

Here ρ_0 is the reference density and α the thermal expansivity coefficient α ($3.10^{-5}K^{-1}$, table 3).

ρ_0 is defined as 3300 kg/m^3 for the oceanic lithosphere, continental lithospheric mantle, the upper and lower mantle. With a inverse dependence on temperature, the density decreases with depth in the oceanic lithosphere, following the half-space cooling model. In the slab the curved temperature profile is followed. In this way the negative buoyancy of the slab and the plate causes it to sink.

In the continental lithosphere, only the lithospheric mantle is negatively buoyant with ρ_0 set at 3300 kg/m^3. As the continental crust is positively buoyant, ρ_0 is set at 2800 kg/m^3 for the continental crust (Faccenda et al., 2008, Babeyko and Sobolev, 2008, table 3). For the weak zone ρ_0 is also set at 3300 kg/m^3.

No phase changes are added at 410 and 660 km depth for simplification and so no density differences are present with depth in the mantle. Due to the constant temperature of the mantle the density of the mantle is also constant. With $T_m = 1300$°C and $T_s = 0$°C and following equation 16, we obtain a constant density for the mantle of $3171kg/m^3$ (see Figure 10).

3.5 Boundary conditions

The top boundary is set as a free surface with an isothermal temperature of $T_s = 0$°C and the bottom boundary as free slip with an isothermal temperature of $T_m = 1300$°C. The left and right boundaries can be either set at free slip or a plate velocity can be imposed. To satisfy the conservation of mass, the imposed plate velocities are compensated by a mantle outflow such that the total flux at the boundary is zero. To prevent large friction between the inflow and outflow at the boundary a sinusoidal function is implemented in a transition zone between the two to ensure a smooth transition (Figure 7).

To insure zero flux, the following equation has to be satisfied.

$$\Phi = \int_0^{L_y} u dy = 0 \tag{19}$$

with u the horizontal velocity.

With the sinusoidal function implemented from depth z_{l1} to z_{l2} on the left and from depth z_{r1} to z_{r2} on the right boundary, the mass conservation equation becomes:

$$\Phi = \int_0^{y_{l2}} u_{mantle_l} dy + \int_{y_{l2}}^{y_{l1}} (Asin(B(y - C)) + D)dy + \int_{y_{l1}}^{L_y} u_{plate_l} dy = 0 \tag{20}$$

For the left boundary and

$$\Phi = \int_0^{y_{r2}} u_{mantle_r} dy + \int_{y_{r2}}^{y_{r1}} (-Asin(B(y - C)) - D)dy + \int_{y_{r1}}^{L_y} u_{plate_r} dy = 0 \tag{21}$$

For the right boundary.

A, B, C and D are defined as:

$$\begin{aligned} A &= \frac{|u_{plate}| + |u_{mantle}|}{2}, \\ B &= \frac{\pi}{z_1 - z_2}, \\ C &= z_2 + 0.5(z_1 - z_2), \\ D &= |u_{plate}| - A. \end{aligned} \tag{22}$$

rewriting these equations gives the value for mantle inflow to obtain zero flux, $u_{mantle_{l/r}}$:

$$u_{mantle} = -2|u_{plate}| \frac{Lz}{\frac{1}{B}\left[-cos\left(B(-1/2(z_1 - z_2))\right) + cos\left(1/2B(z_1 - z_2)\right)\right] + z_1 + z_2} + |u_{plate}| \tag{23}$$

The velocity profiles can now be implemented on the left (l) and right (r) boundaries as follows.
if $z \geq z_1$ then:

$$\begin{aligned} u_l &= u_{plate_l} \\ u_r &= u_{plate_r} \end{aligned} \tag{24}$$

if $z_2 < z < z_1$ then:

$$\begin{aligned} u_l &= Asin\left(B(y - C)\right) + D \\ u_r &= -Asin\left(B(y - C)\right) - D \end{aligned} \tag{25}$$

if $z \leq z_2$ then:

$$\begin{aligned} u_l &= u_{mantle_l} \\ u_r &= u_{mantle_r} \end{aligned} \tag{26}$$

To check if mass conservation is satisfied, the value of the flux is calculated by equation 20 and 21 using the value for the mantle velocity obtained. If the equations are correct, the flux will be zero.

When absolute plate motion is applied, zero mantle flow is preferred and u_{mantle_l} and u_{mantle_r} are thus set to zero. The total amount of inflow on the one boundary has to be equal to the total amount of outflow on the other boundary to satisfy zero flux. To do so z_{l1} and z_{l2} are set equal to z_{r1} and z_{r2} and u_{plate_l} is set equal to u_{plate_r}. The sinus function for $z_2 < z < z_1$ becomes:

$$u_{l/r} = 0.5u_{plate} sin(\frac{\pi}{z_1 - z_2}(z - z_2 - 0.5(z_1 - z_2)) + 0.5u_{plate} \tag{27}$$

To be able to impose a velocity the initial age of the lithospheric plates at the boundaries should be at least 10 Myr old. If the plate is younger than this the plate is too thin for imposed the velocity on the boundaries to be transferred to the highly viscous plate. Instead this would result in a movement of the lower viscous mantle material below (De Laat, 2016).

3.6 Rheology

With the four deformation mechanisms mentioned in section 2 (diffusion creep, dislocation creep, Peierls creep and yielding), the viscosity field is calculated for our model. First the viscosity obtained by the separate deformation mechanisms is obtained. For simplification we took the grain size to be constant, and the values for d and m are added to the prefactor A. Also, instead of using a separate equation for Peierls creep (equation 5), the activation energy is taken constant so the same equation can be used for all three dislocation mechanisms. The high stress dependence is included for Peierls creep by setting the exponent n to a high value. Overall equation 2 is here modified to:

$$\mu_{disl/diff/prl}(\dot{\epsilon}_{II}, P, T) = A^{-\frac{1}{n}} \dot{\epsilon}_{II}^{\frac{1-n}{n}} \exp(\frac{Q + PV}{nRT}) \tag{28}$$

The initial values of the material parameters are given in Table 4 (section 4.1), labeled as *E_garel*. The values are similar to those used by Garel et al., 2014 and consistent with the experimental data as shown in table 1. As the values for

the material parameters are poorly constrained, we are allowed to tune these values to obtain an appropriate subduction system, within the limits of the obtained values of table 1.

To calculate the viscosity obtained by the yield strength of the material, equations 6 and 7 are used. $\tau_{y,max}$ is set at 1 GPa as Peierls creep is implemented to accommodate the strain under high pressure and low temperature. The initial values for the angle of friction ϕ and cohesion C are also given in table 4 and will be tuned.

The dominant deformation mechanism under a given condition is the mechanism that results in the lowest viscosity (Ranalli and Fischer (1984)). The composite viscosity is calculated by combining the viscosity obtained by the four deformation mechanisms by harmonic averaging:

$$\mu_{comp} = \left(\frac{1}{\mu_{disl}} + \frac{1}{\mu_{diff}} + \frac{1}{\mu_{prl}} + \frac{1}{\mu_y} \right)^{-1} \tag{29}$$

In this way the mechanism with the lowest viscosity will determine the viscosity, while the mechanism with the highest viscosity will only have a minimal contribution. When two mechanisms create a roughly similar viscosity they will both have a similar contribution to the composite viscosity. Harmonic averaging is preferred over arithmetic ($\mu_{comp} = \mu_{disl} + \mu_{diff} + ...$) or geometric averaging ($\mu_{comp} = \mu_{disl} \cdot \mu_{diff} \cdot ...$) as it yields the lowest effective viscosity and promotes subduction (Schmeling et al., 2008).

To prevent the viscosity to reach unrealistic low or high values (eg in the cold interior of the slab), the viscosity is limited to a a minimum viscosity of 10^{19} Pa.s (μ_{min}) and maximum viscosity of 10^{25} Pa.s (μ_{max}, table 3). This cut-off is implemented after the calculation of the composite viscosity. In this way the mechanisms creating extremely high viscosities are negligibly small in the harmonic averaging.

The various materials as described in the model setup (section 3.1) all have different properties so the values of the material properties are varied between the materials.

The lower mantle is believed to deform primarily due to diffusion creep (section 2), so the composite is only determined by diffusion creep. Also, as the viscosity has a more shallow gradient in the lower mantle (Figure 6), the activation volume and activation energy are both decreased. In table 4 the values for the lower mantle are marked with (LM).

The contact between the SP and OP should be weak, so friction at the contact zone is decreased and the SP can move along the OP. To decrease the viscosity the angle of friction and the cohesion are decreased for the oceanic crust (section 1). For the continental crust, the dislocation creep mechanism is weakened to comparable values used by Thieulot (2011) (see table 5, section 4.2).

3.7 Numerical implementation

The model is constructed with the two-dimensional version of the finite element code ELEFANT (Thieulot, 2014). ELEFANT solves the Stokes equation and the heat transport equation (equation 8 and 9) and is designed to address geological flow problems at crustal and lithospheric scales. It is based on bilinear velocity-constant pressure (Q1-P0) elements. This means that velocity is computed at the nodal points and pressure at the element center. The velocity is thus continuous over the elements as nodes belong to multiple elements (Q1) and the pressure is discontinuous as it is constant over every element and thus discontinuous over the boundary between them (P0, Tosi et al., 2015).

ELEFANT uses a penalty formulation to reduce the size of the matrix by imposing a relaxation on the incompressibility constraint (Thieulot, 2016). The equations are solved using the direct solver MUMPS, which is a parallel sparse direct solver made to solve large linear systems (Amestoy et al., 2000). This makes ELEFANT suitable to solve large and complex equations requiring many iterations over many time steps, as is needed to create a numerical subduction model.

The Arbitrary Lagrangian Eularian (ALE) algorithm is used to account for the free surface at the top boundary. This is done by allowing the grid to deform vertically while a constant width is maintained in horizontal direction (Thieulot, 2014), creating surface topography.

Furthermore a so called 'marker-in-cell' technique is implemented to track the material as it moves through the domain. A certain amount of markers is implemented in each cell, storing the rheological and thermal properties on that location at each time step. The markers are advected using the fourth-order Runge-Kutta technique. This advection scheme is very accurate in space (fourth-order accuracy) but less accurate in time (first-order accuracy) (Gerya, 2009). When markers exit the domain, it is flagged as inactive. To make sure that each element contains at least a minimal amount of markers, population control is applied. When an element contains a too low amount of markers, abnormal viscosity and density values can be obtained (Thieulot, 2016). Population control checks the number of markers per cell and will add a markers to the cell till its initial number of markers is restored (Thieulot, 2016).

To obtain the viscosity field using equation 28, non-linear iterations are needed. Since the viscosity is dependent on the strain rate, which is dependent on the velocity. Using non-linear iterations a starting viscosity μ_0 is chosen (eg $10^{21} Pa.s$ for the upper mantle) and a first guess of the velocity is obtained. With this outcome a new, more accurate viscosity field

is obtained for which the velocity field can be calculated again. The iterations continue until the velocity and viscosity field have converged and the difference between one iteration to the next is negligible. A correct velocity and viscosity is now obtained.

After the non-linear iterations have converged, the calculations start again for the next time step. The size of the time step is however not constant but is determined by Courant-Friedrichs-Lewy condition (Thieulot, 2011, equation 30). Here the size of the time step is dependent on the maximal velocity (v_{max}), the size of the smallest element in the domain (h_{min}) and the Courant number (C). The Courant number can be chosen between [0,1] and is set here at 0.05. To prevent the code from running too long, for example when the velocities exceed realistic values, a minimal time step of $dt_{min} = 100$ years is implemented.

$$dt = C\frac{h_{min}}{v_{max}} \tag{30}$$

The free surface simulation used, however, is sensitive to the size of the time step. If a too large time step is taken, numerical instabilities will develop as the velocity field at the surface will flip direction with every time step (Kaus et al., 2010). This instability is known as the "drunken sailor effect". This effect is caused by the fact that the topography is brought out of isostatic equilibrium with the rest of the model when the time step used is too big (Kaus et al., 2010).

To prevent the "drunken sailor effect" in ELEFANT, an approach known as the Free Surface Stabilization Approach (FSSA) is implemented in the code. The FSSA extends the existing force balance equations taking into account the effect caused by the deforming numerical grid by the free surface from one time step to the next (Kaus et al., 2010).

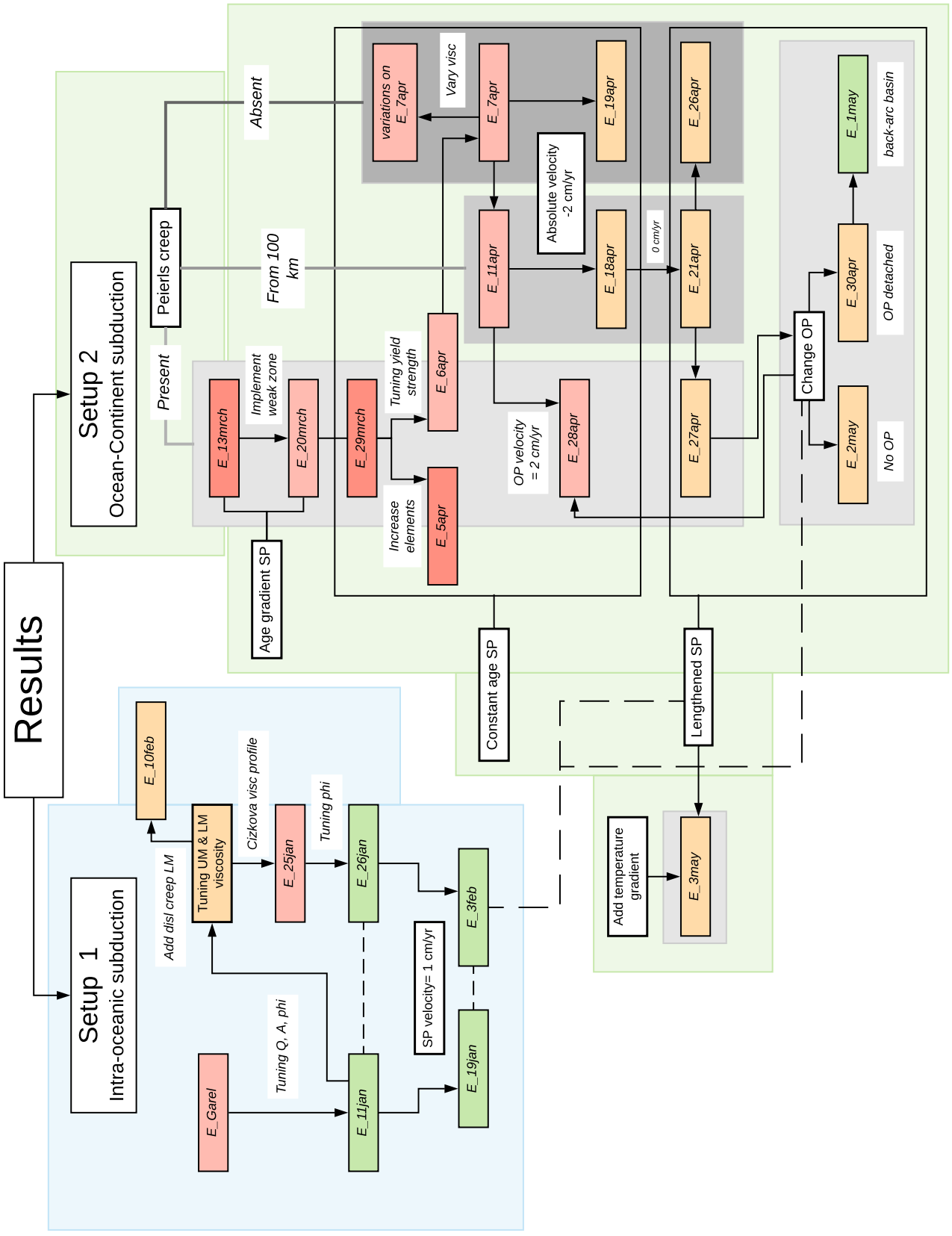

Figure 9: Schematic representation of the various runs. Blue: section 1, green: section 2. Colored boxes give the various boxes. Red - green indicate unsuccessful to successful runs, respectively. Grey boxes indicate the difference in Peierls creep.

4 Results

The results will be described following the two different setups as described in section 3. Searching for a fully functioning subduction model in both setups, I have experimented with various beginning and boundary conditions. I altered the rheological parameters within the range of plausible values obtained by various experiments and used by comparable numerical subduction models (see table 1 and 2). Additionally I experimented with the effect of Peierls creep and with adding (absolute) plate velocities in various settings.

To get an overview of our journey through the various experiments, Figure 9 gives an overview of the various experiments. The results of section 1 (intra-oceanic subduction) are given in blue, the results of section 2 (ocean-continent subduction) are given in green. Every colored box gives one experiment (named e.g., $E_1 1 jan$) and the colors of the box give an indication of the success of the run. Red is an unsuccessful run, orange indicates that subduction is created but there are still some imperfections and green indicates that the run is (relatively) successful. The other boxes give an indication of the variation of these experiments compared to the other experiments. The grey boxes indicate the presence of Peierls creep (dark grey: present, light grey: absent, grey: only present from 100 km dept).

4.1 Section 1: Intra-oceanic subduction

The following section describes the results of the various runs of section 1, as shown in blue in Figure 9. The runs represent an intra-oceanic subduction zone as described in section 3.1 for the setup shown in figure 7. I will describe and discuss every run separately and put forward the problems faced.

Figure 10 gives the initial conditions of the domain based on the equations given in section 3.1. The SP is initially 10-80 Myrs old and the OP 10-40 Myrs old, as is comparable to Garel et al., 2014. The top figure shows the 5 materials which are present in the domain (labeled as material 1-5). The middle figure shows the temperature division ranging from 0°C at the surface to 1300°C in the mantle following equation 16. The bottom figure shows the density profile ranging from $3300 kg/m^3$ at the surface to 3160 kg/m^3 in the mantle following equation 18.

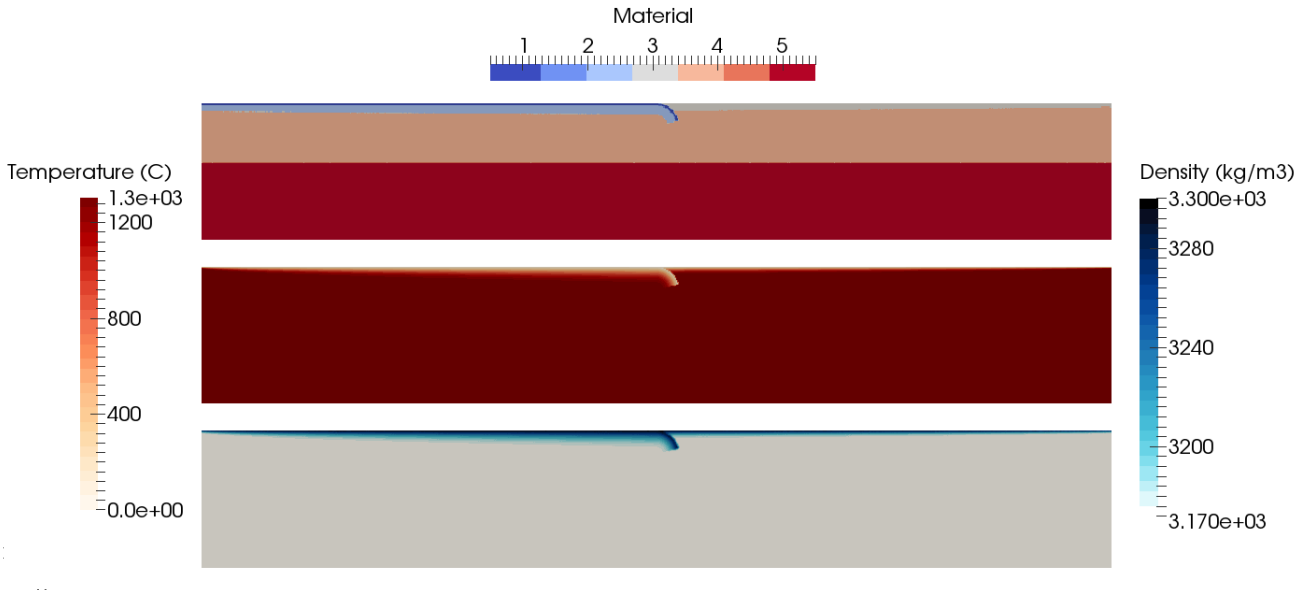

Figure 10: Begin conditions. Top: materials. 1= OC, 2= SP (10-80 Myr), 3= OP (10-40 Myr), 4= UM, 5= LM. Middle: temperature field. Bottom: density field. Legends will be similar for the following figures.

4.1.1 Run *E_Garel*

As a starting point the model is ran with the rheological parameters used by Garel et al., 2014 (table 4, labeled as *E_Garel*).

Figure 11 shows the result of the run after 9 Myrs. The slabs does not sink and instead the upper mantle material creeps to the surface through the overriding plate close to the slab (top figure of figure 11). The oceanic crust is not weak enough to decouple the overriding and subducting plate but instead mantle material penetrates through the overriding

Parameter	Run				
	E_Garel	E_11jan	E_16jan	E_25jan	E_26jan
dislocation creep					
A (Pa^{-n}/s)	$5 \cdot 10^{-16}$	$5 \cdot 10^{-16}$	$5 \cdot 10^{-16}$	$5 \cdot 10^{-16}$	$5 \cdot 10^{-16}$
Q (kJ/mol)	540	**560**	560	560	560
V (cm/mol)	12	**10**	10	10	10
n	3.5	3.5	3.5	3.5	3.5
diffusion creep					
A (Pa^{-n}/s)	$2 \cdot 10^{-11}$(UM)	$2 \cdot 10^{-11}$	$2 \cdot 10^{-11}$	$2 \cdot 10^{-11}$	$2 \cdot 10^{-11}$
	$5 \cdot 10^{-16}$(LM)	$5 \cdot 10^{-16}$	$5 \cdot 10^{-16}$	$5 \cdot 10^{-16}$	$5 \cdot 10^{-16}$
Q (kJ/mol)	300(UM)	300	300	300	300
	200(LM)	200	200	**210**	210
V (cm/mol)	4 (UM)	**3**	3	**2** (UM), **5** (SP,OP)	2 (UM), 5 (SP,OP)
	1.5 (LM)	1.5	1.5	**0.2**	0.2
Yield strength					
ϕ (°C)	11.31	11.31	11.31	11.31	11.31
	1.15 (WZ)	**0.5**	**0.7**	0.7	0.7
C (MPa)	10	10	10	10	10 (UM), **15** (SP,OP)
	2 (WZ)	2	2	2	2

Table 4: Values viscosity parameters in equation 28 for various runs.

plate close to the trench. Where the mantle material penetrates to the surface the viscosity reaches the minimum viscosity of 10^{19} Pa.s.

When the mantle material reaches the surface, velocities decrease and the time steps increase. Although the FSSA technique is implemented (section 3.7) the code still becomes unstable and the surface starts to oscillate (figure 12).

Although these parameters resulted in a successful subduction with a similar setup for Garel et al. (2014), these parameters are not able to create subduction in our model. We have to take into account that Garel et al. (2014) uses a very complex mesh, contrary to our simple course mesh. This has strong effects on strain localization, influencing the result. The rheological parameters should thus be altered in a way successful subduction is obtained with our code.

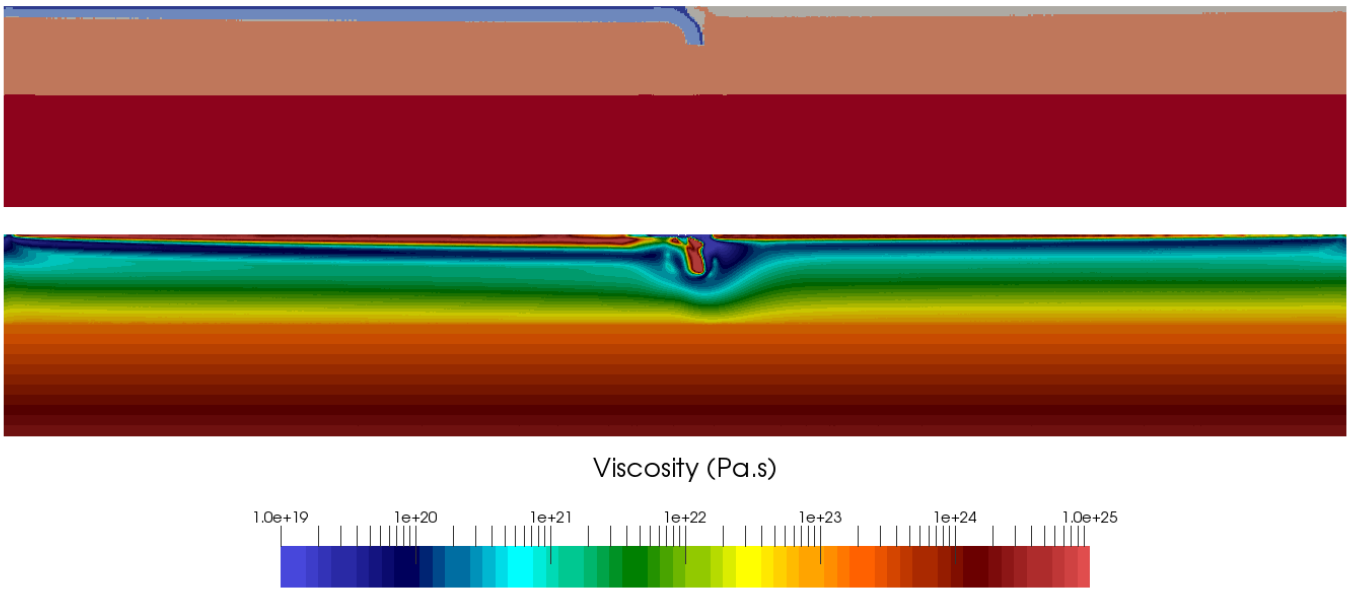

Figure 11: Result run E_Garel after 9 Myr. Top: material field, bottom: viscosity field. Legend for viscosity will be similar for the following figures.

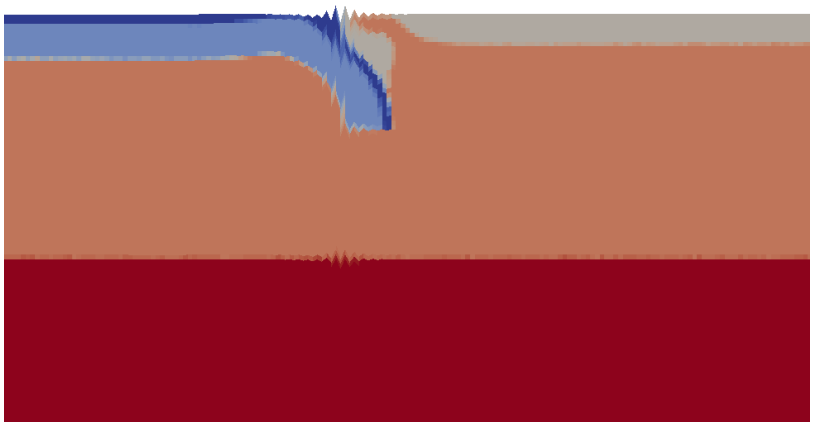

Figure 12: Result of material field of run E_garel after 12 Myr. Mantle material has hit the surface and oscillations start.

4.1.2 Run E_11jan

For the oceanic crust to function as a shear zone between the plates, the yielding strength of the oceanic crust had to be decreased. Together with tuning the activation energy and activation volume of dislocation creep (table 4, labeled E_11jan), a subduction system was created. The location of the trench was moved to x=3000 km and to maintain a similar age gradient through the SP, the age at the left boundary increased to 40 Myr.

Figure 13 shows the result of run E_11jan over 85 Myr. For the full run see movie A.1.1.

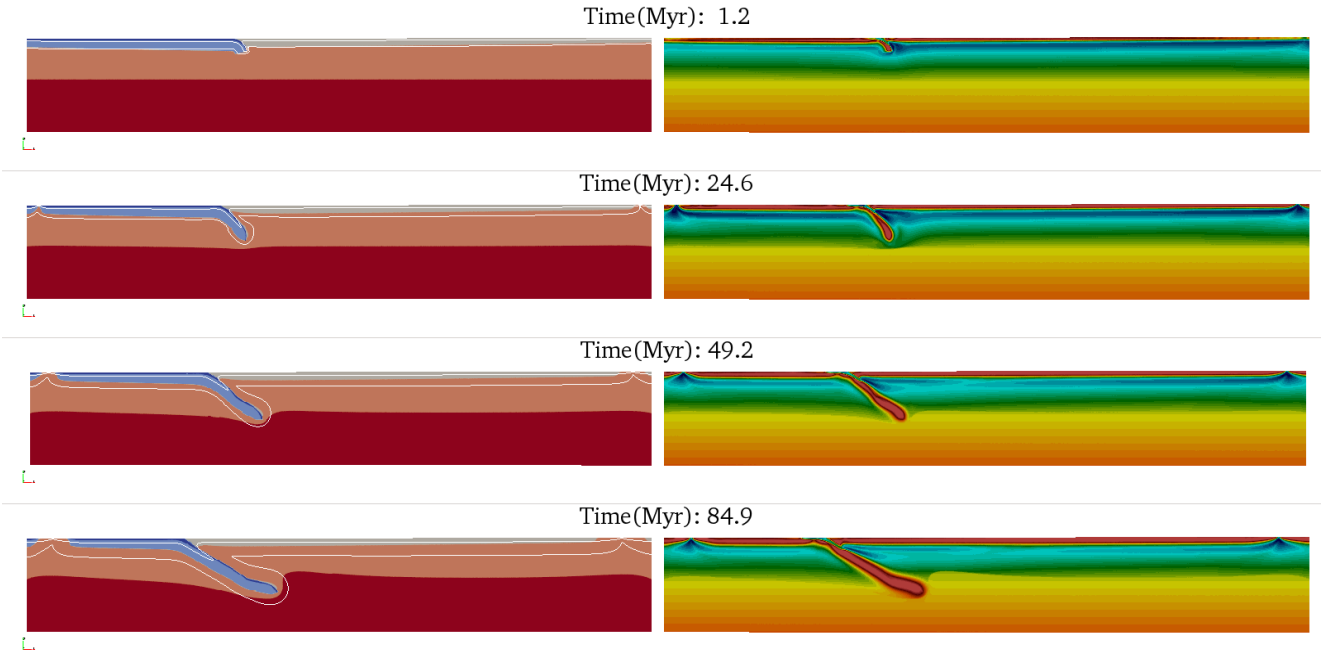

Figure 13: Snapshots of the result of run E_11jan over various times. Left: material field, right: viscosity. The two white lines represent the 700° C and 1300° C isotherms. White lines in any following figure present the same.

Initially the plate sinks down vertically into the upper mantle. The oceanic crust is weak enough to function as a concentration of strain and a thin zone of low viscosity is created between the plates making it possible for the subducting plate to move along the overriding plate (figure 14). At this low viscosity tunnel the viscosity is roughly $10^{20} Pa.s$ and strain rate is significantly high (up to $3.10^{14} s^{-1}$, figure 15).

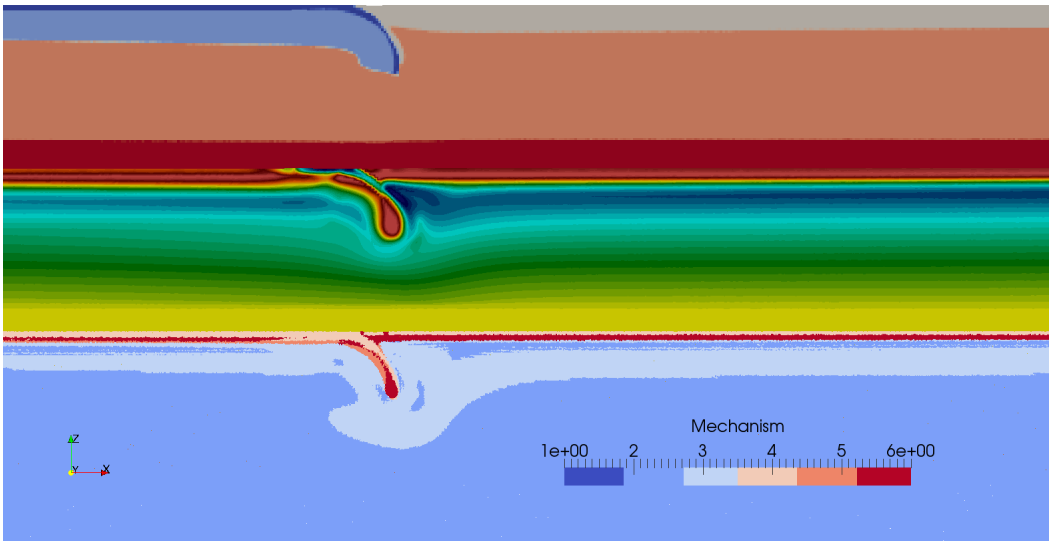

Figure 14: Result of run E_11jan after 15 Myr. Top: materials, middle: viscosity, bottom: deformation mechanism. Mechanism 1= minimum viscosity, 2= diffusion creep, 3= dislocation creep, 4= yield strength, 5= Peierls creep, maximum viscosity.

The bottom figure of figure 14 shows the dominant deformation mechanisms. Along the oceanic crust and shear zone the yield strength dominates (mechanism 4). This is expected as the oceanic crust has a low angle of friction and cohesion. Peierls creep (mechanism 3) is dominant in the deeper part of the slab, promoting bending of the slab at depth. Around the tip and in the upper part of the upper mantle dislocation creep is the dominant deformation mechanism (mechanism 3), comparable to the areas of high strain rate (figure 15). The rest of the upper and lower mantle is dominated by diffusion creep (mechanism 2) and shows a fairly layered viscosity field.

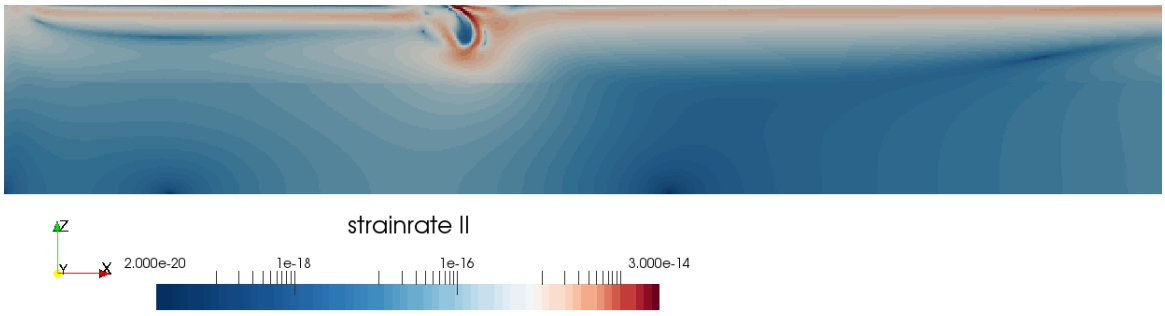

Figure 15: Strain rate (s^{-1}) after 15 Myr.

As the plate sinks ridges form on the sides of the domain both in the subducting and overriding plate (figure 13). These ridges form as the lithosphere is youngest thus thinnest at the sides so mantle material can easily penetrate to the surface, detaching the plates from the sides. This promotes subduction as it allows plate motion in both the SP and OP (figure 16). This system forms two convection cells through the domain: one underneath the SP and one underneath the OP (figure 16). The motion is however slow, with a maximum velocity of 2 cm/yr at 50 Myr. This maximum velocity is observed in the returnflow, just below the OP, causing the trench to roll back as the slab continues to sink.

After 50 Myr the slab has reached the upper-lower mantle (ULM) boundary. Instead of flattening out above or penetrating through the lower mantle, the slab pushes the lower mantle aside, deforming the ULM boundary. Through time (figure 13) the slab continues to push against the lower mantle and as it flattens out, a bulge of lower material is piled up in front of the tip and the ULM boundary is nothing but a linear boundary anymore.

Figure 17 shows the surface variation after 50 Myr. At the trench and at the ridges there is a clear topography created. The ridges cause elevation of a few hundred meters while the trench causes a deep through of a few kilometers. This topography is relatively stable and remain within expected limits.

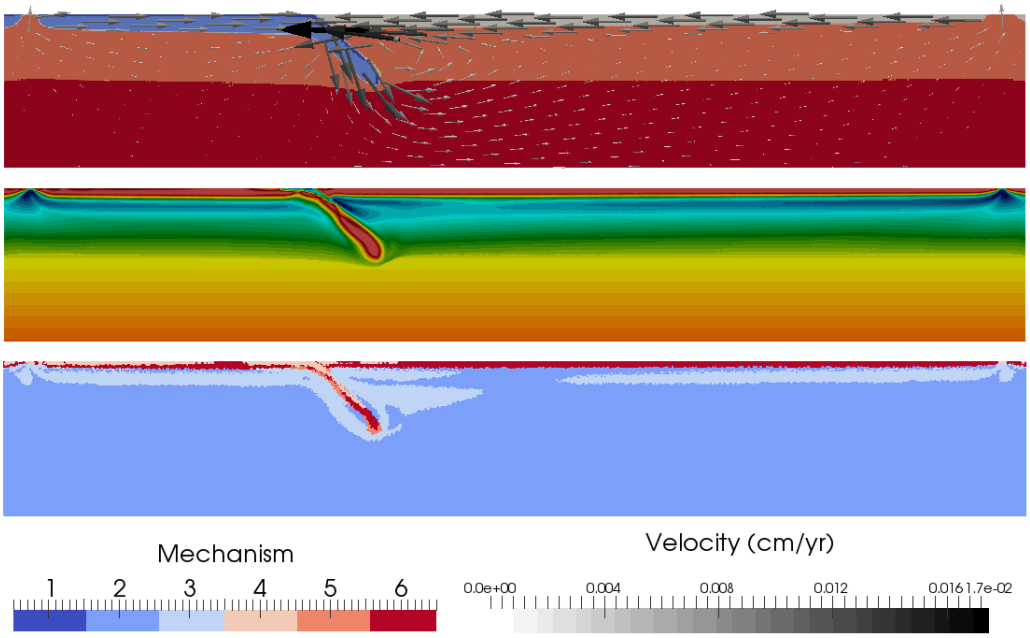

Figure 16: Result of run E_11jan after 50 Myr. Top: materials with velocity arrows, middle: viscosity, bottom: mechanism.

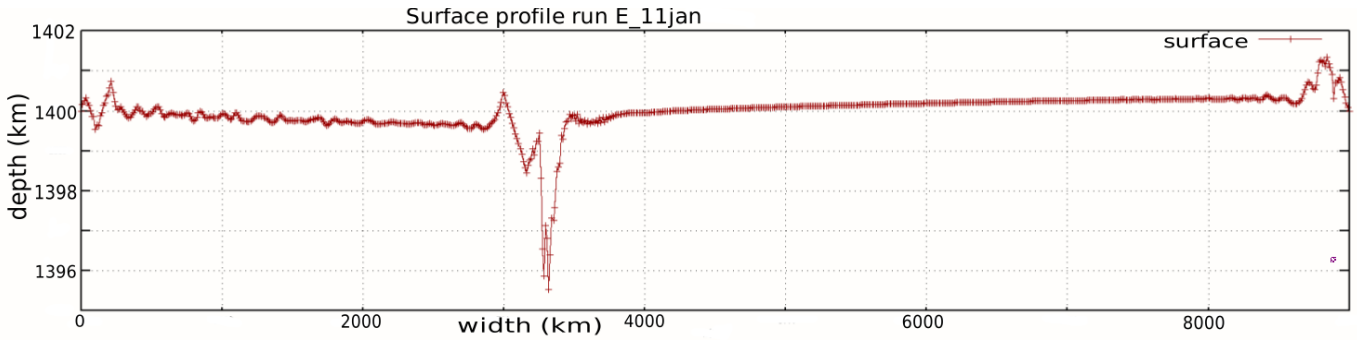

Figure 17: Surface variation at 50 Myrs of run E_11jan.

4.1.3 Run *E_19jan*

The next step is to impose a plate velocity using equation 23. Figure 18 shows the result of run *E_19jan* after 78 Myrs, where a constant plate velocity of 1.0 cm/yr was imposed to the SP. For the full two runs see movie A.1.3.

The first part of the run goes as expected; the slab sinks into the the mantle, creating a ridge when the sinking velocity exceeds the imposed velocity. When the slab reaches the lower mantle, the sinking velocity decreases and the imposed velocity exceeds the sinking velocity. As a result of the continuing imposed plate velocity, subduction is initiated at the ridge, instead of a continuation of subduction at the trench (figure 18). The lithospheric plate is thus not strong enough to obtain its shape when the imposed velocity exceeds the pulling velocity of the slab.

By increasing the angle of friction in the oceanic crust (table 4, run *E_13jan*), the slab remains rigid enough to transfer the ridge without changing its shape (figure 19). Increasing the yield strength also alters the morphology of the slab as its viscosity is increased.

Due to the imposed velocity the slab approaches the lower mantle in a more vertically position, again pushing the LM aside.

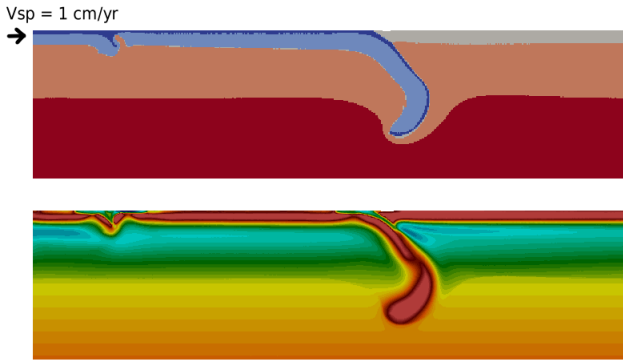

Figure 18: Snapshot of run E_19jan with $\phi(WZ) = 0.5$ in the OC. Upper diagram: material field, bottom diagram: viscosity field.

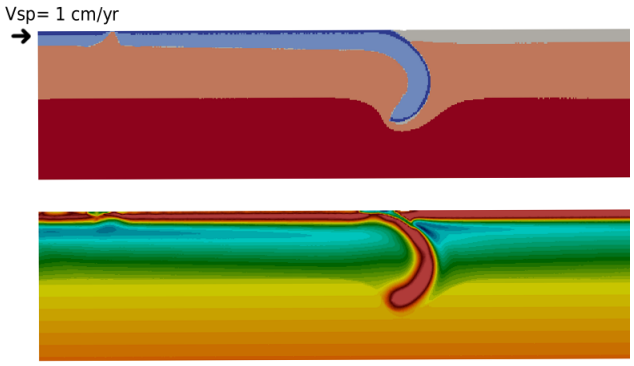

Figure 19: Snapshot of run E_19jan with $\phi(WZ) = 0.7$. Upper diagram: material field, bottom diagram: viscosity field.

4.1.4 Tuning UM and LM viscosity

In an attempt to solve the lower mantle problem, the viscosity of the lower mantle is varied. Figure 20 shows the result of three runs, each with another viscosity profile for the lower mantle. The top figure has a constant effective viscosity for the lower mantle of 10^{22} Pa.s, the middle a viscosity of $1 - 2 \cdot 10^{22}$ Pa.s and the bottom a viscosity of $3 - 10 \cdot 10^{22}$ Pa.s, similar to run E_11jan. With implementing a lower LM viscosity, the slab can push the lower mantle more easily down and deform the boundary than with a higher LM viscosity. The boundary remains deformed and impermeable. For the full runs these models see movie A.1.2.

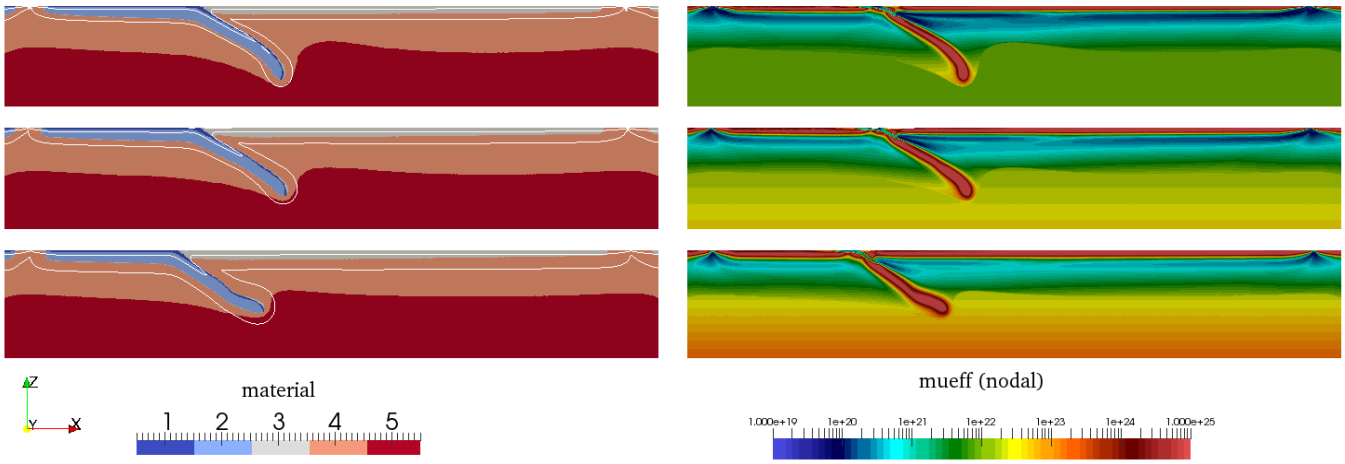

Figure 20: Snapshots of three runs with varying lower mantle viscosity. Top figure: $\mu_{eff}(LM) = 10^{22}$ Pa.s, middle figure: $\mu_{eff}(LM) = 1 - 2 \cdot 10^{22}$ Pa.s, bottom figure: $\mu_{eff}(LM) = 1 - 10 \cdot 10^{22}$ Pa.s

.

To obtain a reference on the viscosity of the domain, the vertical viscosity profile of our runs was compared to the viscosity profile generated by Čížková et al., 2012 (figure 21). The viscosity profile of E_11jan is measured after a single time step at x=6000 km, 3000 km from the trench. At this stage the lithosphere and mantle are little influenced by the sinking slab.

Compared to Čížková et al., 2012, the viscosity profile of E_11jan is higher in both the upper and lower mantle. Also the viscosity jump between the upper and lower mantle is minimal. The viscosity profile of run E_garel is also included, showing even higher viscosity values.

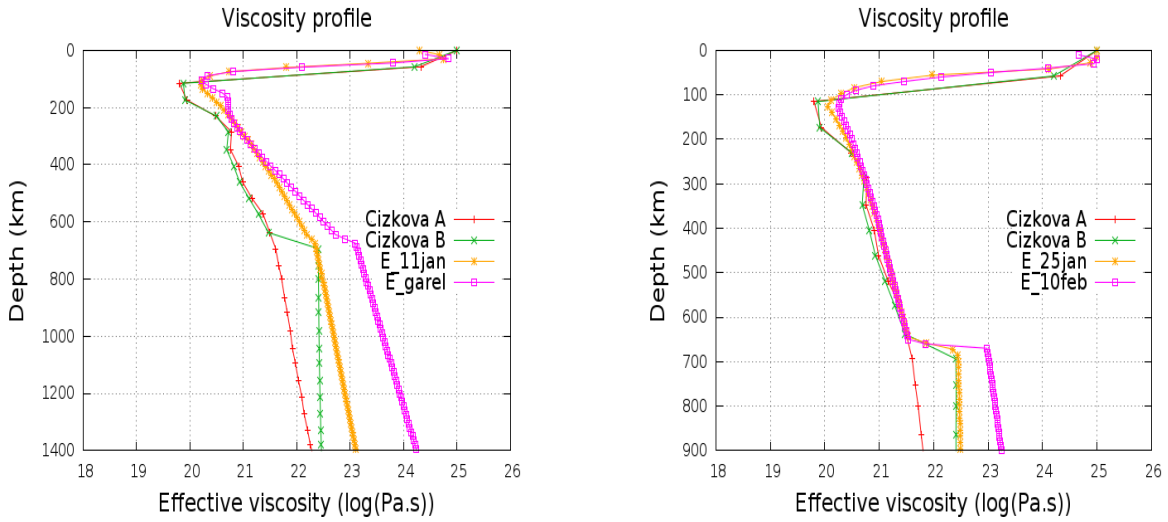

Figure 21: Initial viscosity profiles at x=6000 km (3000 km from trench). Left: E_11jan (yellow) and E1_garel (purple). Right: E_25jan (yellow) and E_10feb (purple). Added are the viscosity profiles generated by Čížková et al., 2012 (A (red) and B (green)).

4.1.5 Run *E_25jan*

For run *E_25jan* the parameters are tuned to obtain a similar viscosity profile as Čížková et al., 2012 (yellow line figure 21b). The values as listed in table 4, labeled *E_25jan*, and the result is shown in figure 22.

The slab sinks down towards the lower mantle, where after it breaks off at the hinge and the slab remnants sinks down on top of the lower mantle.

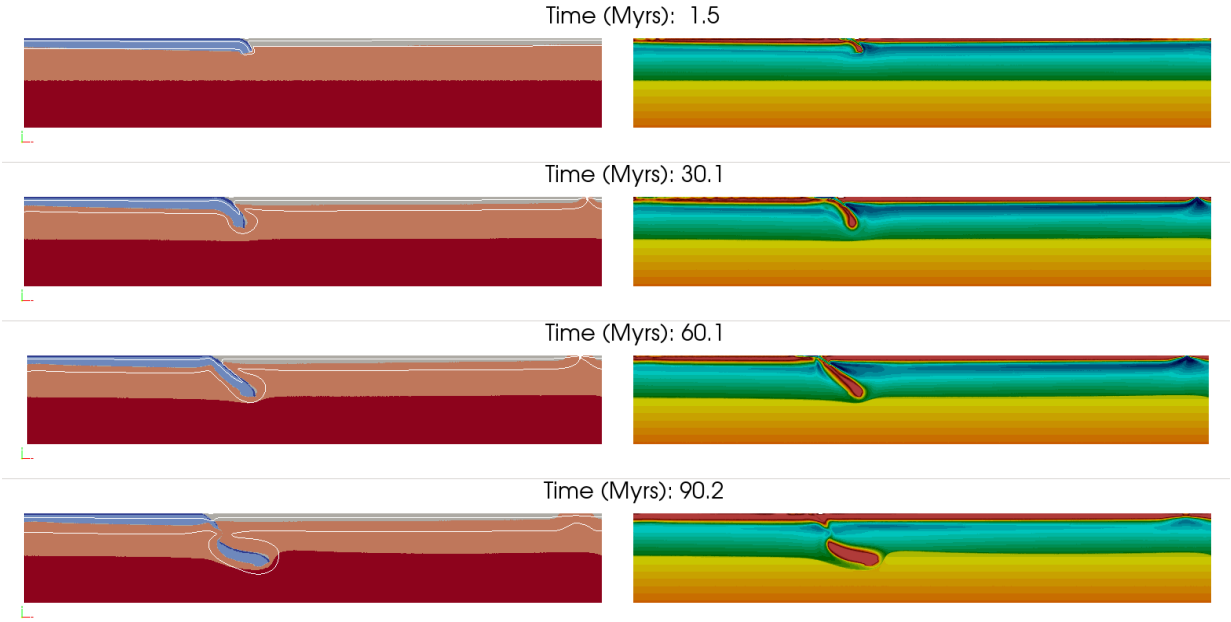

Figure 22: Snapshots of the result of run E_25jan at various times. Legend same as figure 20.

4.1.6 Run *E_26jan*

To prevent the slab from breaking off, the yield strength of the lithospheric plates is increased (table 4, run *E_26jan*). This results in the model shown in figure 23.

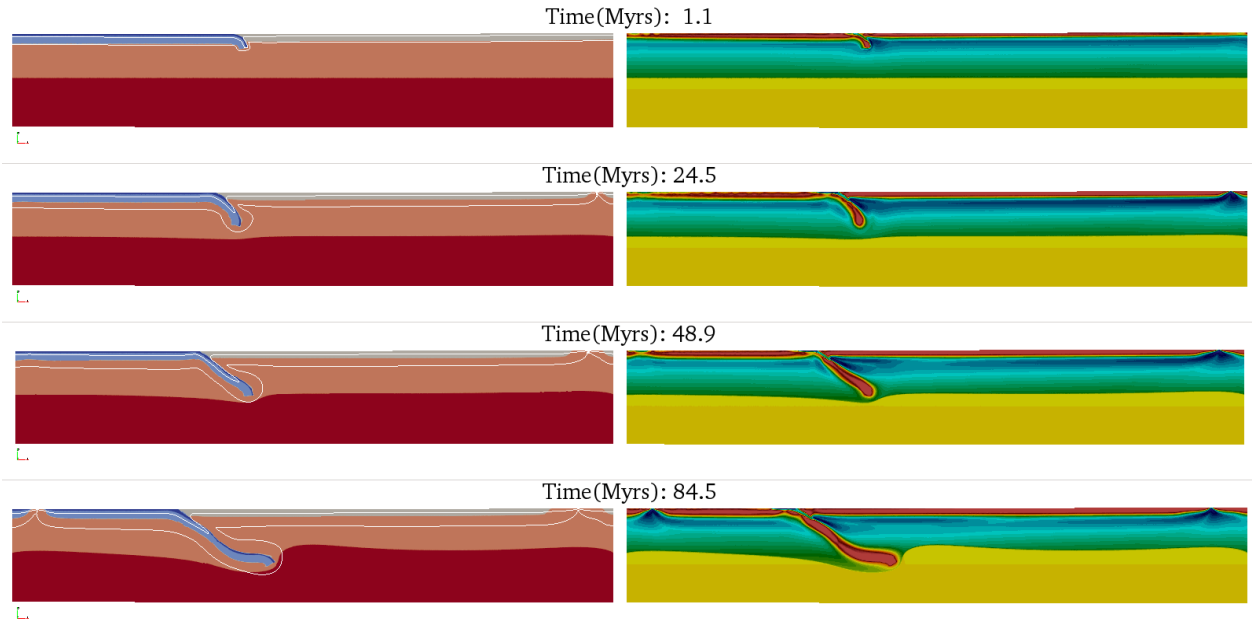

Figure 23: Snapshots of the results of run E_26jan at various times. Legend same as figure 20.

With these parameters a similar subduction model is created as by E_11jan. The slab sinks in a similar matter over a similar time frame. Only a smaller ridge forms in the SP and a more horizontal positioning of the slab is created (figure 23, bottom figure). Although there is a higher viscosity jump between the LM and UM, lower viscosity in the UM and LM are more rigid, the result is similar. Different combinations of rheological parameters can thus resolve in a similar result.

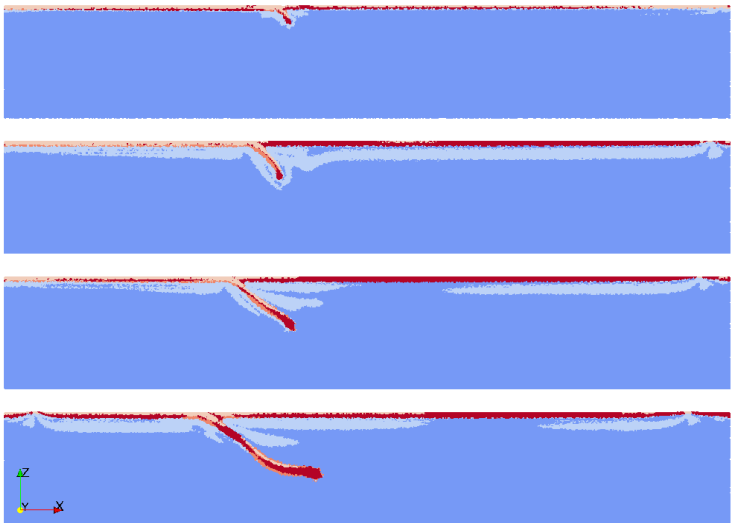

Figure 24: Dominant mechanism per snapshot of run E_26jan shown in figure 23. Legend same as figure 20.

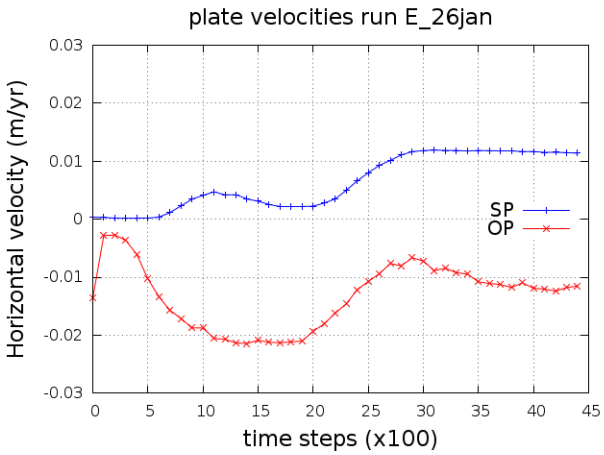

Figure 25: Horizontal velocity of the OP and SP for run E_26jan.

Figure 24 shows the dominant mechanisms over the domain for the various time steps presented in figure 23. When the slab has sunken around 500 km depth, diffusion creep takes over dislocation creep around the tip of the slab slab as the lower mantle causes a decrease in velocity at the tip of the slab. Yield strength stays dominant around the hinge and Peierls creep dominates where bending of the strong slab occurs.

Figure 25 gives the velocity of the OP and SP through the run. In the first part of the run the OP moves with a velocity of 2 cm/yr towards the trench and as the velocity of the SP is still low, it created significant rollback. When the a ridge is also created in the SP the velocity in the SP increases, decreasing the motion of the OP.

4.1.7 Run E_3feb

Again a plate velocity of 1.0 cm/yr is imposed to the SP. The result is shown in figure 27. As expected the slab sinks faster than without an imposed plate velocity and a similar result is obtained to run E_19jan. For the full run see movie A.1.4.

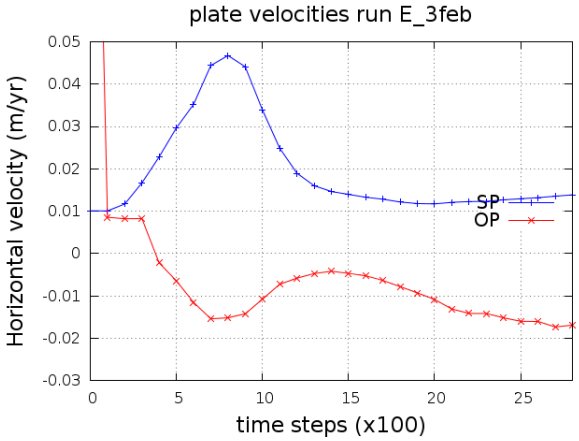

Figure 26: Horizontal velocity SP and OP of run E_3feb.

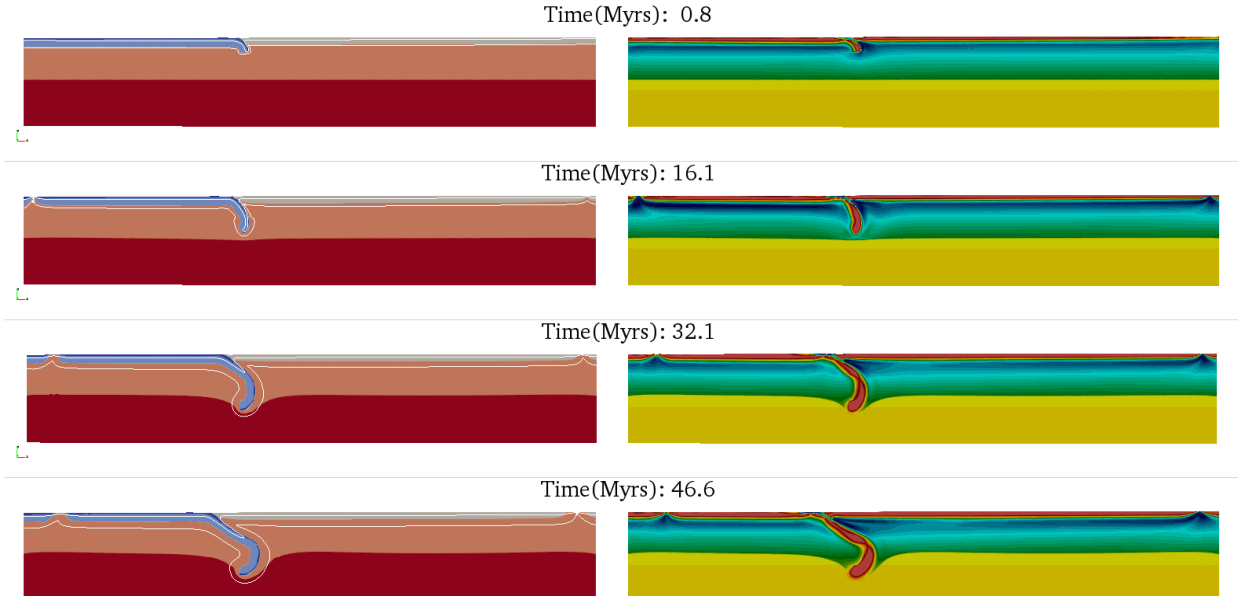

Figure 27: Snapshots of the results of run E_3feb at various times. Legend same as figure 20.

Figure 26 gives the plate velocities of run E_3feb. The velocities of both the SP and OP increase when the slab sinks through the UM by the combination of slab pull and ridge push. When the slab approaches the LM the velocity decreases and the velocity of the SP decreases to the imposed velocity of 1 cm/yr. The velocity of the OP is less stable but increases slowly through time.

4.1.8 Run E_10feb

Another option to modify the behaviour of the LM is to change the dominant deformation mechanisms in the LM. Although seismic observations have proposed that diffusion creep is the dominant deformation mechanism in the LM, this does not mean that dislocation creep can locally decrease the viscosity when strain is increased (when a slab approaches). In run E_10feb I thus implemented dislocation creep as a possible deformation mechanism in the lower mantle. The overall viscosity of the LM is increased to $10^{23} Pa.s$. Figure 28 gives the result.

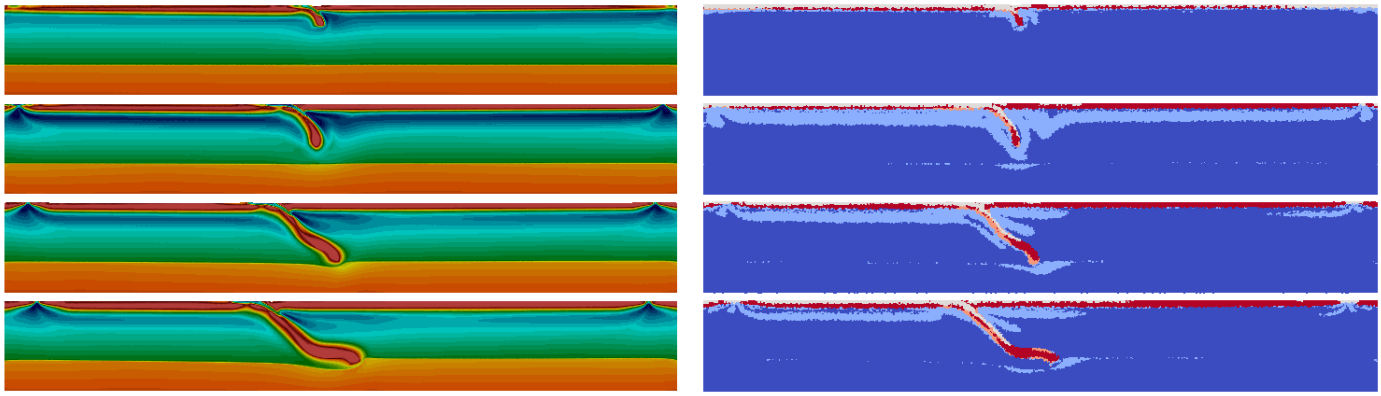

Figure 28: Result of run E_10feb at 0 Myr, 25 Myr, 44 Myr and 73 Myr. Left: viscosity field, right: dominant deformation mechanism.

When the slab approaches the LM, a local decrease in the viscosity of the LM can be observed, decreasing the viscosity further the slab sinks. The increased viscosity causes the boundary only to locally indent, however the ULM boundary remains deforms, although the effect is decreased.

4.2 Section 2: Ocean-continent subduction

The following section describes the results obtained from the runs of section 2, as shown in green in Figure 9. It represents a continent-oceanic subduction zone, comparable to the setting of the South Sandwich subduction system, as described in section 1.2 for the setup shown in Figure 8. The runs are subdivided into sections. These sections are given in white boxes in Figure 9. Within these sections I will again describe and discuss every run separately and put forward the problems faced.

In this setup the oceanic overriding plate is replaced by continental lithosphere of constant age. No plate motions are imposed, so the side boundaries, as well as the bottom boundary is free slip. The top boundary is again free surface. *something with subducting plate underneath OP.* Figure 29 gives the initial conditions of run *E_13mrch* in terms of a) materials, b) temperature field and c) density field. Table 5 gives the rheological parameters for each material. These parameters will be used in the following runs, unless stated otherwise. Figure 29d gives the viscosity field created by these parameters after 1 Myrs.

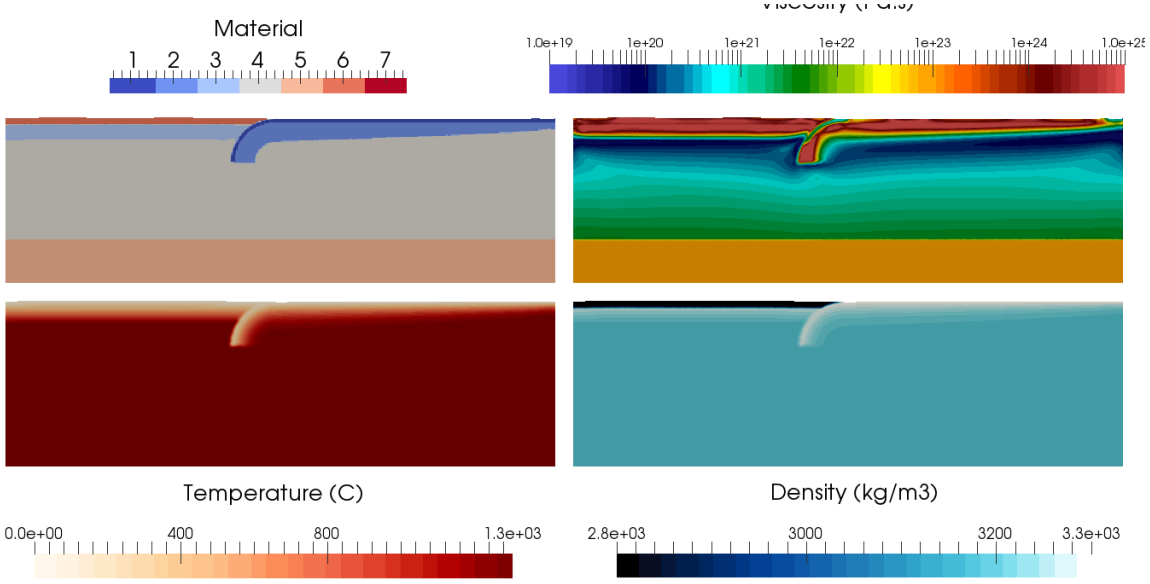

Figure 29: Begin conditions of run E_13mrch. a) Material field: 1= oceanic crust (OC), 2= oceanic lithospheric mantle (20-80 Myr, SP), 3= continental lithospheric mantle (OP), 4= upper mantle (UM), 5=lower mantle (LM), 6= continental crust (CC), 7= weak zone (WZ, absent). b) Temperature field (°C), c) Viscosity field (Pa.s), d) density field (kg/m^3). Legend similar for following figures.

4.2.1 Run *E_13mrch*

For run *E_13mrch* the age of the oceanic lithosphere at the right border is set to 20 Myr. The result of run *E_13mrch* over 7.5 Myr is shown in figure 30.

There is a strong age gradient in the subducting plate: 20-80 Myr over 1500 km. This causes a strong difference in temperature and density gradient between the side of the domain and the trench. As the lithosphere is thin on the right side of the domain (20 Myr), the lithosphere is weak and a ridge can easily form. When the ridge has formed after 2.5 Myr, the oceanic lithosphere is free to move from the side. Because of the strong gradient in density, the sinking velocities accelerates to 25 cm/yr after 7.5 Myr (Figure 30).

A convection cell is formed between the sinking slab, the flow of mantle material towards the ridge and the oceanic plate moving towards the trench. This causes the slab to make a circular motion back towards the right, creating a subduction system comparable to the Advancing Mode defined by Schellart, 2008 (Figure 1). As the viscosity increases with depth it is easier for the slab to move back towards the right than to sink further down.

No ridge forms in the continental lithosphere as there is no weak lithosphere, so little movement is seen on the right side of the domain. Minimal returnflow is observed at the wedge.

Table 5: Values viscosity parameters in equation 28 for various runs. Bold numbers vary from the other materials.

Material	OP(3)	SP (2)	CC (4)	OC (1)	UM (5)	LM (6)	WZ (7)
dislocation creep							
A (Pa^{-n}/s)	$5 \cdot 10^{-16}$	$5 \cdot 10^{-16}$	$\mathbf{1.1 \cdot 10^{-28}}$	$5 \cdot 10^{-16}$	$5 \cdot 10^{-16}$	$\mathbf{10^{-42}}$	$\mathbf{1.1 \cdot 10^{-28}}$
Q (kJ/mol)	560	560	**223**	560	560	**540**	**223**
V (cm^3/mol)	10	10	**12**	10	10	**12**	**12**
n	3.5	3.5	**4**	3.5	3.5	3.5	**4**
diffusion creep							
A (Pa^{-n}/s)	$3 \cdot 10^{-11}$	$3 \cdot 10^{-11}$	$3 \cdot 10^{-11}$	$3 \cdot 10^{-11}$	$3 \cdot 10^{-11}$	$\mathbf{2 \cdot 10^{-16}}$	$3 \cdot 10^{-11}$
Q (kJ/mol)	300	300	300	300	300	**220**	300
V (cm^3/mol)	5	5	5	5	**2**	**0.2**	5
n	1	1	1	1	1	1	1
Peierls creep							
A (Pa^{-n}/s)	10^{-150}	10^{-150}	10^{-150}	10^{-150}	10^{-150}	$\mathbf{10^{-300}}$	10^{-150}
Q (kJ/mol)	540	540	540	540	540	540	540
V (cm^3/mol)	10	10	10	10	10	10	10
n	20	20	20	20	20	20	20
Yield strength							
ϕ (°)	12	12	**11.31**	**0.7**	12	12	**11.31**
C (MPa)	10	10	10	**2**	10	10	10

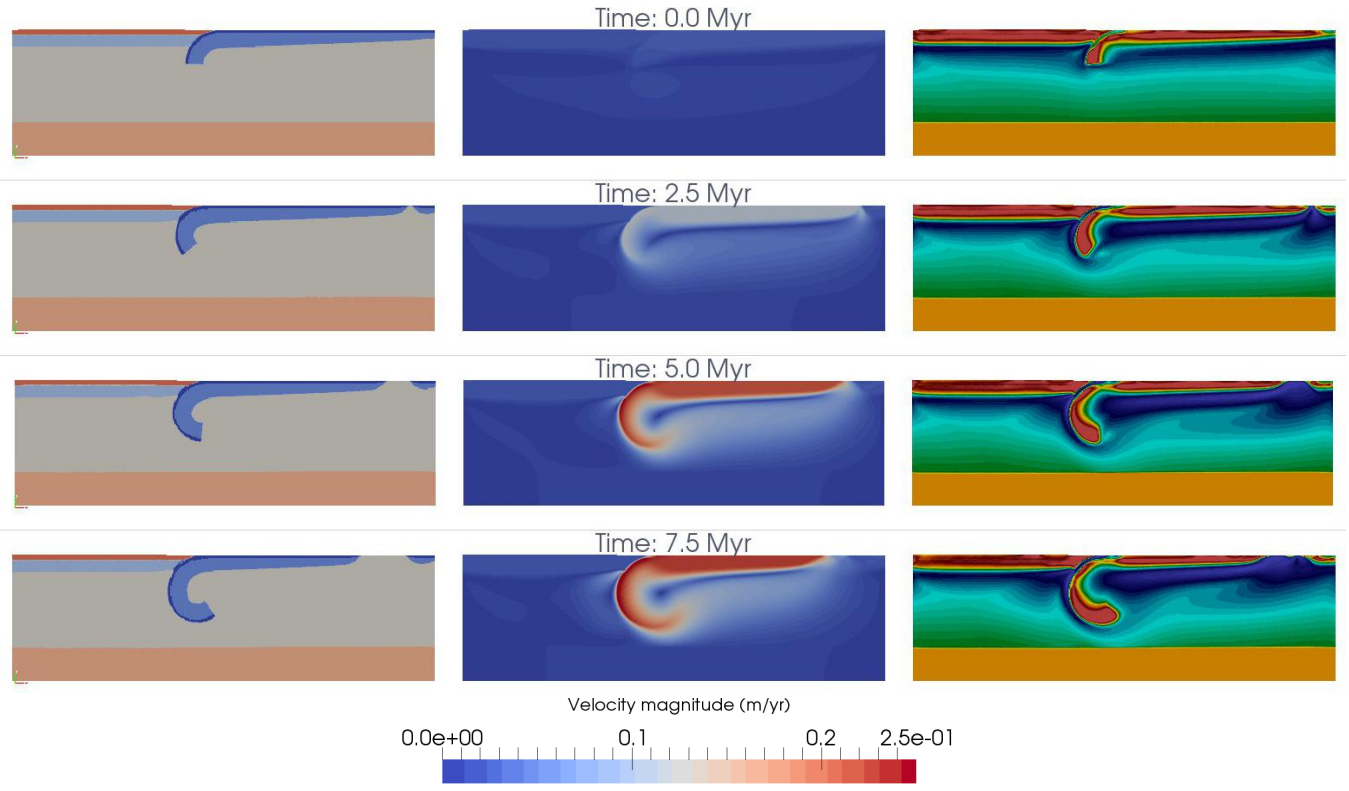

Figure 30: Result of run E_13mrch over 7.5 Myr. Left: material field, middle: velocity field, right: viscosity field.

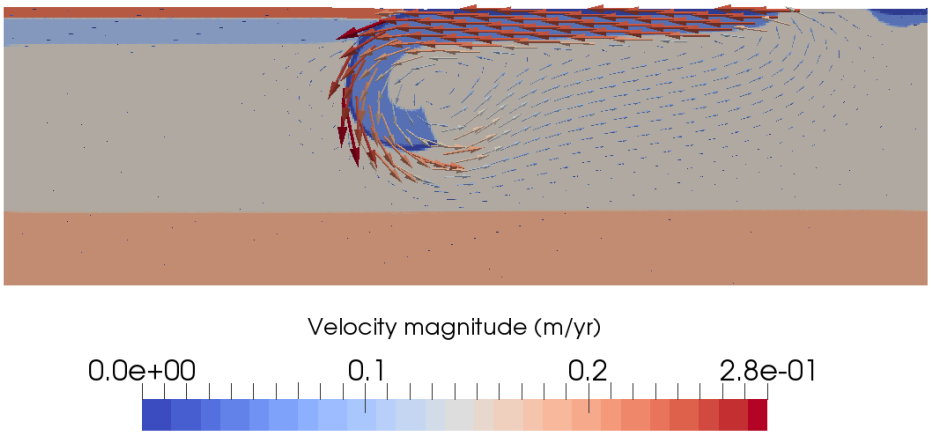

Figure 31: Result of run E_13mrch at 7.5 Myr. Material field with velocity arrows.

4.2.2 Run E_20mrch

Instead of the oceanic crust acting as a weak zone, an weak zone of 20 km wide is added at the contact zone between the OP and SP (WZ, red area in figure 32) and the oceanic crust is decreased to 10 km thickness. The weak zone has the same rheological properties as the oceanic crust (table 5). Moreover the activation volume for dislocation creep, V_{disl}, is increased to 11 cm^3/mol (which is still in the range of realistic values, see table 1), in an attempt to slow down the sinking velocity. The other rheological properties are similar to run E_13mrch.

Figure 32 shows the result of run E_20mrch over 10 Myr.

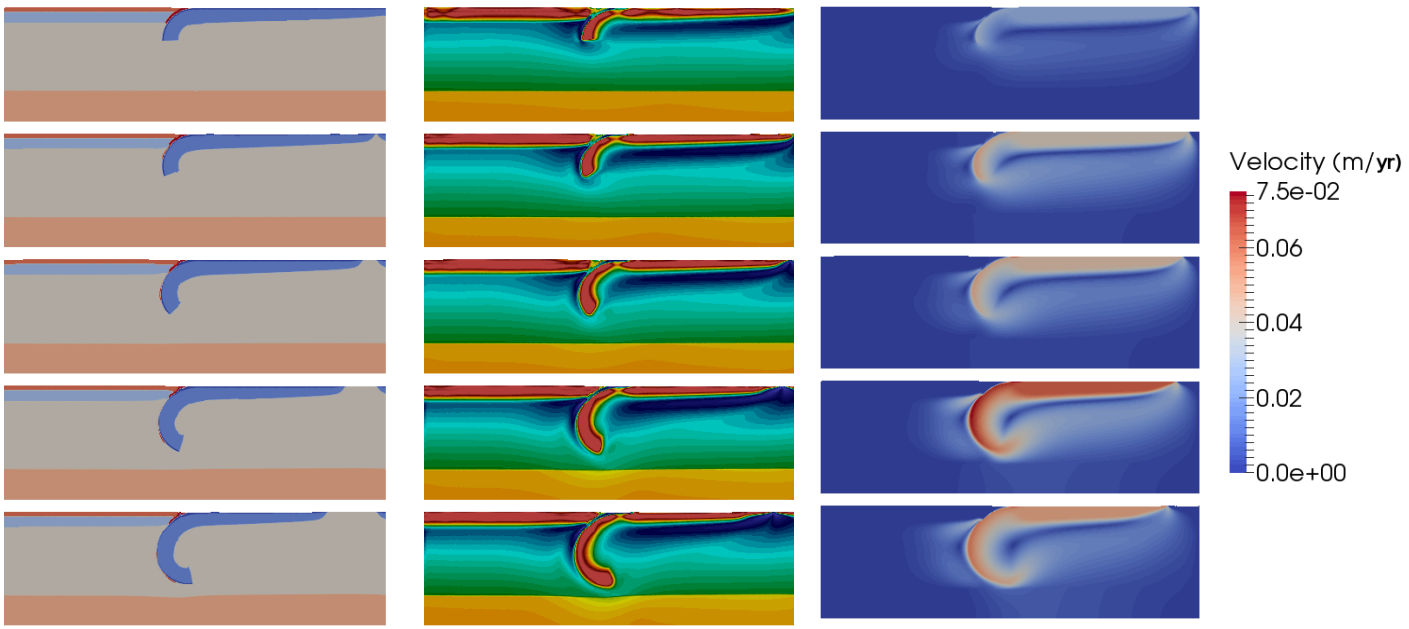

Figure 32: Result of run E_20mrch at (top to bottom): 0 Myr, 2.9 Myr, 5.3 Myr, 7.5 Myr, 9.8 Myr. Left: material field, middle: viscosity field, right: velocity field.

Due to the ridge push and slab pull force of the SP, the SP pushes against the OP and the weak zone gets thinned and partly dragged along with the SP. This causes the viscosity at the contact zone between the plates to increase and thus slowing down the slab, together with the increased activation volume for dislocation creep.

However, the density difference still causes a ridge to form and the slab to accelerate and as it sinks. The maximum

sinking velocity is 7.5 cm/yr. The slab again sinks in a circular motion, creating a convection cell with the opening ridge. The radius of the circle is however increased and the slab sinks down more vertically, reaching the mantle after 10 Myr.

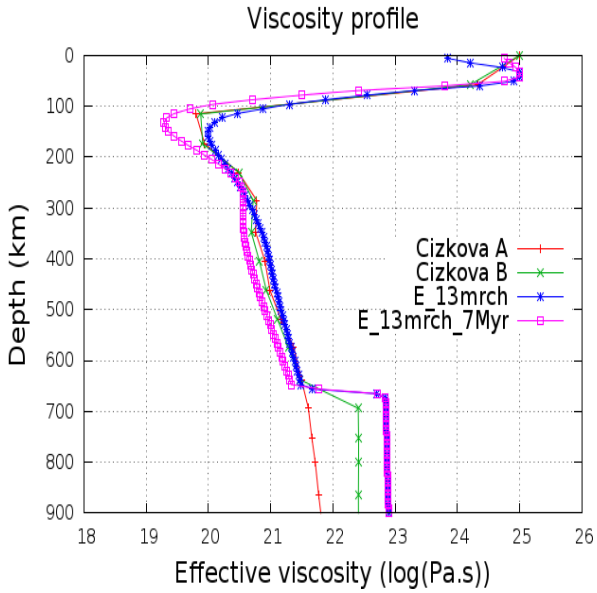

Figure 33: Viscosity profile of run E_13mrch at 1 Myr and 7 Myr vs the viscosity profiles of Čížková et al., 2012.

Constant age oceanic lithosphere

To avoid the acceleration effect due to the disconnection of the plate from the side boundary, the oceanic plate is given a constant age of 80 Myr. Subduction is then only caused by slab pull, not by ridge push. As the oceanic and continental plate are attached to the sides of the domain, the slab can only sink by detaching from the overriding plate and from the surface and rolling back. To promote the slab to detach from the OP, a weak zone of 40 km wide is implemented.

Additionally, the yield strength of the weak zone is lowered to a similar value of the oceanic crust.

Figure 34 gives the begin conditions of this setup in terms of material (left), temperature (middle) and density (right).

Figure 34: Begin conditions section 3. Left: material field, middle: temperature field, right: density field. Legend same as before.

4.2.3 Run *E_29mrch*

Figure 35 shows the result of run *E_29mrch* over 4.5 Myr.

Now that the oceanic lithosphere has a constant age, there is no density gradient towards the trench. The oceanic lithosphere is strong throughout the domain so no ridge can form, preventing any unnatural acceleration.

Instead, mantle material penetrates through the weak zone towards the surface, and a back-arc basin is formed. Because of the low viscosity of the weak zone the mantle material can easily penetrate creating high strain rates and with velocities up to 20-30 cm/yr (36) the mantle material has reached the surface in 3 Myr (Figure 35).

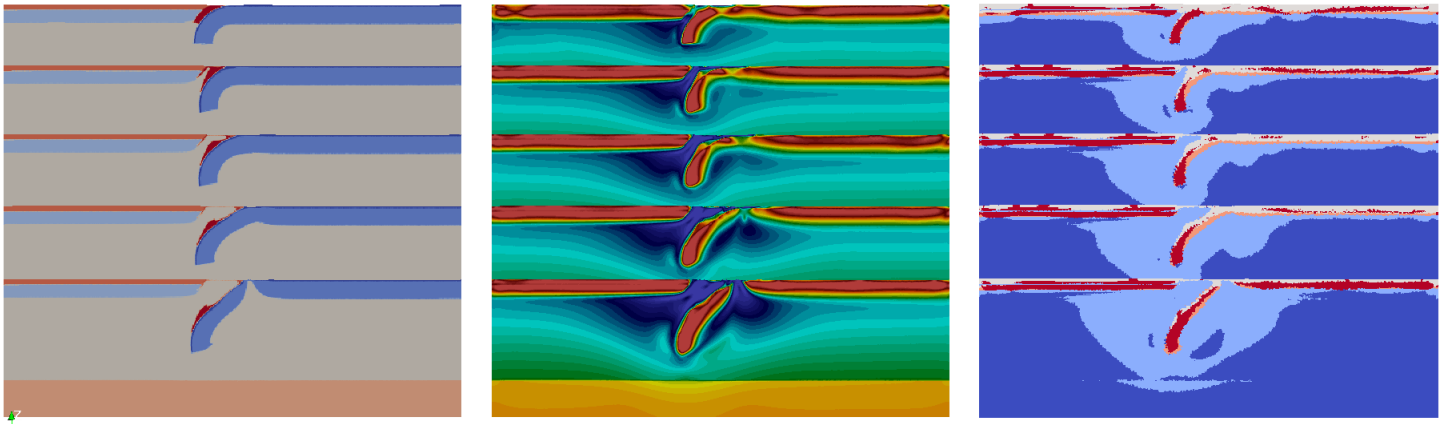

Figure 35: Result of run E_29mrch. Left: material field, middle: viscosity field, right: dominant mechanism. top to bottom: 0 Myr, 2.5 Myr, 3.2 Myr, 3.8 Myr, 4.4 Myr

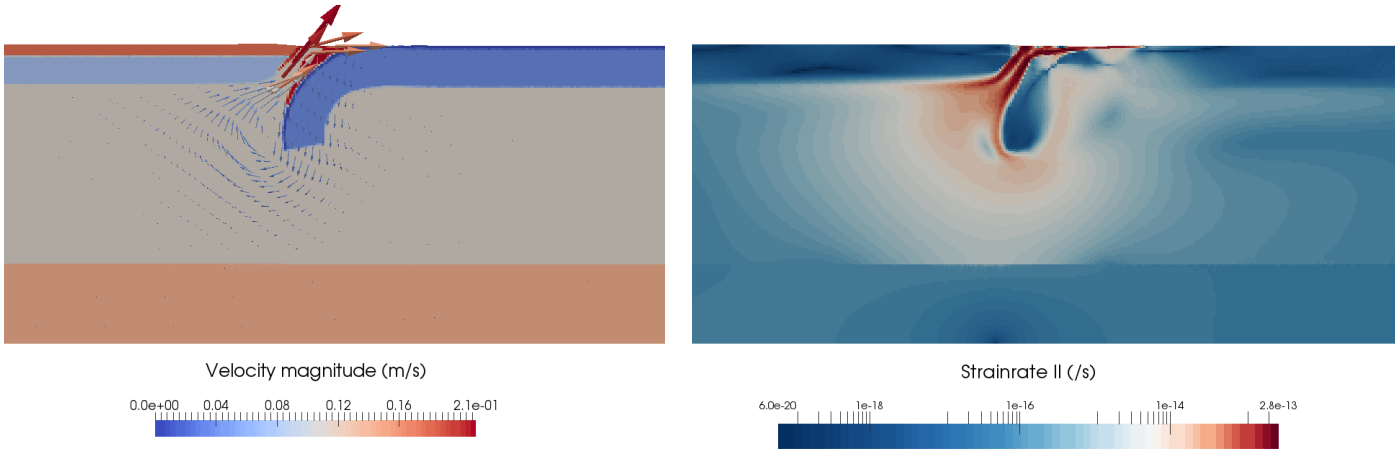

Figure 36: Result after 2.8 Myr. Left: material field with velocity arrows, right: strain rate field.

As the back-arc basin expands, the slab sinks into the mantle and the slab detaches from the surface causing the trench to move backwards, creating rollback. Ideally this rollback would continue as the back-arc basin grows. However, this rollback is only observed until roughly 3.8 Myr, when 120 km of rollback is created. As the slab sinks, strain starts to localize at the hinge, causing the viscosity to decrease significantly here. The lithosphere is weakened locally and the upper mantle material can move up at the hinge (Figure 37). A local convection cell has then formed around the sinking slab, the back-arc basin and the hinge (Figure 37). Eventually this causes the slab to detach from the rest of the oceanic lithosphere around 4.3 Myr and sink (Figure 35).

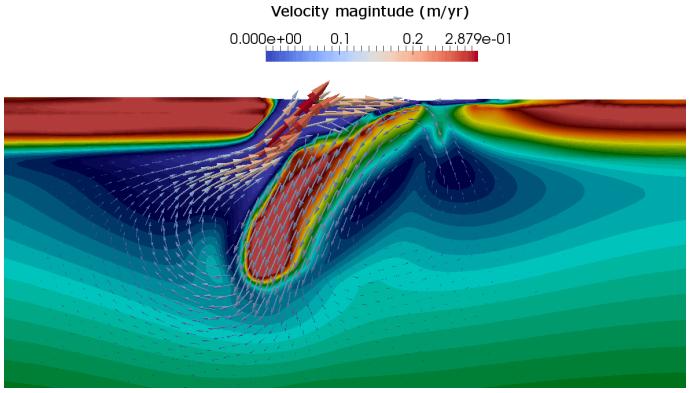

Figure 37: Result of run E_29mrch after 3.8 Myr. Viscosity field with velocity arrows.

4.2.4 Run *E_5apr*

To create further rollback, the slab must detach from the surface but remain attached to the oceanic lithosphere. A returnflow should thus be created in the top of the subducting plate. To facilitate this back flow the oceanic crust is thickened to 20 km and the vertical number of elements is increased to 180 so the elements decreased from 6.7 to 5 km deep. The oceanic crust now consists of 4 elements in thickness. Additionally, the weak zone is set to a constant value of $10^{19} Pa.s$.

Figure 38 shows the result of this run over 1.5 Myrs.

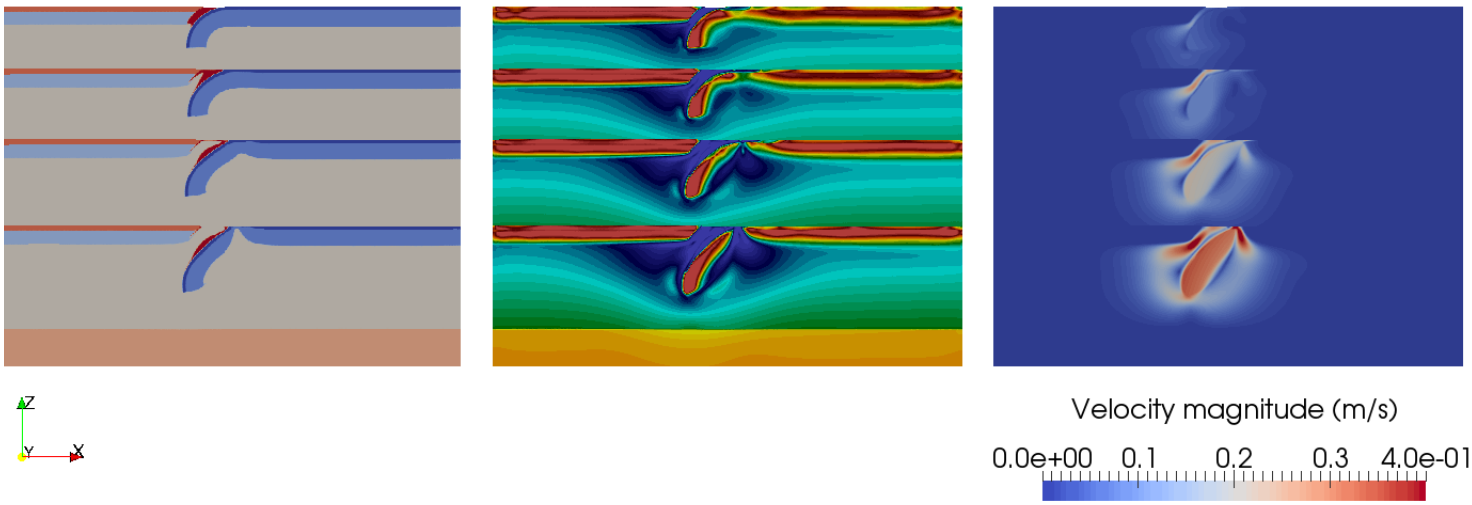

Figure 38: Result of run E_5apr at (top to bottom): 0 Myr, 0.86 Myr, 1.35 Myr, 1.58 Myr. Left: material field, middle: viscosity field, right: velocity magnitude field.

Again, the slab detaches at the hinge. In this run 50 km rollback is observed in 1.35 Myr while the slab has sunken 100 km. Thereafter the slab detaches and sinks and no more rollback is observed.

As the weak zone is set to $10^{19} Pa.s$, the velocity of the mantle material flowing into the back-arc basin is higher than before (Figure 38). Also, as the oceanic crust is increased in thickness, the oceanic lithosphere is weakened (the crust has weaker properties than the lithospheric mantle). This causes the strain to localize faster and after 1.5 Myr the slab has detached and velocities as high as 40 cm/yr are reached.

4.2.5 Run *E_6apr*

In an attempt to prevent the strain to localize at the hinge, the yield strength the lithospheric plates and the oceanic crust is increased. The yield strength of the continental crust is decreased and set equal to the yield strength of the oceanic crust. Table 6 gives the new values of the angle of friction, ϕ, and cohesion, c, which determine the yield strength of the material.

To decrease the velocity of the mantle material entering the mantle wedge, the dislocation activation volume is increased to $12 cm^3/mol$ for all materials. This value is still in the range of realistic activation volumes (see table 1).

Figure 39 shows the result of run *E_6apr*.

Table 6: Values of angle of friction, ϕ, and cohesion, C, used in equation 6 to obtain the yield strength of the material for run E_6apr

Parameter	OP	SP	CC	OC	UM	LM	WZ
Yield strength							
ϕ (°)	**20**	**20**	**3**	**3**	12	12	0.7
C (MPa)	10	10	**4**	**4**	10	10	2

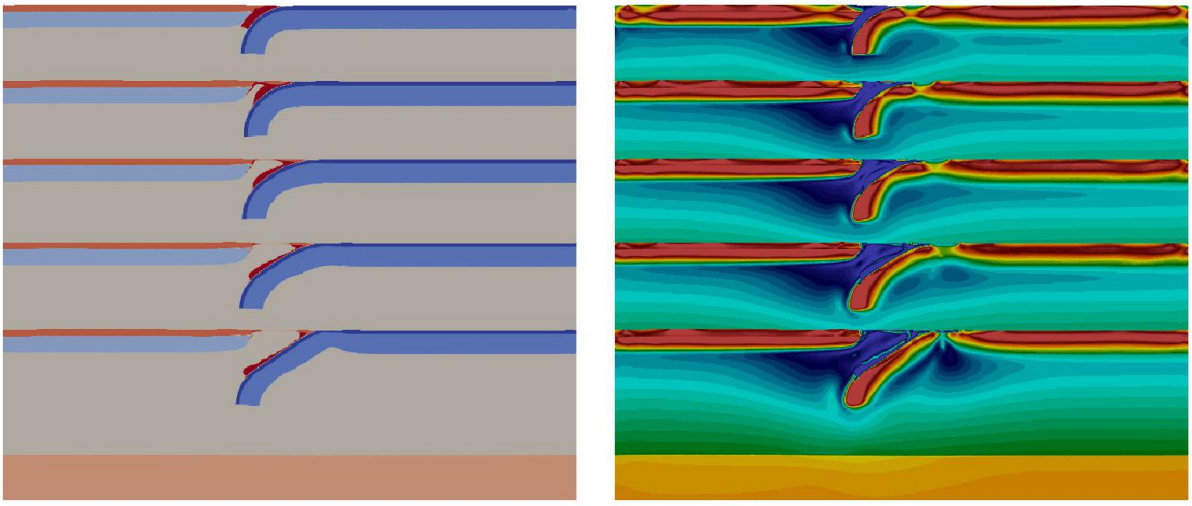

Figure 39: Result after (top to bottom): 0 Myr, 1.1 Myr, 1.8 Myr, 2.6 Myr, 3.7 Myr. Left: material field, right: viscosity field.

The subducting plate is stronger with the increased yield strength as the viscosity at the hinge is higher than in run *E_5apr*. 180 km of rollback is observed in 2.5 Myr while the slab sunk 100 km. The amount of rollback has thus increased compared to the former runs.

However, after 2.5 Myr the strain starts to localize at the hinge and the slab breaks off around 4 Myr (Figure 40. In this time no further rollback is observed as the slab tilts downwards and breaks off.

Due to the increased activation volume of the dislocation creep, the maximum velocity of mantle material penetrating the weak zone is decreased to 27 cm/yr. Strain and strain rate are still high in the wedge causing the viscosity to be low (Figure 40).

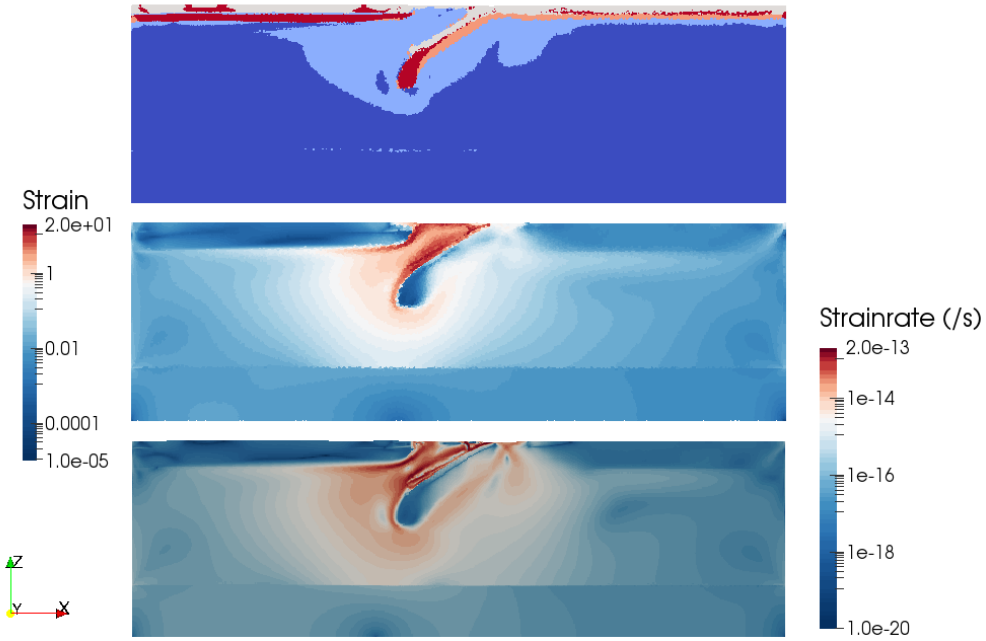

Figure 40: Result of run E_6apr after 3 Myr. Top: dominant deformation mechanism, middle: strain field, bottom: strain rate field (s^{-1}).

Influence of Peierls creep

As explained in section 2, Peierls creep is a deformation mechanism which is important at low temperatures and has a strong dependence on stress (n=20). If the stress is localized at the hinge, Peierls creep will thus be the dominate deformation mechanism here and the viscosity will decrease significantly. In the following runs I will experiment with the effect of Peierls creep on the subduction system. Firstly, I will leave Peierls creep out (run *E_7apr*) and experiment with some variations in viscosity. Secondly, Peierls creep will be implemented only from 100 km onwards, so it cannot effect the hinge (run *E_11apr*).

4.2.6 Run *E_7apr*

In run *E_7apr* Peierls creep is left out as a deformation mechanism. Figure 41 shows the result over 22 Myr. For the full run see movie A.1.5.

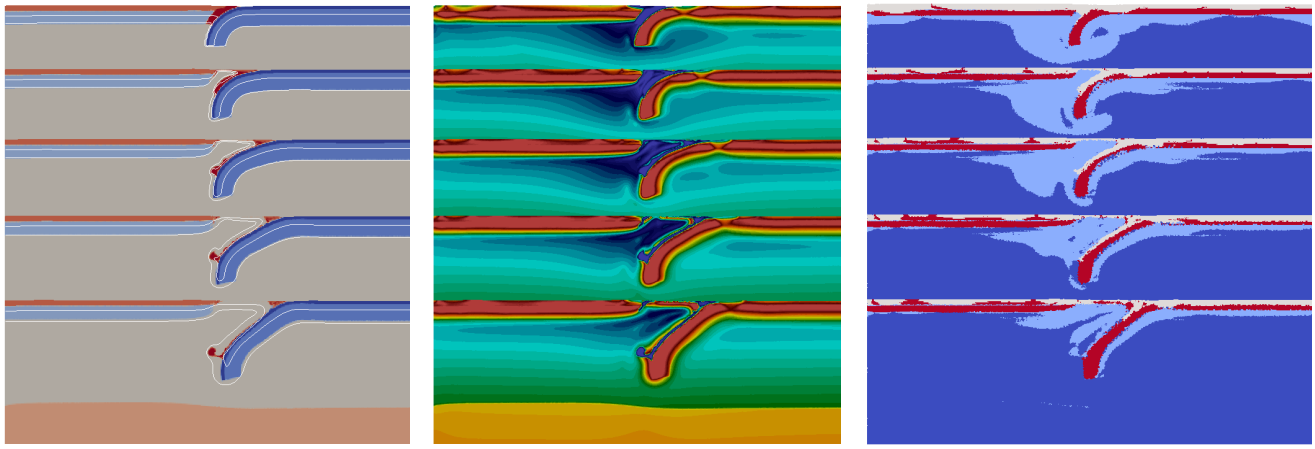

Figure 41: Result of run E_7apr. Left: material field, middle: viscosity field, right: deformation mechanism (mechanism 4 (orange) = peierls creep is absent). White lines are 700 and 1200 °C isotherms. Top to bottom: 0 Myr, 2.5 Myr, 5.5 Myr, 12 Myr 22 Myr

In the first 7.5 Myrs 250 km of rollback is observed, while the slab sinks 140 km. The sinking velocity is on average 2 cm/yr and the rollback velocity around 3 cm/yr. As Peierls creep is absent, the viscosity in the hinge stays high as the slab sinks and rolls back. The viscosity at the hinge remains lower than the rest of the SP (Figure 41). Without Peierls creep, yield strength is the dominant deformation mechanism at the hinge and over time the viscosity does not decrease further, preventing slab break off.

The absence of Peierls creep also increased the viscosity in the slab itself. This makes it more difficult for the slab to deform and thus to bend and sink. The slab sinks slower than at the former runs and the maximum velocity of mantle material flowing into the wedge is 18 cm/yr.

After 7.5 Myr the rollback ceases, but the slab continues to sink deeper by tilting downwards. From 7.5 - 22 Myr only an extra 40 km of rollback is observed and the slab sinks another 100 km to a depth of 500 km. The average sinking velocity has decreased to 1 mm/yr. The velocity with which the mantle material moves into the back-arc basin is also slowed down significantly. At 15 Myr this is maximal 2.5 cm/yr (Figure 42). At the surface of the back-arc basin the velocity has decreased to 4 mm/yr.

After 15 Myr the temperature at the surface of the back-arc basin has decreased and so has the strain rate (Figure 42). This together has caused the viscosity at the surface of the back-arc basin to significantly increase to the maximum viscosity of 10^{25} after 15 Myr. Thus preventing any further motion at the surface of the back-arc basin.

Instead, the slab tilts slowly and the sinking velocity decreases as it sinks through the mantle. This is caused by several factors. Firstly, the high viscosity of the slab causes high resistance to bending and tilting further downward. Secondly, the only place where the displaced material can go into the back-arc basin. However as the slab approaches the lower mantle, the material at the right side of the domain is more difficult to be displaced. It has to either move between the slab and the lower mantle towards the back-arc basin, or move through the lower mantle, which is highly viscous. These factors cause the sinking velocity to slow down significantly until the slab diffuses out. Figure 43 visualizes the velocity field at 22 Myr.

As the viscosity of the weak zone is set at a constant value of $10^{19} Pa.s$, it will remain so throughout the run. For this reason the weak zone (red area in figure 41) can easily get moved around the domain. In this run it moves up with the returnflow creating a 'wobble' of weak zone at the tip of the slab.

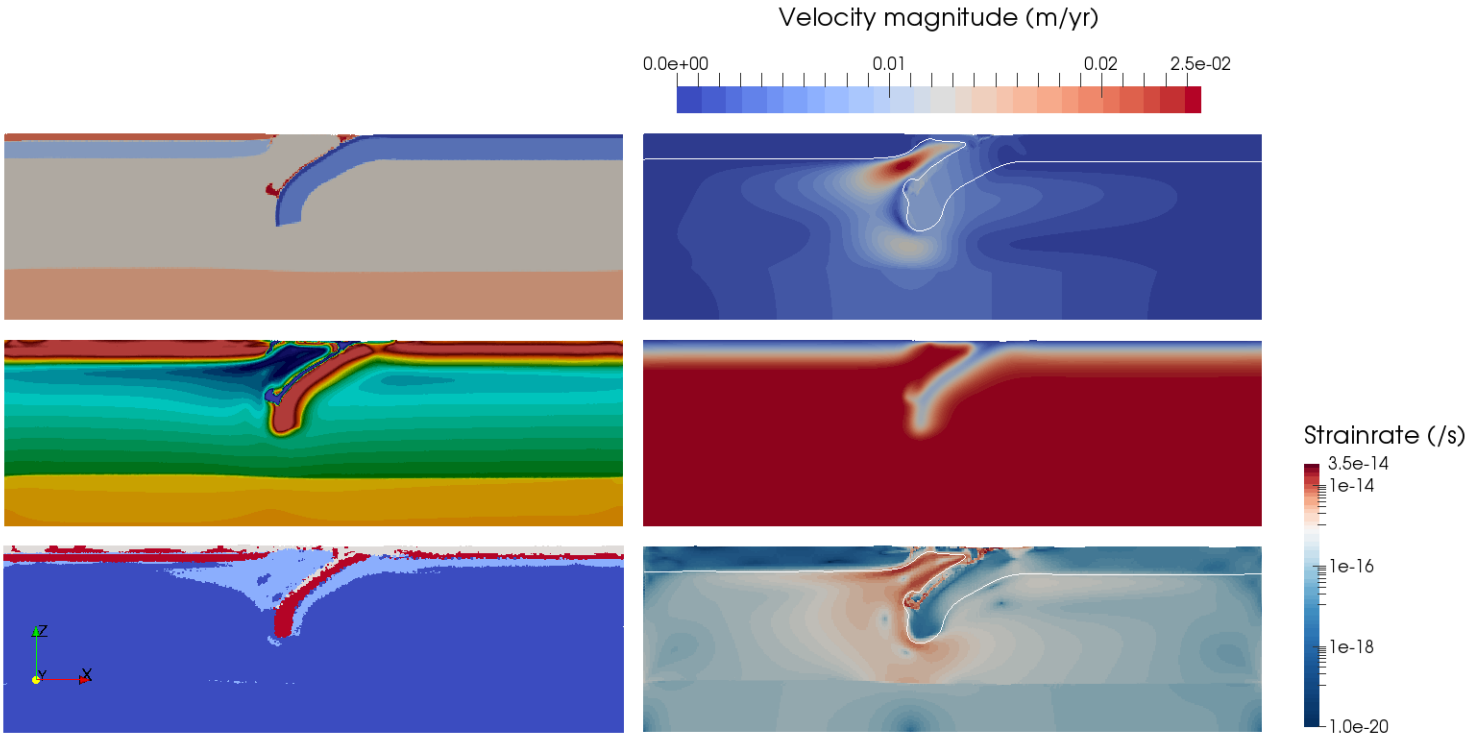

Figure 42: Result of run E_7apr after 15 Myr. Top left: material field, middle left: viscosity field, bottom left: dominant deformation mechanism, top right: velocity field, middle right: temperature field, bottom right: strain rate field. White line represents 1200°C isotherm.

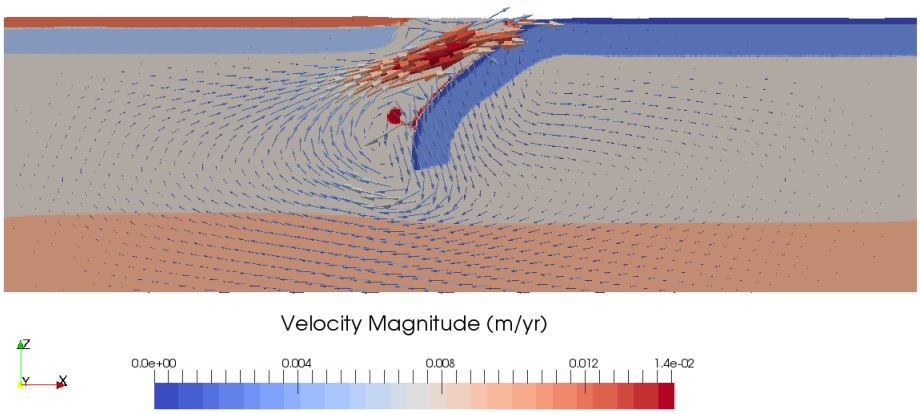

Figure 43: Result of run E_7apr after 22 Myr. Material field with velocity arrows.

4.2.7 Variations on *E_7apr*

In an attempt to create further rollback and to prevent a weak viscosity zone to form at the hinge, various major factors are varied and the result is compared to run *E_7apr* (Figure 44).

To prevent the weak zone to create unnatural shapes through time due to its extremely low viscosity, the viscosity of the weak zone is set at $10^{19} Pa.s$ for the first 100 km only. Thereafter the material of the weak zone follows the properties it has been given before.

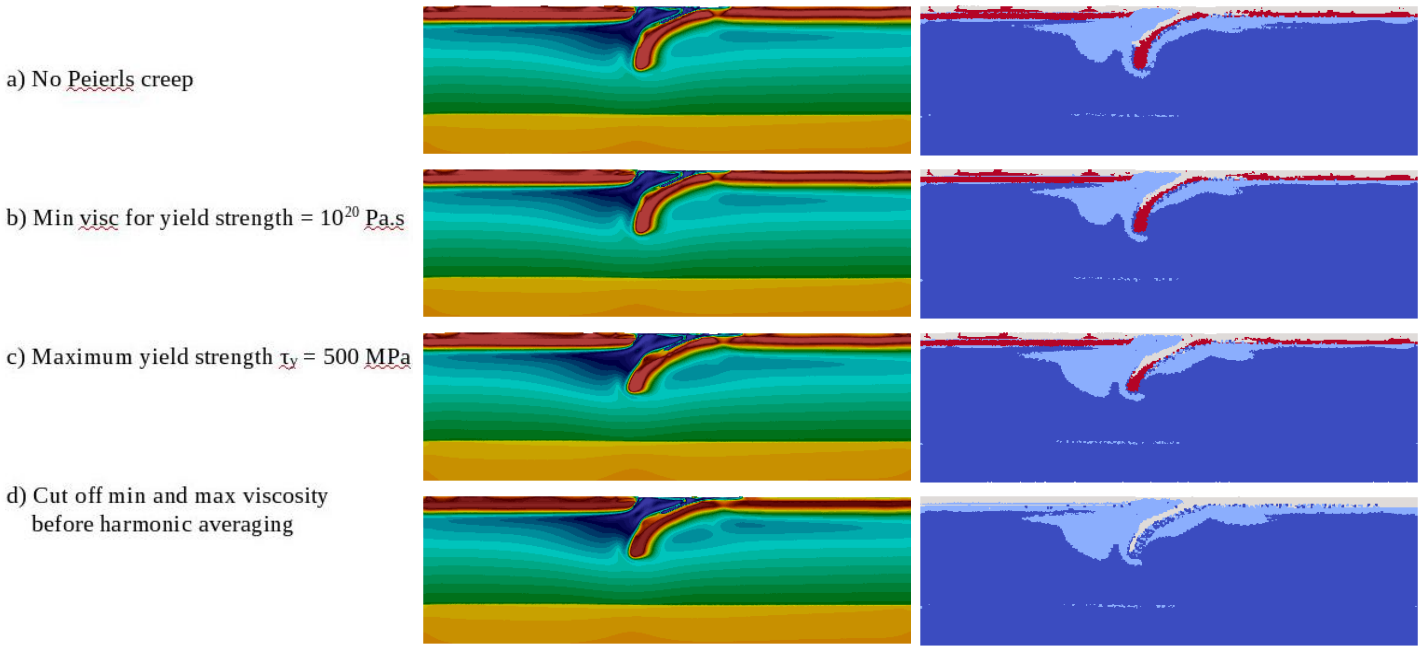

Figure 44: Result of a) run E_7apr after 5.4 Myr, b) run E_8apr after 5.5 Myr (minimal viscosity for yield strength = $10^{20} Pa.s$), c) run E_9apr 4.3 Myr (maximum yield strength $\tau_{ymax} = 500MPa$, d) run E_10apr 4.4 Myr (Cut off minimal and maximal viscosity before harmonic averaging).

The first variation, run E_8apr, is the implementation of a higher minimal viscosity of $10^{20} Pa.s$ for the viscosity obtained by yield strength (Figure 44b). This would cause the places where yield strength is the dominant deformation mechanism to have an increased viscosity. This **adaption** would thus increase the overall yield strength of the SP, including the hinge and the slab.

However, the result of this run is very similar to run E_7apr (Figure 44b) as the minimum viscosity created by the yield strength of the material is rarely reached.

The second variation, run E_9apr, is to decrease the maximum yield strength to $\tau_{ymax} = 500MPa$. Following equation 7, $\mu_y = \frac{min(\tau_y, \tau_{ymax})}{2\dot{\epsilon}_{II}}$, this will decrease the yielding viscosity μ_y. This would cause a more uniform lower yield strength of the material.

Figure 44c shows the result of run E_9apr. The viscosity of the slab is lowered and can thus more easily deform as it sinks. The hinge however still has lower viscosity than the surrounding lithosphere.

In the third variation, run E_10apr, a change in calculating the composite viscosity is applied. The composite viscosity is calculated by using the harmonic averaging of the viscosity values obtained by the various deformation mechanisms. Thereafter the viscosity is cut off at $10^{19} Pa.s$ as minimal viscosity and $10^{25} Pa.s$ as maximum viscosity. Another way to calculate the composite viscosity is to first cut of the viscosity values obtained by the various deformation mechanisms before harmonic averaging is applied.

This results in a lower viscosity overall (Figure 44d). The maximum viscosity is $3.3 \cdot 10^{24} Pa.s$ instead of $10^{25} Pa.s$. Apart from the lower maximum viscosity, however, the evolution of the domain is similar. Because the maximum viscosity is decreased the slab is weakened and breaks off at the hinge as the slab sinks.

Overall, these variations do not help to make a more stable slab without a weak point at the hinge and do not create further rollback.

4.2.8 Run E_11apr

Peierls creep is important for the flexibility of the slab as it sinks, but causes break-off at the hinge. For this reason run E_11apr only included Peierls creep from 100 km onwards. Figure 45 shows the result. For the full run see movie A.1.6.

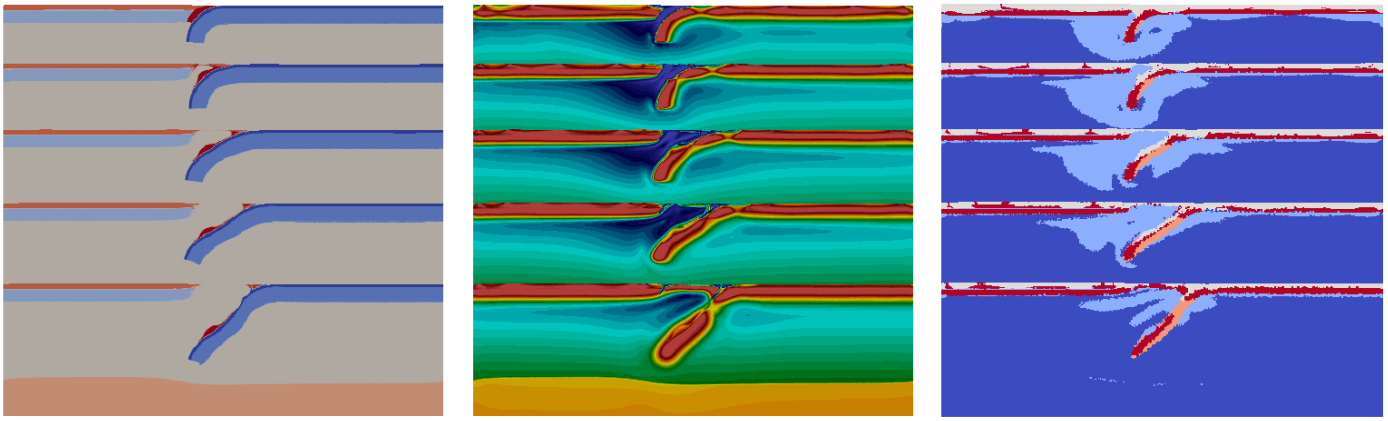

Figure 45: esult of run E_18apr. Left: material field, middle: viscosity field, right: dominant deformation mechanism. Top to bottom: 0 Myr, 1.6 Myr, 3.2 Myr, 6.8 Myr, 32.6 Myr

In the first 7 Myr the slab sinks 130 km while the slab rolls back 270 km. After 7 Myr only 30 km more rollback is observed while the strain localizes at 100 km depth, where Peierls is implemented. This causes the slab to break off here and sink (lowest image figure 45).

Implement velocity

So far the slab has not sunken further than around 500 km. As mentioned before, one reason for this is that the material right of the slab has no space to move to due to the absence of torroidal flow. When material is allowed to move through the side boundaries, this problem can be solved. This flow is constructed by implementing an absolute plate velocity (a similar velocity is imposed on both the SP and the OP so they both move with the same velocity relative to the mantle). Both on the left and on the right border a velocity of -2 cm/yr (towards the left) is implemented for the lithosphere. The velocity profiles on the left and right boundary of the domain are set equal so that an equal amount of material flows into the domain as out (see section 3.5). As the presence of Peierls creep at the hinge causes break-off, this absolute velocity will be implemented in a setup where Peierls creep is only present from 100 km onwards (run E_18apr) and where Peierls creep is absent (run E_19apr). Additionally, I will test the effect of a OP velocity of 2 cm/yr (run E_28apr).

4.2.9 Run E_18apr

Figure 46 shows the result of run E_18apr, which has similar properties as run E_11apr (Peierls creep from 100 km onwards) but with an imposed velocity of -2 cm/yr.

In 15 Myr the slab sinks all the way to the lower mantle. As the slab sinks it gets pushed further down by the imposed absolute velocity. As material is moving in and out of the domain, the mantle material can be displaced and the slab can continue to sink (Figure 47). As the overriding plate moves out of the domain, mantle material is free to flow into the back-arc basin, expanding over time.

In absolute plate motion frame the slab rolls back 190 km in the first 4 Myr and then moves back 340 km in the following 25 Myr (Figure 46). In a relative plate motion frame a back-arc basin of 500 km is created over 30 Myr. The growing of the back-arc basin is however caused by the overriding plate moving away from the trench instead of the plate further detaching from the surface.

The point where the slab refuses to detach from the surface and roll back further is thus still present. More material flowing into the back-arc basin does not prevent the viscosity to increase at the surface of the back-arc basin and after 10 Myr the whole surface of the back-arc basin has maximum viscosity.

As the slab reaches the lower mantle, the rheology increases and the tip of the slab stops to sink further. The absolute velocity continues, and more lithospheric material sinks down. This causes the slab to fold upon the lower mantle. The folding is made possible by Peierls creep. As Peierls creep is only present from 100 km onwards and the slab does not break off at the surface (Figure 46).

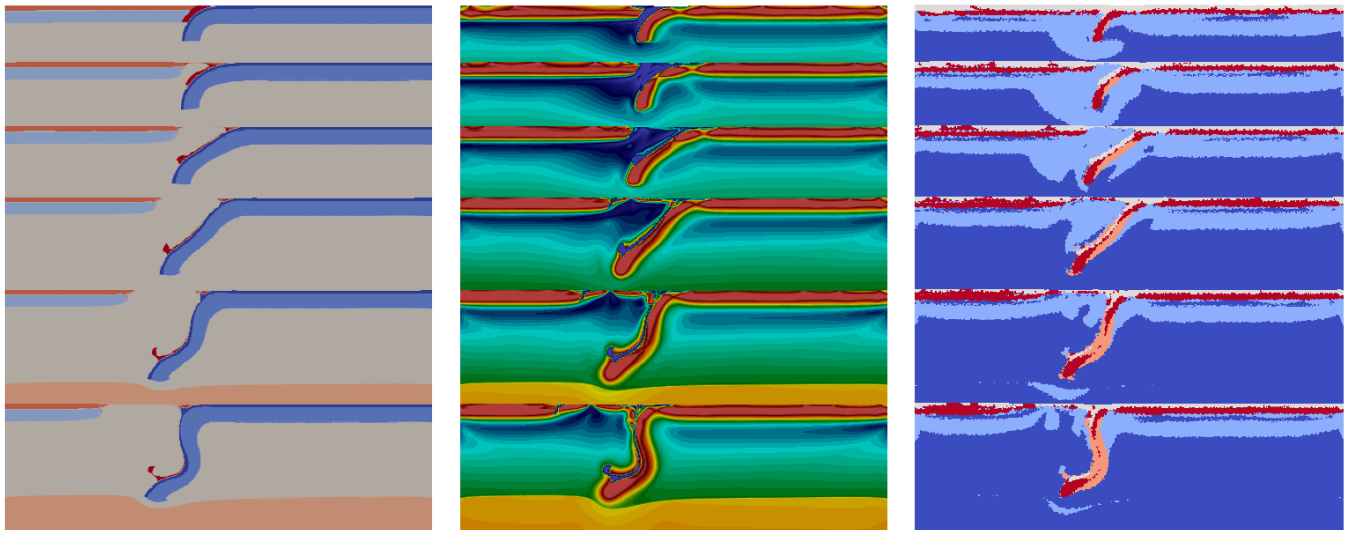

Figure 46: Result of run E_18apr. Left: material field, middle: viscosity field, right: dominant deformation mechanism. Top to bottom: 0 Myr, 1.8 Myr, 4.1 Myr, 11.6 Myr, 21.4 Myr, 30.6 Myr.

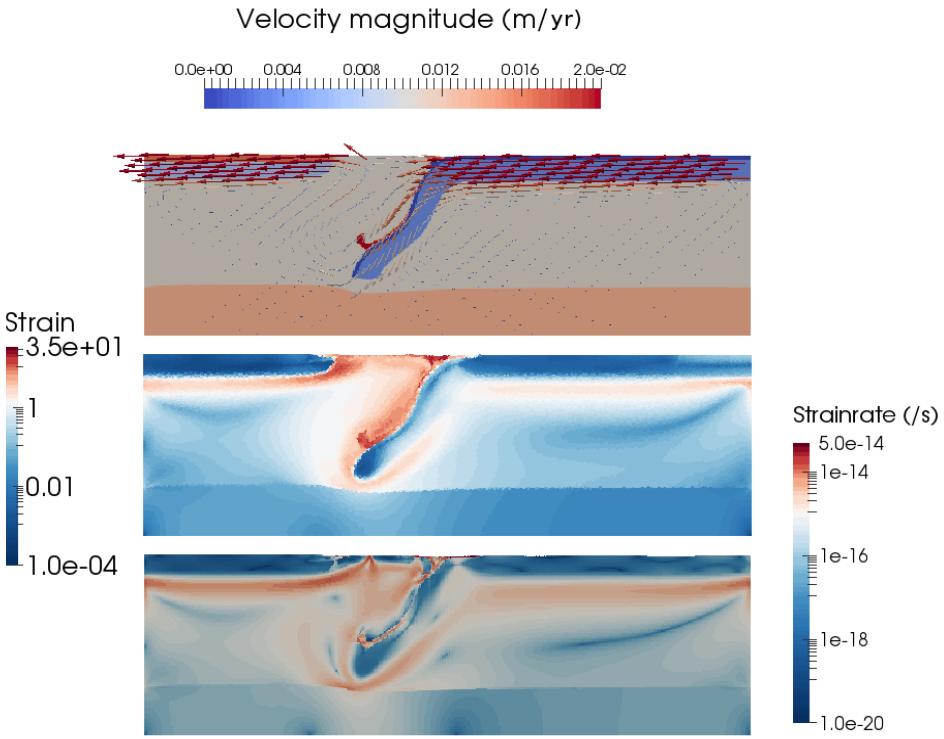

Figure 47: Result of run E_18apr after 17.5 Myr. Top: material field with velocity arrows, middle: strain field, bottom: strain rate field (s^{-1}).

4.2.10 Run *E_19apr*

For run E_19apr Peierls creep is absent. Again an absolute velocity of -2 cm/yr is implemented. Figure 48 gives the result. For the full run see movie A.1.7.

In 15 Myrs the slab sinks all the way to the lower mantle. In this time the trench has moved back 200 km while the OP has moved away 300 km. A back-arc basin of 500 km has thus formed. After 15 Myrs the absolute plate motion causes the trench to move towards the left and as it does it overturns the slab to a more vertical position as it approaches the lower mantle. In the next 25 Myr the absolute velocity pushes the slab slightly into the lower mantle. Due to the high

viscosity of the lower mantle the sinking velocity decreases and not all imposed velocity of the SP is transferred to slab sinking. Instead a part of the imposed velocity is transferred horizontally to the back-arc basin moving over the slab (see Figure 49). This causes the viscosity in the slab and at the surface to increase significantly (Figure 48).

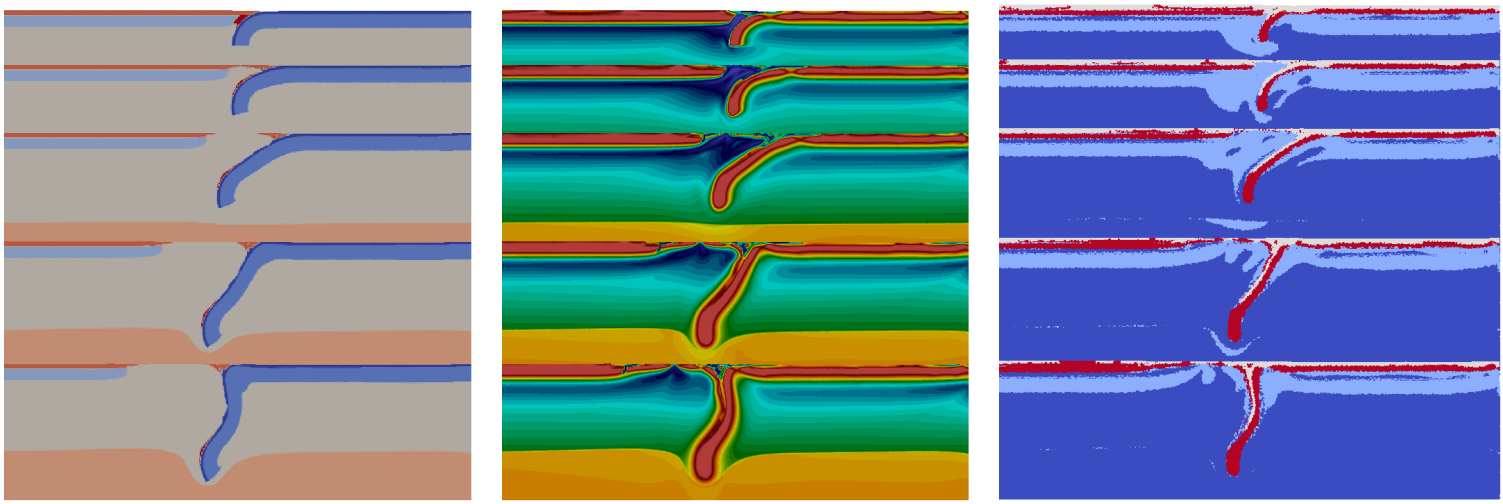

Figure 48: Results of run E_19apr. Left: material field, middle: viscosity field, right: dominant deformation mechanism. Top to bottom: 0 Myr, 3.7 Myr, 11.9 Myr, 28.2 Myr, 41.0 Myr

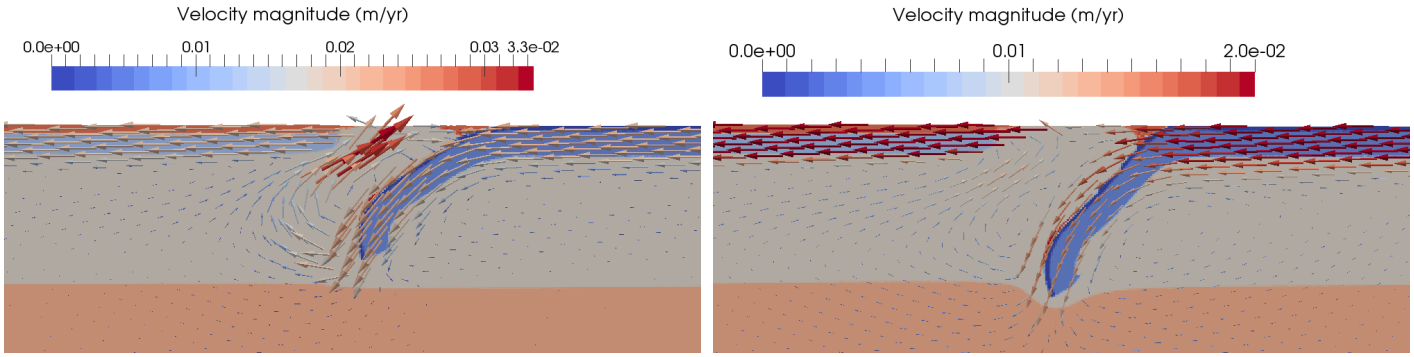

(a) 11.9 Myr *(b) 22.2 Myr*

Figure 49: Material field with velocity arrows at a) 11.9 Myr and b) 22.2 Myr.

4.2.11 Run *E_28apr*

With the setup similar to run *E_18apr*, a velocity of 2 cm/yr is imposed on the overriding plate in run *E_28apr*. Figure 50 gives the result.

First, rollback is created by the creation of the back-arc basin. Thereafter the overriding plate approaches the slab, pushing the trench further back. However, the plate does not sink further than 500 km, as the mantle material right of the slab needs to move underneath the slab towards the right side of the domain for motion to continue (Figure 51).

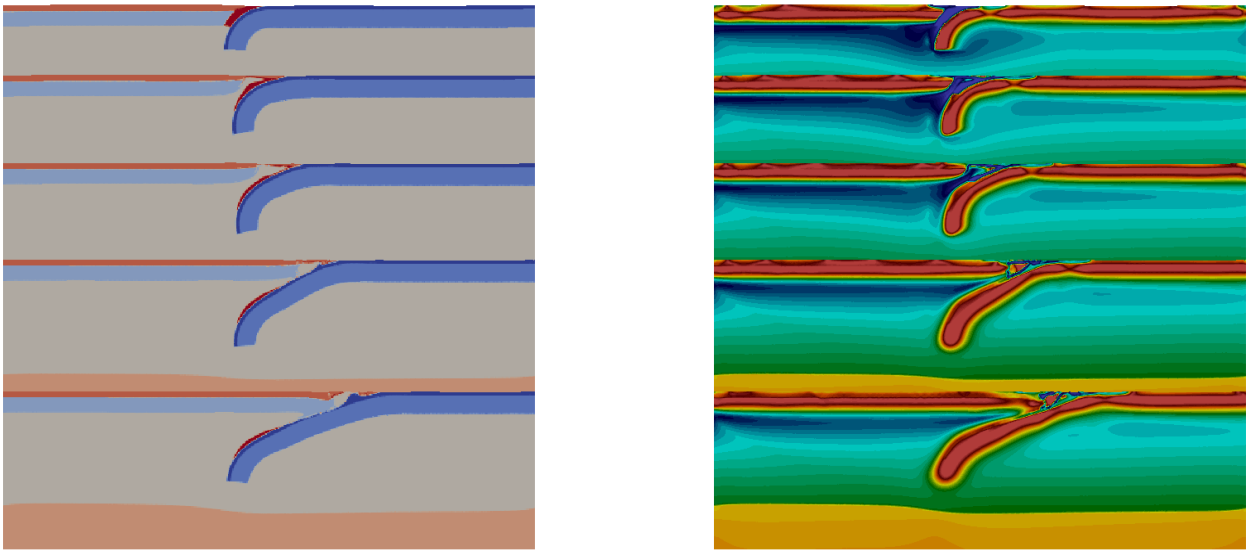

Figure 50: Result of run E_28apr over time. Left: material field, right: viscosity field.

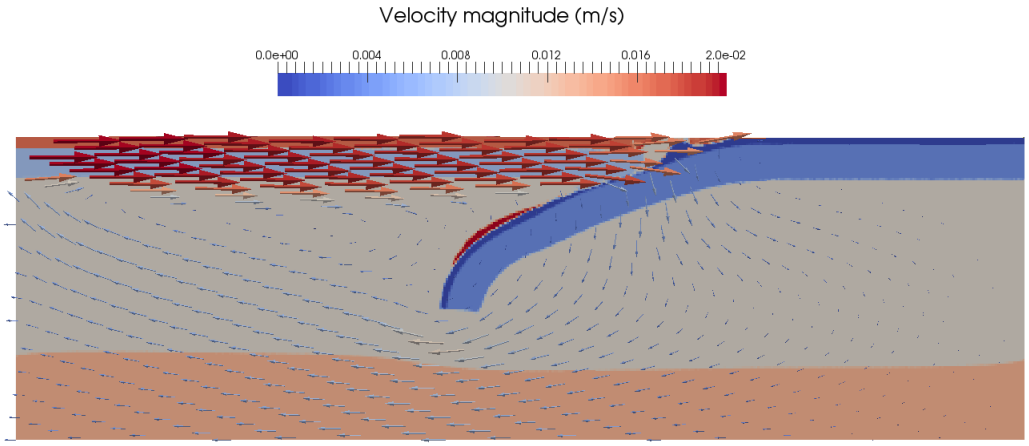

Figure 51: Result of run E_28apr. Material field with velocity arrows.

Lengthened oceanic lithopshere

With an imposed velocity the material can move through the domain and the slab can sink towards the lower mantle. Looking back at section 1, the slab is able to sink through the upper mantle as the mantle material below the SP can move up to the surface where the ridge forms (see e.g., run E_26jan, section 4.1.6). No extreme sinking velocities are reached (section 4.2.1) as the domain is wide and the age gradient shallow. With a smaller domain, however, a ridge causes unnatural acceleration (run E_13mrch and E_20mrch) and a constant age of the oceanic lithosphere is required.

For this reason the domain is widened to $L_x = 5500km$ and our SP is lengthened to $4000km$ (similar to section 1). The age at the right boundary is set at 40 Myr and at the trench at 80 Myr. In this way the slab can sink due to slab pull and ridge push due to the creation of the ridge without unnatural accelerations. I experiment again with the effect of Peierls creep by implementing Peierls creep from 100 km onwards (run E_21apr), leaving Peierls creep out (run E_26apr) and implementing Peierls creep throughout (run E_27apr). Last, a slight temperature gradient is added through the domain, to experiment how this will effect the subduction (run E_3may).

4.2.12 Run *E_21apr*

In run *E_21apr* Peierls creep is present from 100 km onwards. Figure 52 gives the result of run *E_21apr*. For the full run see movie A.1.8.

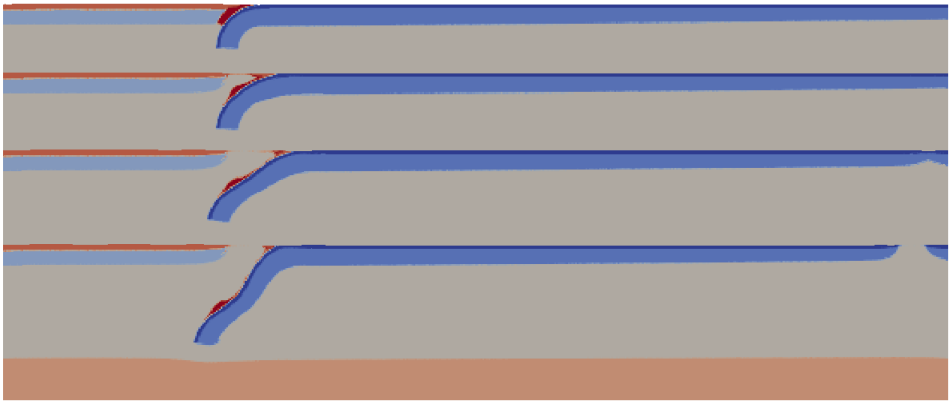

Figure 52: Result of run E_21apr: material field. Top to bottom: 0 Myr, 2.2 Myr, 5.0 Myr, 12.1 Myr.

In the first 5 Myr a back-arc basin forms and the slab sinks 140 km into the upper mantle until a depth of 400 km. In this time the SP has rolled back 220 km. At 5 Myr a ridge forms at the right boundary and a convection cell is formed of mantle material moving up to the ridge, the oceanic lithosphere moving to the left and the slab sinking down (Figure 53). After 5 Myr rollback ceases and the trench starts to move back to the left slowly as the slab continues to sink. After 12 Myr the slab has sunken another 80 km and the trench has moved 90 km back to the left.

A small convection cell is formed right of the slab where mantle material moves in a backward flow into the wedge. As slab continues to sink the trench starts moving towards the left the back-arc basin decreases. The backward flow decreases and becomes concentrated below the overriding plate (Figure 53). This returnflow causes the slab to bend at depth due to Peierls creep.

As seen in figure 53, a high velocity arrow is observed at the trench of 3.1 cm/yr. This causes the surface to become unstable after 12 Myr and starts to oscillate.

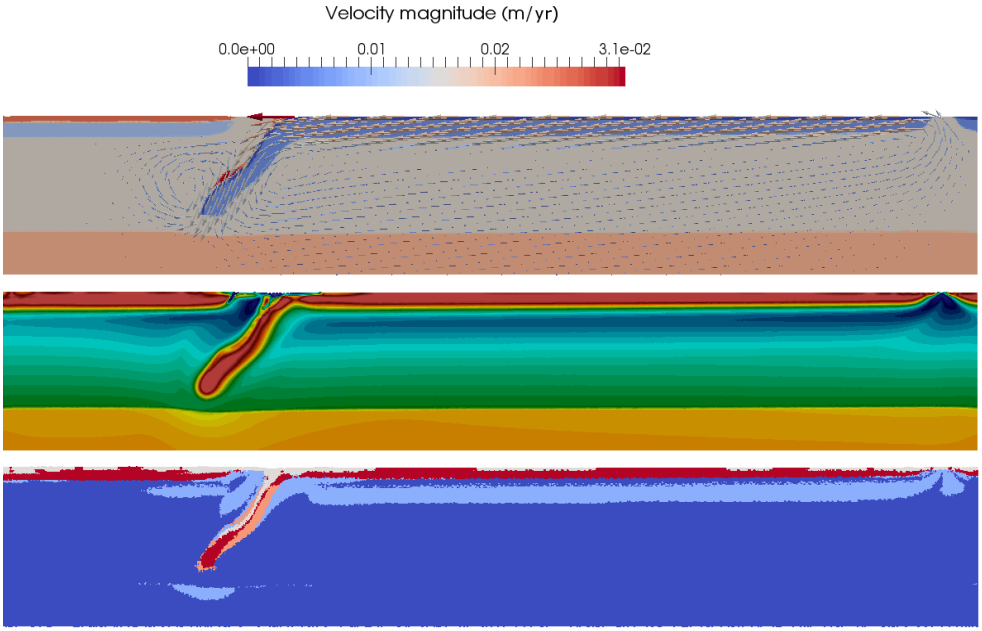

Figure 53: Result of run E_21apr after 12.1 Myr. Top: material field with velocity arrow, middle: viscosity field, bottom: dominant mechanism (Peierls present from 100 km onwards).

4.2.13 Run *E_26apr*

In run *E_26apr* Peierls creep is left out. Also, the weak zone is thinned to 20 km width. Result is shown in figure 54.

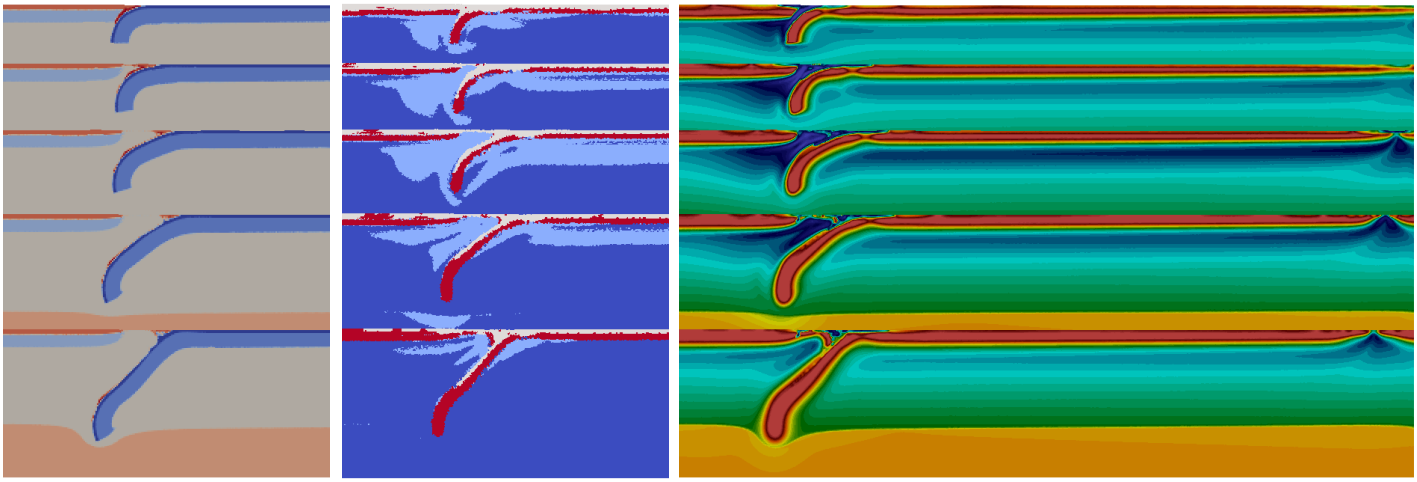

Figure 54: Result of run E_26apr. Left: material field, middle: deformation mechanism, right: viscosity field. Top to bottom: 0 Myr, 3.0 Myr, 5.6 Myr, 10.8 Myr, 35.6 Myr

Firstly, the 20 km thick weak zone seems to be enough for a mantle back-arc basin to form in this setup (Figure 54).

The slab sink into the upper mantle and tilts as it approaches the lower mantle. Because of the absence of Peierls creep the slab does not deform easily and the viscosity in the slab is increasingly high, comparable to run *E_7apr*. Because of the age gradient the slab can continue to sink, instead of diffusing into the upper mantle, but decreases in velocity through time.

As in run *E8_18apr*, the back-arc basin forms in the first 5 Myr, where after a ridge forms and the slab continues to sink and the trench slowly moves back towards the left. After 10 Myr the slab has reached the lower mantle and the slab slows down. After 35 Myr the motion has slowed down and the tip of the slab has slightly penetrated into the lower mantle. Also the viscosity of the slab has increased significantly and the motion has decreased to a few mm/yr. Except at the surface of the back-arc basin, where horizontal velocities still reach 1 cm/yr. This causes the surface to start oscillating after 35 Myr.

4.2.14 Run *E_27apr*

In run *E_27apr* Peierls creep is present throughout the whole domain. The result is shown in figure 50. For the full run see movie A.1.9.

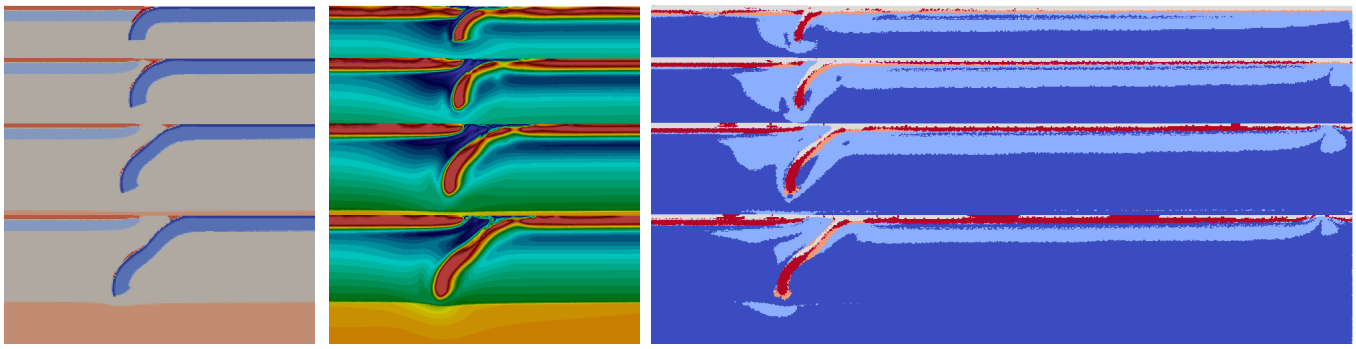

Figure 55: Result of run E_27apr. Left: material field, middle: viscosity field, right: deformation mechanism. Top to bottom: 0 Myr, 3.5 Myr, 6.7 Myr, 10.9 Myr

A back-arc basin forms in the first 5 Myr, where after a ridge forms and the slab continues to sink. After 10 Myr the slab has reached the lower mantle. As Peierls creep is present the slab bends as it sinks. Although Peierls creep is present through the whole domain, the slab does not break off at the hinge. This is due to the lengthened subducting plate, decreasing the strain in the hinge due to a shallower density gradient through the subducting plate.

When the tip of the slab approaches the lower mantle after 10 Myr, rollback ceases. Figure 56 shows the velocity at 6.7 Myr, when rollback is still continuing, and 9.4 Myr, when rollback has ceased. At 6.7 Myr the mantle material moves into the back-arc basin with a maximum of 8.3 cm/yr and the trench is pushed back with 3 cm/yr at the surface of the back-arc basin. At 9.4 Myr the backward flow has decreased to maximal 3.7 cm/yr and the velocity at the surface has decreased to 1 cm/yr. In the trench little movement is observed anymore and rollback has ceased.

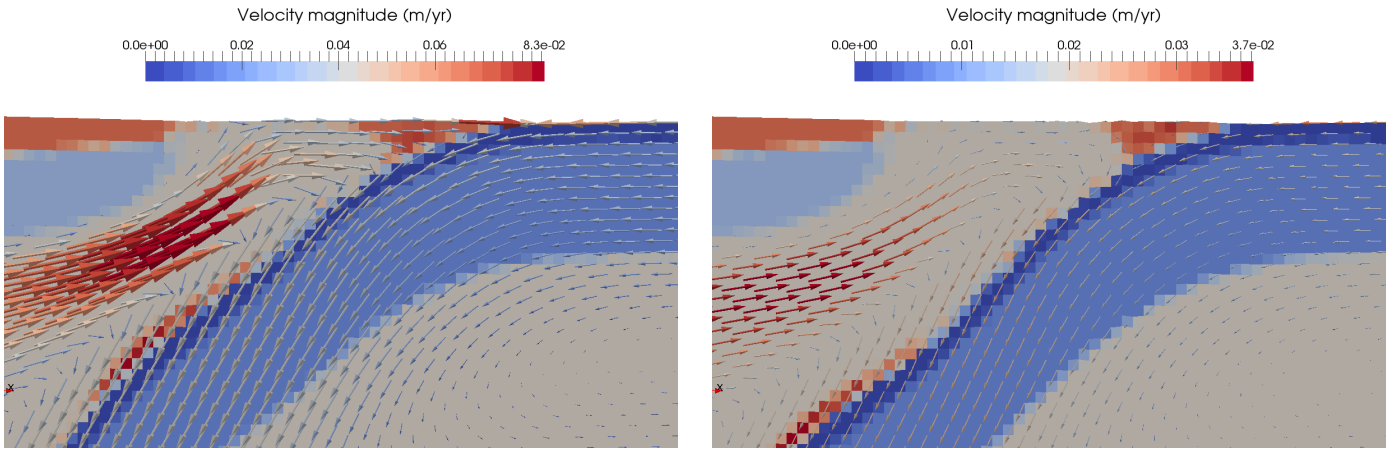

(a) 6.7 Myr *(b) 9.4 Myr*

Figure 56: Material field with velocity arrows of run E_27apr after a) 6.7 Myr and b) 9.4 Myr.

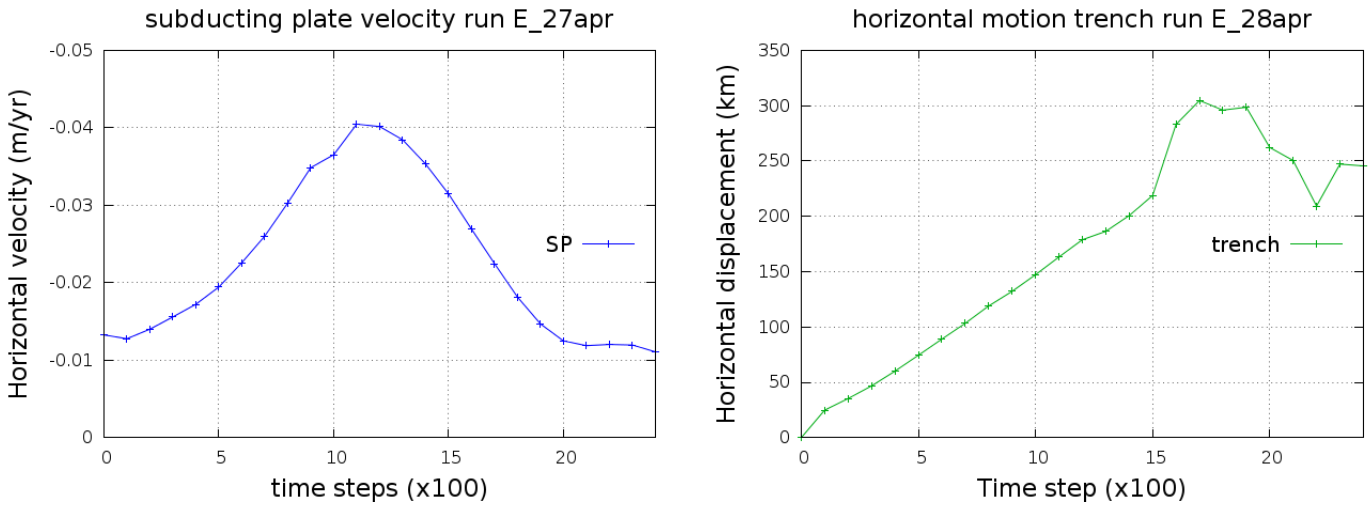

Figure 57: left: horizontal velocity of the SP (m/yr) vs time steps, right: horizontal displacement of the trench (km) of run E_27apr

After 11 Myr oscillations form at the trench and the code becomes unstable. Figure 58 shows the velocity arrows at the trench just before the oscillations start. In the back-arc basin material moves with 1.5 cm/yr towards the right and bends down with the slab back into the mantle. In the SP material moves with a similar velocity in the opposite direction, bending down with the slab. In between there is a small area of continental crust material which is squeezed between these two materials. Around 11 Myr this causes the surface in the back-arc basin to go oscillating.

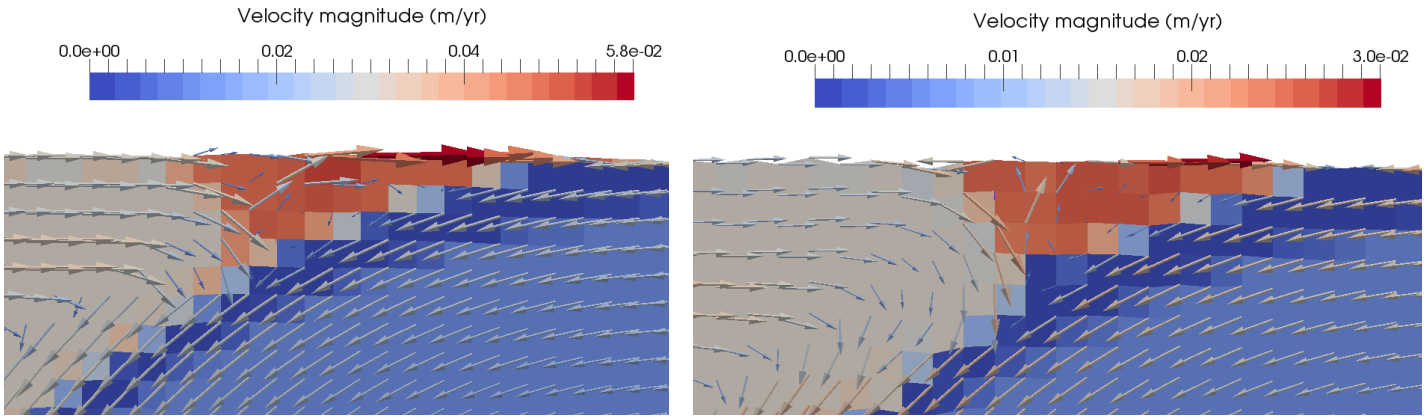

(a) 8.3 Myr *(b) 10.9 Myr*

Figure 58: Material field with velocity arrows of run E_27apr at various times.

4.2.15 Run *E_3may*

To experiment what the effect is of a temperature gradient through the mantle, a temperature gradient of 0.2 °/km is added through the mantle. This gives creates a temperature of 1450 °C at the bottom of the domain and 1380 °C at the ULM boundary. Figure 59 shows the initial temperature field.

Figure 59 gives the result of run *E_3may*.

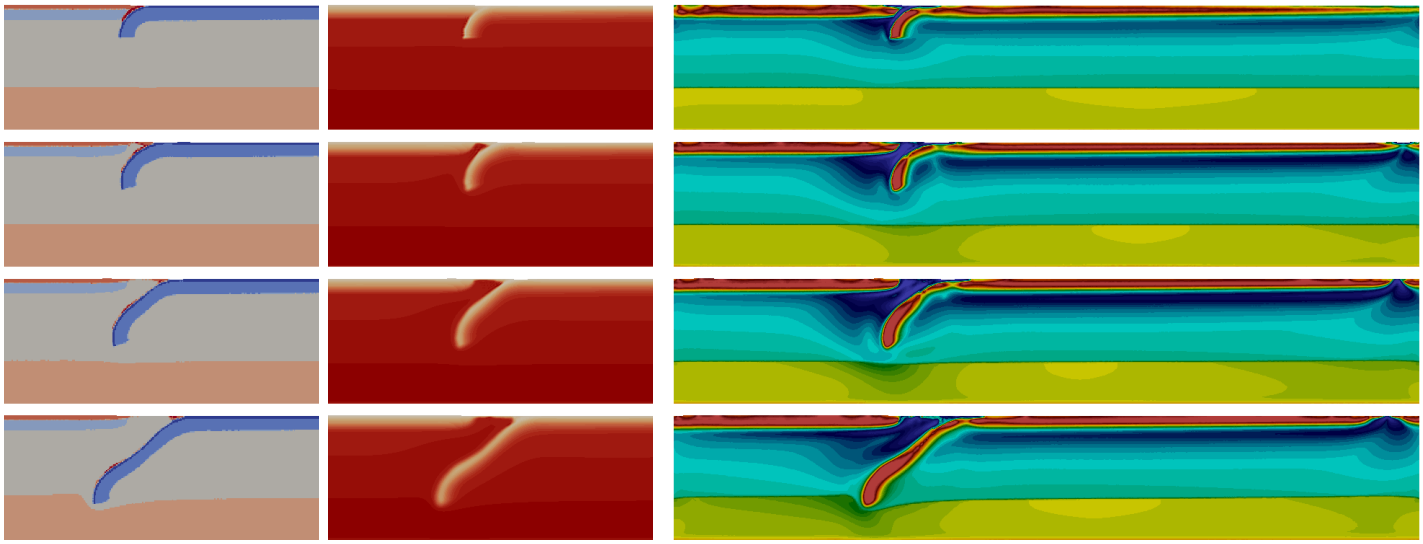

Figure 59: Result of run E_3may. Left: material field, middle: temperature field, right: viscosity field. Top to bottom: 0.2 Myr, 2.3 Myr, 3.8 Myr, 7.2 Myr

Overriding plate

So far I have tried to create further rollback by imposing a weak zone and inserting an age gradient. Going back to section 1, the age gradient in the overriding plate made it possible for the overriding plate to be free to move away from the side boundary with the trench. This made it easier for the trench to move and thus to create rollback and further sinking. In section 2 the overriding plate is continental and thus no ridge can form and the OP remains attached to the side boundary and cannot effect the trench motion and subduction evolution. In run *E_30apr* the OP is detached from the side boundary, to investigate the effect is of a freely moving OP. In run *E_1may* a wider weak zone is implemented to see the effect of a back-arc basin. Last, the OP is removed altogether, to see how this effects the subduction system (run *E_2may*).

4.2.16 Run *E_30apr*

In run *E_30apr* the overriding plate is detached from the left boundary, so it is free to move from the boundary. This is done by placing low viscosity upper mantle material left of the overriding plate (top Figure 60). The width of the domain is set at $Lx = 6000km$ and the trench is set at $X_{trench} = 3000km$. In this way both the OP and SP are 3000 km long. The age gradient of the SP is set at 40-80 Myr. The parameters are similar to run *E_27apr* (including Peierls creep).

Figure 60 gives the result over 50 Myr. For the full run see movie A.1.10.

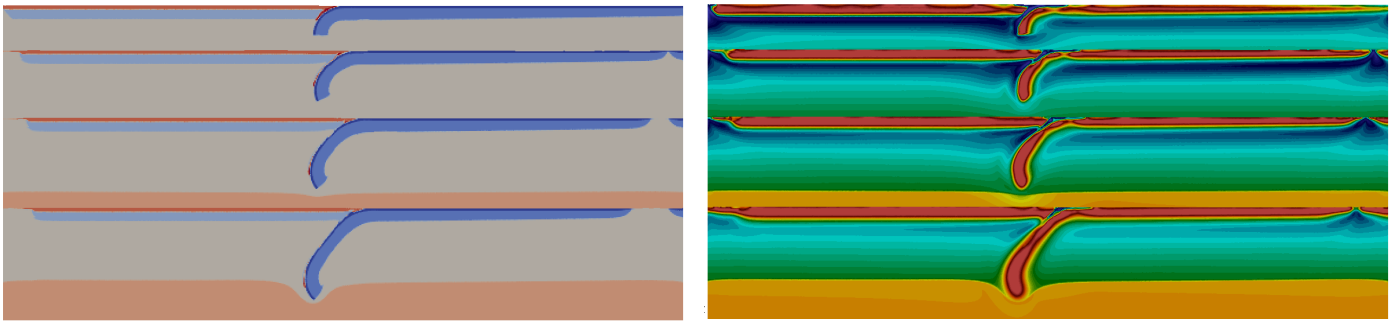

Figure 60: Result of run E_30apr at (top to bottom): 0 Myr, 4.5 Myr, 11 Myr, 50 Myr. Left: material field, right: viscosity field.

As the OP is free to move, it moves to the right, squeezing the weak zone between the plates so no mantle material can penetrate. As the ridge forms the slab continues to sink until it reaches the lower mantle around 8 Myr. Over this time the trench has moved 130 km back towards the left. After 8 Myr the sinking velocity decreases as it slowly penetrates the lower mantle with a few mm/yr. After 50 Myr another 95 km of rollback is observed and the slab has sunken 160 km into the LM. The viscosity of the slab has increased significantly in this time.

Now that the overriding plate is free to move, motion is possible on both sides of the slab. Figure 61 gives the velocity field after 6.1 Myr. The SP moves with a horizontal velocity of -3 cm/yr and the OP with a horizontal velocity of 1 cm/yr. The material right of the slab moves towards the ridge while the material left of the slab either forms a backward flow into the back-arc basin above the slab or moves towards the left boundary where mantle material can move up.

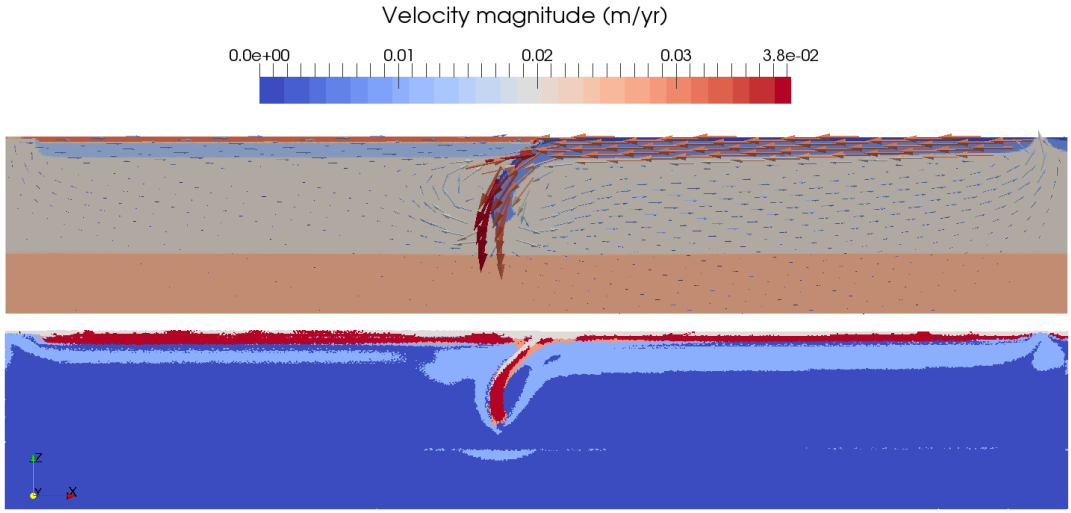

Figure 61: Result of run E_30apr after 6.1 Myr. Top: material field with velocity arrows, bottom: viscosity field.

4.2.17 Run *E_1may*

At run *E_30apr* no back-arc basin formed as the OP moved towards the slab so the back-arc basin had no time to form. For run *E_1may* a wider weak zone of 40 km wide is implemented to make it possible for a back-arc basin to form. Figure 63 shows the result over 30 Myr. For the complete run see movie A.1.11.

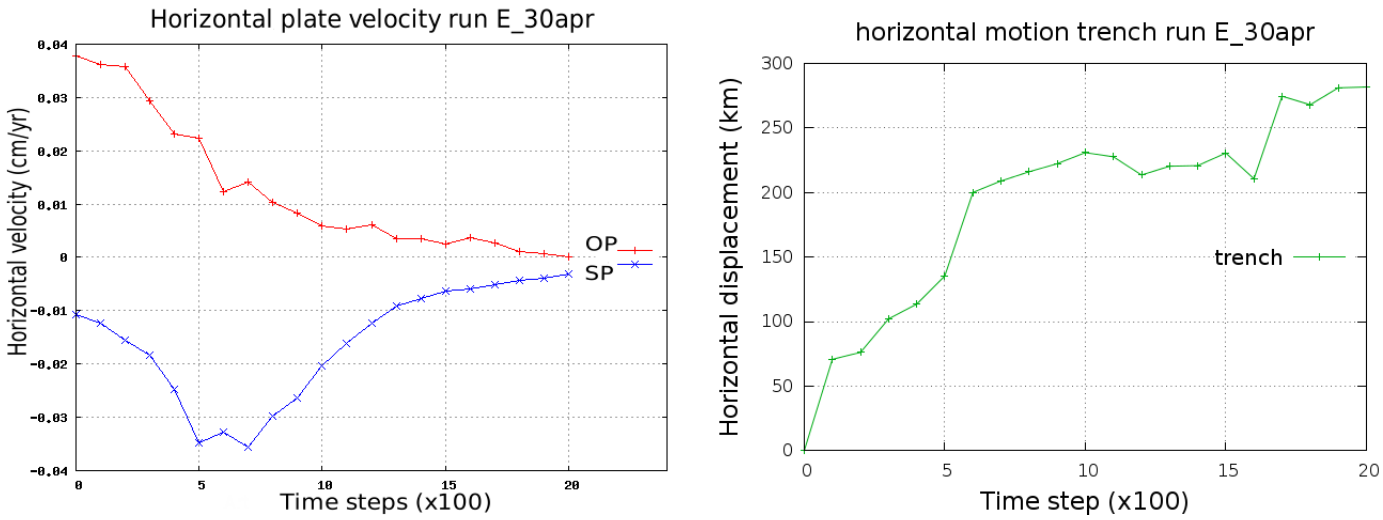

Figure 62: left: horizontal velocity of the SP (m/yr) vs time steps, right: horizontal displacement of the trench (km) of run E_30apr

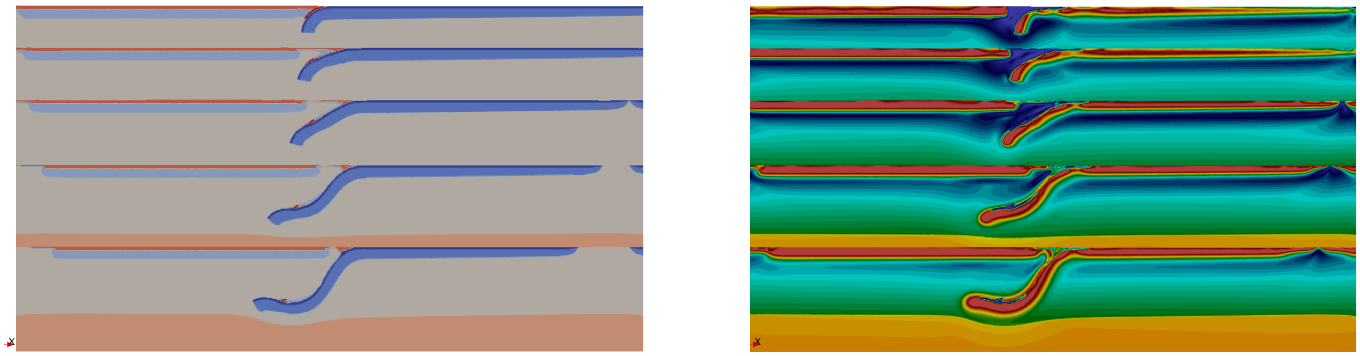

Figure 63: Result of run E_1may (top to bottom): 0 Myr, 1.0 Myr, 3.6 Myr, 11.3 Myr, 30.2 Myr. Left: material field, right: viscosity field.

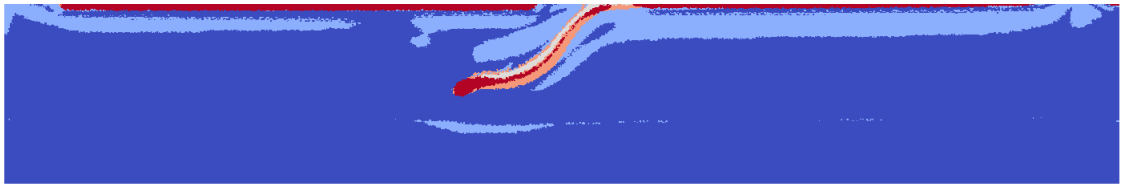

Figure 64: Mechanisms at 11 Myr.

Because the weak zone is bigger, the material has space to penetrate into the wedge. In the first 4 Myrs a back-arc basin of 430 km has been created caused by 260 km of rollback and 170 km by penetrating mantle material into the OP. Meanwhile the OP moves towards the right with a velocity of 2.3 cm/yr. As the velocity of the backward flow decreases over time the OP motion decreases the size of the back-arc basin, approaching the trench. After 4 Myr the trench remains roughly at the same position.

As the overriding plate approaches trench the slab continues to sink, the slab moves to a horizontal position just above the lower mantle. As it lies down on the lower mantle the viscosity of the slab increases and the velocity decreases to roughly 1 cm/yr.

At 30 Myr 1200 km of slab has subducted and the ridge had widened 480 km. Also the continental lithosphere has moved 340 km away from the left boundary. In this time the continental lithosphere has not completely reached the trench, leaving 70 km of mantle material in between. After 30 Myrs, however, the surface starts to oscillate at the trench. Figure 65 gives the magnitude of the velocity at the trench where the surface start to become unstable.

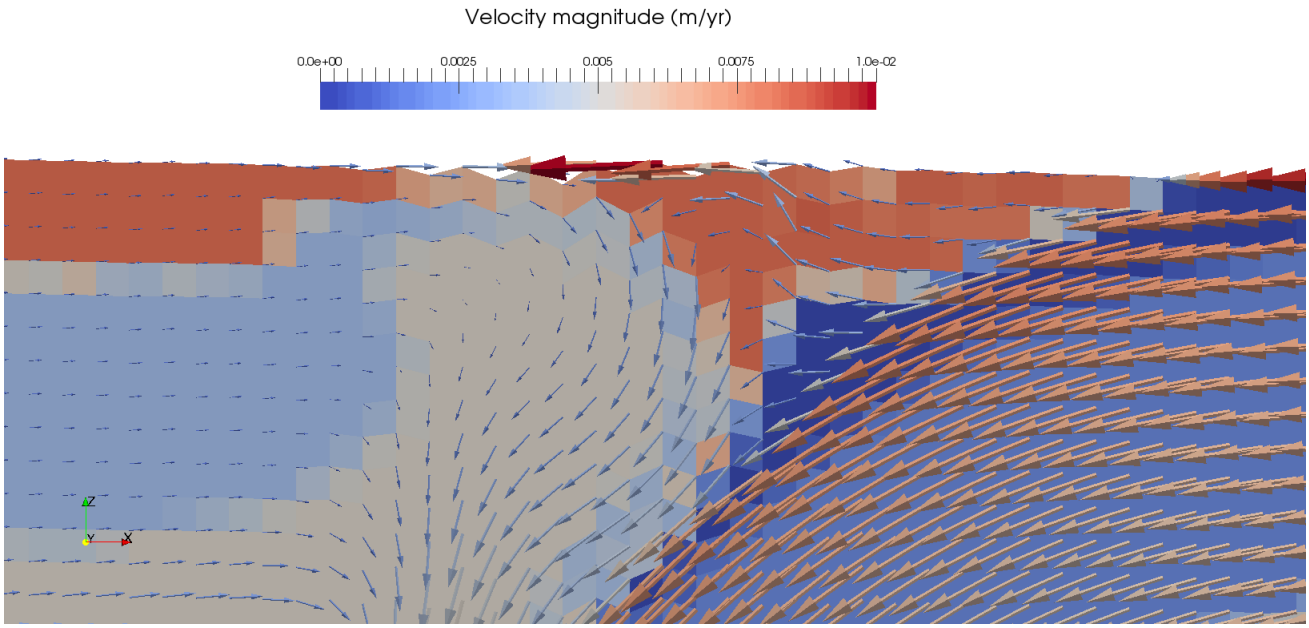

Figure 65: Material field with velocity arrows after 30 Myr at trench of run E_1may.

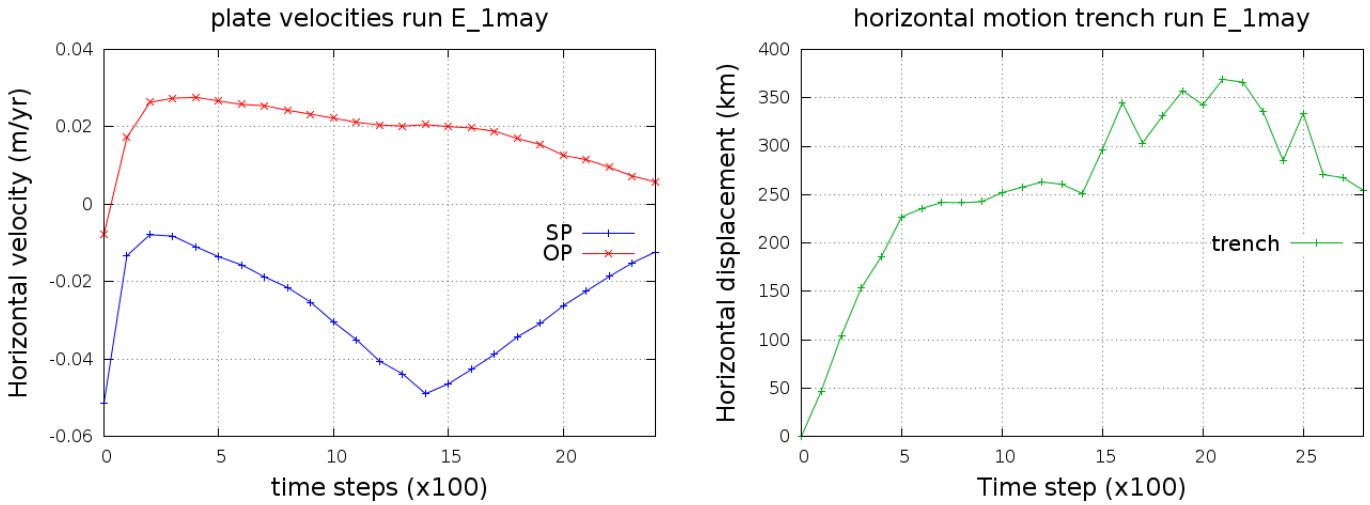

Figure 66: left: horizontal velocity of the SP (m/yr) vs time steps, right: horizontal displacement of the trench (km) of run E_1may

4.2.18 Run *E_2may*

To test the influence of the free surface and the OP, run *E_2may* is ran with a free slip boundary condition at the top boundary and without the presence of an OP. Figure 67 shows the result.

Even without an overriding plate, the slab only detaches for the first 50 km. After this the crustal material piles up at the trench and the trench migrates leftwards as the ridge forms at the right boundary. It thus seems that this trench locking is not due to the effect of the overriding plate but due to the behaviour of the (oceanic crust of the) SP and the the solution should be searched at the contact between the mantle material and the SP at the trench.

In this run the slab sinks increasingly vertically into the mantle, contrary to run *E_1may*, where the slab tilts to a horizontal position. The presence of an OP thus strongly effect the evolution and shape of the slab in the UM.

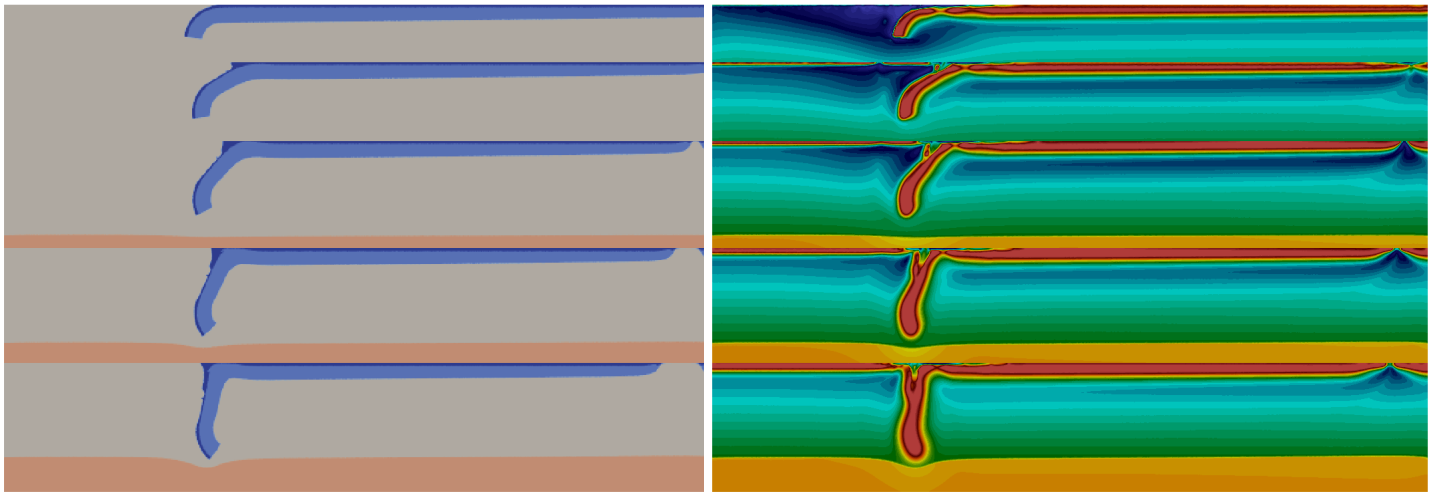

Figure 67: Result of run E_2may. Left: material field, right: viscosity field. Top to bottom: 0.1 Myr, 4.4 Myr, 9.6 Myr, 18.2 Myr, 34.9 Myr

5 Discussion

5.1 Lower mantle

A significant problem in the code is the behaviour of the lower mantle as the slab approaches the ULM boundary. As an initial condition, the lower mantle is set as a separate material, with separate material properties. The lower mantle set to be present below 660 km depth. The lower mantle is highly viscous (10^{22} to 10^{23} Pa.s) and is deformed primarily by diffusion creep, which is prescribed in the material properties of the viscosity for the material.

In run E_26jan the LM has a viscosity of $3 - 4 \cdot 10^{22} Pa.s$ and a viscosity jump of 1 order of magnitude at the ULM boundary. When the slab starts sinking through the upper mantle, the ULM boundary almost directly starts deforming as it approaches. When the tip of the slab has sunken to 550 km, the boundary has lowered locally over 40 km beneath the slab and increased 15 km in height towards the sides. The distance between the tip of the slab and the top of the lower mantle is thus increased from 110 to 150 km. Although the viscosity of the LM is 10x as high as the viscosity at the bottom of the UM and only deforms through diffusion creep, the UM material which is displaced by the subducting slab has enough strength to deform the ULM boundary.

Varying the viscosity of the LM from $10^{22} Pa.s$ to $10^{23} Pa.s$ changes how easily the ULM can deform, but still does not allow penetration through the ULM boundary. With a low viscosity LM the boundary deforms more easily (Figure 21) while with a higher viscosity LM, and thus increased viscosity jump (run E_10feb, Figure 28), the boundary is stiffer so harder to deform. Either way the slab does not penetrate through and the boundary remains deformed.

In an attempt for the slab to break through the ULM boundary, dislocation creep is added as a deformation mechanism to the LM (run E_10feb). This causes the viscosity to decrease locally where the slab approaches the LM (Figure 28). Due to this local decrease the viscosity of the LM becomes less stratified and thus start varying locally. The decrease in viscosity makes it easier for the slab to deform the ULM boundary on a more local scale, but does not solve the problem.

Also the depth of the domain has no influence on the behaviour of the LM. In section 1 the domain is 1400 km deep, including 740 km of LM, while in section 2 the domain is only 900 km, including only 240 km of lower mantle material. Both setups however show a similar LM behaviour. The width of the domain would effect the ULM boundary as there would be more area to compensate for the displaced material where the slab indents the boundary.

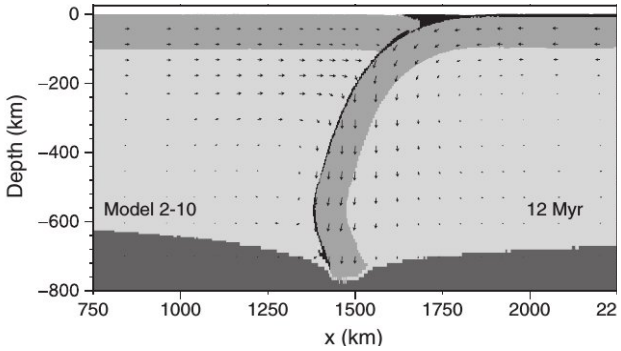

Figure 68: The resulf of a numerical ocean-ocean subduction model including a linear viscous lower mantle by Quinquis et al. (2011).

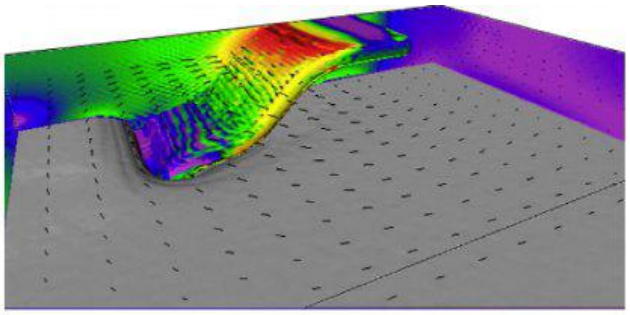

Figure 69: The result of a numerical one-sided subduction model by Stegman et al. (2010).

An impermeable boundary is thus created between the UM and LM where the slab only indents the boundary when it approaches but never sinks through. This problem is also seen in Quinquis et al. (2011), where the mantle is linearly viscous and a viscosity jump of 2 orders of magnitude ($10^{20} Pa.s$ in the UM to $10^{22} Pa.s$ in the LM) is present (Figure 68). Similar to our model they use a square grid with low resolution. The slab has a constant high viscosity of $10^{23} Pa.s$, an order of magnitude higher than the LM and no strain weakening process is implemented. Either the low resolution or the high viscosity of the slab might thus be an explanation to the observed problem. Quinquis et al., 2011, however, does not give a possible explanation for this phenomenon.

Stegman et al. (2010) also created an impermeable ULM boundary and as the slab sinks the boundary gets locally deformed (Figure 69). In the subduction models of Stegman et al. (2010) the slab either lies flat or is folded on the ULM boundary. The viscosity of the slab is decreased by the presence of a low yield strength making folding possible. However, although the ULM boundary is similar to Quinquis et al. (2011), this lowered viscosity does not cause a penetration of the slab into the lower mantle but merely causes the slab to fold on top of the ULM boundary, similar to our results. This indention of the ULM mantle, however, does not cause a problem in the setup of Stegman et al. (2010) as they use a wide

3D domain that compensates for this indention. Additionally, They are not focused on stimulating a slab that penetrates through the ULM boundary and this observation is not further discussed.

Other numerical models with a similar setup, however, do not show this deformed boundary (e.g., Nakakuki and Mura, 2013, Garel et al., 2014, Sharples et al., 2014, Holt et al., 2015) . In the numerical models of Holt et al. (2015), for example, the slab either lies flat on top of the lower mantle or penetrates through. Either way the boundary between the UM and LM remains undeformed. Holt et al. (2015) constant viscosity values; $10^{20} Pa.s$ for the UM and $5 \cdot 10^{21} Pa.s$ for the LM (the viscosity jump is thus 50).

Also in Garel et al. (2014) the ULM remains stationary. Varying the viscosity jump between 10, 30 or 100 only influences if and how far the slab sinks into the LM, but does not change its stability. Figure 70 gives the evolution of an intra-oceanic subduction model as simulated by Garel et al. (2014). Clearly the ULM boundary remains stationary and the dominant deformation mechanism is merely diffusion creep in the lower mantle. The lowest figures (d) give the underlying computational mesh used for this simulation. As visualized, the mesh is very complex with triangular elements that vary in size over the domain and over time. A detailed mesh is present along the slab, the trench and the ULM boundary. The viscosity jump at the ULM boundary is thus captured in a thin, high resolution area, while in our model it is captured in two elements over 655 to 678 km deep. This could effect the localization of strain along the boundary, as it effects the contact between the SP and OP at the trench (see section 5.2).

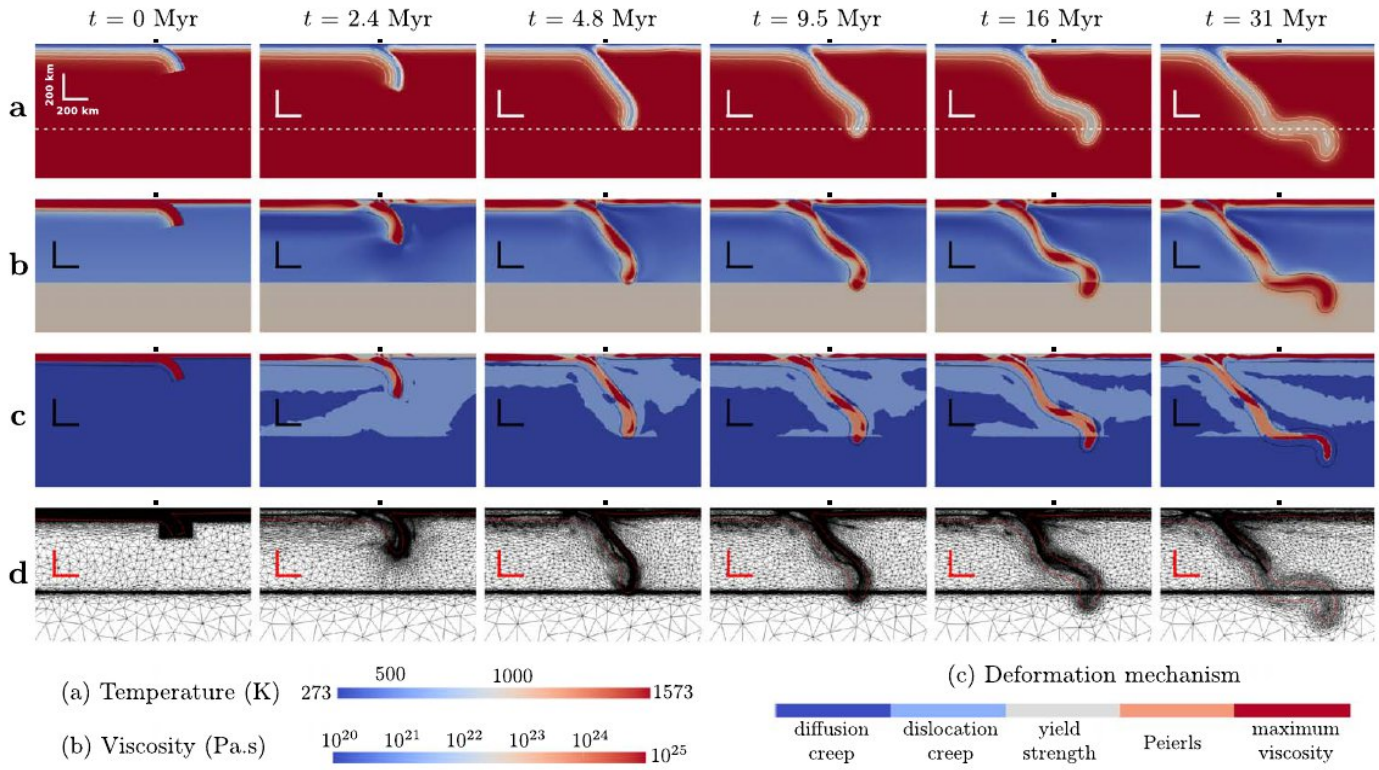

Figure 70: Subduction evolution of a numerical intra-oceanic subduction model by Garel et al., 2014. a) Temperature field, b) viscosity field, c) deformation mechanism, d) computational mesh at varying times (t=0 to t= 31 Myr).

Contrary, Holt et al. (2015) use cubic elements of 5 to 15 km wide for their simulation, which is similar to our setup. They use, however, free slip on the top boundary, causing the elements to remain cubic throughout the run and not vary in shape as the topography changes over time. I have experimented with free slip, but also with free slip does the boundary indent (Figure 67).

Last a temperature gradient is implemented in the mantle and a density contrast is implemented between the UM and LM, both did not solve the problem.

Overall several options have been explored for the behaviour of the ULM boundary. I found that the following features do not cause the deformation of the ULM boundary: the element size, the grid type (squared or triangular), the top boundary (free surface or free slip), the depth of the domain, the viscosity jump (3-100), the rheology (Newtonian, non-Newtonian or constant viscosity), the deformation mechanisms in the LM (only diffusion creep or both diffusion and dislocation creep), the temperature (constant or gradient) and the density (constant or density increase at boundary).

A possible cause can be the high viscosity in and around the slab when approaching the lower mantle. This high viscosity is seen in every run (e.g., run $E_1 1jan$,13, and run $E_1 9apr$, 48). The high viscosity is not only seen inside the slab, but also in the zone of upper mantle material around it. This causes the tip of the slab never to touch the lower mantle but always remain separated by a narrow zone of highly viscous UM material (see e.g., Figure 23). In this zone diffusion creep dominates, which might be the cause for the presence of this highly viscous zone. In the absence of dislocation creep, material cannot easily move aside, and the viscosity in the area increases and the slab tip and its surrounding is able to indent the boundary. Figure 70c) shows that in the model of Garel et al. (2014) dislocation creep dominates in a large part of the upper mantle, especially around the slab. This could thus be a plausible explanation.

Although I have experimented with implementing dislocation creep in the lower mantle, in most of the runs dislocation creep is absent in the lower upper mantle. I have tuned the parameters of the viscosity extensively, but was not able to tune the parameters of the viscosity that dislocation creep would dominate deeper in the mantle for a successful subduction in this setting. A solution would be to include adiabatic heating so the temperature in the deeper mantle will be higher. In this way the parameters of the viscosity can be tuned to lower values and maybe cause dislocation creep to lower the viscosity around the slab approaching the LM.

A last possible solution would be to use a similar material for the subducting plate, overriding plate and upper mantle. In this way there is no boundary between the slab and the surrounding mantle and it will behave in a more similar way. This will be of importance when the slab sinks further into the mantle, towards the lower mantle as it expected to behave in a similar way to the surrounding mantle. This is numerically challenging, though, as it restricts the freedom of tuning the viscous parameters of the lithospheric plates separately to tune successful subduction for example at the hinge.

5.2 Rollback

In section 1, rollback is seen in the successful runs (e.g., run $E_1 1jan$ and run $E_2 6jan$). Rollback is created as soon as the slab starts sinking and continues when the slab hits the lower mantle. In section 1 the OP is a thin oceanic plate with an age (and thus density) gradient towards the trench. Over time this creates a ridge at the side of the domain, causing a ridge push force towards the trench. The OP is free to move, allowing the OP to move with the retreating trench. This, together with the slab pull and ridge force of the SP, promotes subduction and trench retreat in this setup (Figure 16). The plate velocity is slow (roughly 1 cm/yr), which agrees with the observation that slow plates are generally attached to retreating trenches (Faccenna et al., 2007).

In section 2, however, the overriding plate is continental and fixed to the side. The OP is highly viscous throughout so no ridge can form and the OP is unable to move with the trench. No weak zones are implemented so no continental extension can be created within the OP. When the SP is constant in age, subduction can only be created by decoupling of the plates. When the plates are decoupled the trench can retreat and the slab can sink freely. By imposing a wide weak zone mantle material penetrates between the plates to form a back-arc basin and they are decoupled (e.g., run $E_2 9mrch$). During decoupling the slab rolls back up to 250 km in the first few Myr. Hereafter the decoupling stops and, if no plate motion is inserted, the slab breaks off or diffuses out (run E_29mrch and E_7apr, respectively). Only slab pull is thus not enough for the slab to rollback and sink further in our model.

In contrast, Quinquis et al. (2011) created rollback by merely a SP in a upper mantle environment due to slab pull (Figure 71). The SP is of constant thickness and attached to the side boundary, similar to our setup. No OP is present so rollback is only due to the sinking of the gravitational unstable slab. This shows that our slab should thus theoretically be able to sink without further forces involved. I have experimented in several ways to create further decoupling. I decreased the size of the elements to increase the effect of the weak OC (run E_5apr) and alternated the viscosity of the SP in several ways (section 4.2.7). These experiments, however, did not result in an increase of rollback and decoupling remained limited.

A possible explanation for the limited decoupling is the presence of a small wedge of continental crust material that gets trapped between the back-arc basin and the subducting plate (Figure 56), resisting further retreat when returnflow velocities have decreased. When the OP is left out (run E_2may, Figure 67), however, a crustal wedge of oceanic material forms instead, and the same problem occurs. Comparing this run to the result of Quinquis et al. (2011), no crustal wedge forms in their model and the trench is able to roll back. Additionally, Quinquis et al. (2011) showed that a weak oceanic crust is necessary for substantial rollback (Figure 71), as it promotes decoupling at the surface. In his model an oceanic crust of a single element is already enough to create rollback. Increasing our element size further would thus not make a difference. Instead the properties of the oceanic and continental crust should be analyzed further so this crustal wedge is prevented from forming and decoupling can continue.

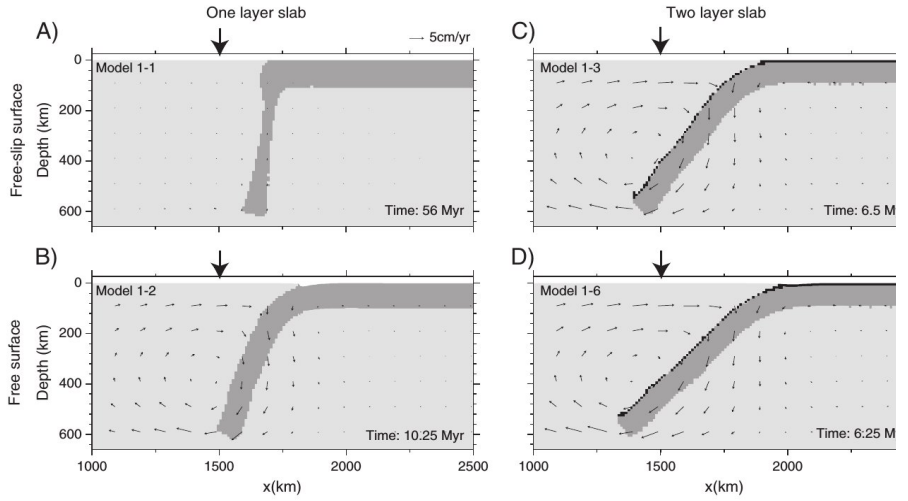

Figure 71: Model results of Quinquis et al. (2011). A) One layer lithosphere with a free-slip surface, B) one layer lithosphere with free surface, C) two later lithosphere with free-slip surface and D) two layer lithosphere with free surface. Black arrows at surface represent the initial position of the trench. Time required to reach a depth of 600 km is shown in the lower right corner.

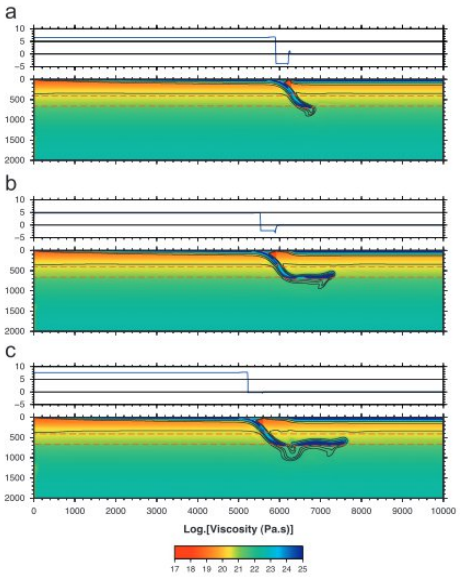

Figure 72: Evolution of subduction model of Nakakuki and Mura (2013), with a continental OP fixed at the right boundary and an implemented weak zone. a) 19.0 Myr, b) 32.3 Myr, c) 52.1 Myr. The top graph gives the surface velocity.

Nakakuki and Mura (2013) created a comparable setup to setup 2 with a fixed continental OP and a weak zone between the OP and SP. Figure 72 gives the result of one of their runs. This setup results in a back-arc basin where mantle material penetrates close to the surface, similar to our result. Extension in the OP, however, starts when the slab hits the lower mantle around 20 Myr, where after rollback starts. Instead of immediate detachment and rollback as in our model, rollback is triggered by interaction with the lower mantle.

To promote further subduction towards the lower mantle I added a ridge push force to the system by implementing a shallow age gradient through the SP (run e.g., E_21apr), similar to setup 1 and to the setup of Nakakuki and Mura (2013). With the additional ridge push force, subduction is able to continue towards the lower mantle, without the necessity of rollback. As seen in run E_21apr (Figure 52), the trench retreats a similar distance in the first few Myr as former runs, where after it remains stationary as subduction continues. A stationary trench is expected as the ridge push causes an opposite motion of the SP, inhibiting rollback (e.g., Figure 53). A similar result is obtained by Quinquis et al. (2011) and Nakakuki and Mura (2013). The formation of the ridge causes a convection cell to form between the SP, the slab and the underlying mantle. This type of convection cell is observed by other authors that created a mobile SP by either including a ridge, a free SP or an inserted plate motion (e.g., Holt et al., 2015, Garel et al., 2014, Billen, 2008).

Compared to the results of section 1 and of the models of Nakakuki and Mura (2013), I thus expect rollback to form on the interaction with the lower mantle. However, instead of rollback, the trench remains stationary and no rollback is created. This inhibits the slab to flatten on top of the lower mantle and instead the angle of subduction increases. As the ULM boundary is impermeable, the velocities in the slab decrease, its viscosity increases and subduction ceases (e.g., run E_21apr). This same behaviour is seen when the OP is detached from the side boundary so it is free to move (run E_30apr). Although no back-arc basin forms, similar to setup 1, the slab approaches the LM under a high angle and subduction ceases when the tip of the slab indents the ULM boundary. Only in run E_1may does subduction continue. For this setup the OP is free to move, but also a wide back-arc basin is implemented, causing initial rollback to form like in run E_27apr but also imposing a push force from the OP on the trench. With this setup the slab is bend far enough that it approaches the LM in a more horizontal position, enabling the slab to move on top of the LM and for subduction to continue. Further rollback is, however, still not observed and the trench remains locked.

Our successful runs are thus merely limited to setups where the slab is able to lay flat on top of the LM (run E_11jan, E_26jan and E_1may).

It has been shown (e.g., Garel et al., 2014, Stegman et al. (2010)) that the interaction of the slab tip with the ULM mantle is strongly coupled to trench motion. the impermeability of the lower mantle together with the high viscosity of the slab tip can thus strongly influence the behaviour of the trench and vice versa. This recurring problem might thus be a cause of the observed trench locking.

Overall the disability of the subducting plate to continue to decouple from the surface has great influence on the dynamics of our subduction models. Driven merely by slab pull, subduction is only possible until rollback ceases after roughly 200 km. With additional ridge push forces the slab is able to continue to sink until it reaches the lower mantle. For subduction to continue the trench must be able to retreat, which is inhibited. It is thus of great importance to find the cause of this trench locking in further research. A thorough investigation should be done on the rheological parameters of the SP and the surrounding mantle, as they are the likely cause of this trench locking. Apparently the behaviour of the subducting plate, especially that of the oceanic crust causes a crustal wedge to form which seems to locks the rollback. Additionally, the slab stiffens deep in the mantle, unable to penetrate through the ULM boundary, which strongly effects the trench motion.

Additionally, I found that the properties (continental or oceanic, thick or thin) and motion of the OP seem to have a strong effect on the slab dynamics and trench motion. A free movable OP promotes rollback and subduction, while a fixed OP resists rollback. The importance of the OP has been confirmed by several authors and thorough research has been done on the effect of the OP on slab dynamics (e.g., Holt et al., 2015, Nakakuki and Mura, 2013, Garel et al., 2014).

5.3 Oscillations

To stabilize the free surface, the FSSA technique created by Kaus et al. (2010) is implemented. However, as observed in several models (e.g., run E_Garel, E_2apr and E_1may), the surface remains sensitive to oscillations. These oscillations are observed when the mantle material has reached the surface and the overall velocity has decreased (caused by the slab reaching the lower mantle). As the time step is dependent on the velocity (equation 30) the time step increases with decreasing velocity. In this case the time steps exceed the maximum time step for the surface to remain stable and oscillations start. This effect is not seen when no back-arc basin forms (e.g., run E_26jan and run E_30apr) or when the slab does not reach the lower mantle (run E_30mrch). The oscillations are thus created by the combination of mantle material at the surface and the decrease in overall velocity due to the resistance of the lower mantle. The oscillations always start in the back-arc basin. This is expected as the surface is most sensitive here to instabilities as motion is observed in opposing directions (Figure 58).

The quasi-implicit scheme of Kaus et al. (2010) implemented in our code is thus not able to stabilize the surface. Rose et al. (2017) created a different approach to stabilize the surface; using a non-standard finite difference scheme. This scheme allows for large stable time steps and thus might be more appropriate for our setup. In further research this method could be implemented. A downside of this method is, however, that the accuracy of the result will be decreased. At what magnitude this will be is unknown, but it should be taken into account when implementing this scheme.

5.4 Viscosity

5.4.1 Mantle rheology

Overall our used parameters fit within the obtained values by laboratory experiments and values used by other numerical models (see table 1 and 2). However, the values for activation volume, V slightly differ from other numerical models. This could be due to the constant temperature of $1300°C$ of the mantle. The viscosity is dependent on the temperature (equation 28) and thus a decrease in temperature causes an increase in viscosity. This is compensated in our model by decreasing the activation volume (V), which gives the viscosity gradient with pressure (depth, see equation 2).

With the use of these values a viscosity profile is obtained which is similar to the viscosity profile obtained by Čížková et al. (2012) (Figure 21). The viscosity profile of Čížková et al. (2012) is, however, one dimensional so does not take lateral variations into account. These lateral variations include subducting slab and its effect on the surrounding mantle (mostly due to dislocation creep). In our models we have seen that dislocation creep can locally decrease the viscosity in the mantle surrounding the slab (e.g., run E_26apr). Implementing dislocation creep as a deformation mechanism in the lower mantle also causes the viscosity of the LM to locally decrease where the tip of the slab approaches the LM (e.g., run E_10feb). This is to be expected as dislocation creep is dependent on stress and is comparable to results of other numeral models. In Garel et al. (2014) dislocation creep is the dominant deformation

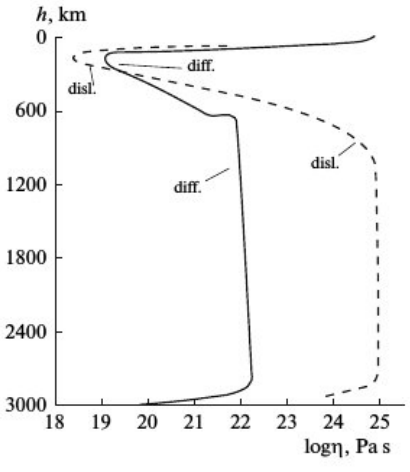

Figure 73: Radial viscosity profile generated by diffusion creep (solid line) and diffusion creep (dashed line). From Trubitsyn (2012).

mechanisms in a wide area around the subducting slab in the upper mantle,
while in our models this region is more confined. Especially when the slab hits the lower mantle, and velocities decrease, does diffusion creep take over from dislocation creep (e.g., Figure 23 and 50). This is proposed as a possible cause of the high stiffness in and around the sinking slab and the inability for the slab to sink into the LM.

When plate motion is implemented in our models (as an imposed velocity, by ridge push, or by a free movable plate), dislocation creep lowers the viscosity in the uppermost mantle below the lithosphere (e.g., run E_26jan, E_18apr and E_1may). When there is no motion in the lithosphere (e.g., when the continental OP is fixed to the side boundary, run E_26apr), little dislocation creep dominates directly underneath the plate (Figure 50). This is expected as plate motion causes friction with the underlying mantle, increasing the strain and the strain rate (e.g., Figure 47), lowering the viscosity caused by dislocation creep. This upper mantle low viscosity zone (LVZ), known as the asthenosphere, has been recognized beneath oceanic and tectonically active regions by seismological research showing a low velocity zone at depths of 100-300 km (e.g., Hales et al., 1968) and by microphysical observations/research on geoid and post-glacial rebound data (Richards et al., 2001). It is consistent with the radial viscosity profiles generated by Čížková et al. (2012) and others (Figures 6 and 21). The dominance of dislocation creep in this LVZ is shown by the numerical experiments of Trubitsyn (2012), as presented in Figure 73.

5.4.2 Slab rheology

In all our models the lithospheric plates are highly viscous (up to 10^{25} Pa.s) and as long as they remain on the surface the viscosity remains high throughout the run. The lithospheric mantle reaches and remains at maximum viscosity, while the crust is little less viscous due to the lower yield strength of the material (e.g., Figure 50) and varies slightly through time. This is consistent with the low temperature and strain rate of the plates and is consistent with observations (Figure 6 and other numerical models (e.g., Billen and Hirth, 2007, Stegman et al., 2010, Holt et al., 2015).

The initially subducted slab in our model is also highly viscous as it has a similar temperature profile as the plate at the surface (equation 17). In all our runs, the tip of the slab remains at maximum viscosity, maintaining its prescribed curved shape (e.g., Figure 50). This shape is more notable in the results of section 2 as the initial angle is 90°compared to 77°in section 1. Holt et al. (2015) also prescribed an initial curved shape of the slab until an angle of 90 °, however, this prescribed shape disappears as soon as the slab sinks. Holt et al. (2015) prescribed, however, a maximum viscosity of only $10^{23}Pa.s$ to the slab, two orders of magnitude lower than the viscosity of our slab. This causes the slab to be more easily deformed. In further research the initial temperature profile of the slab should be increased as the tip of the slab is already at a depth of 150 km when the run starts. A higher temperature will be more realistic and will probably decrease the viscosity at the tip and prevent the initial shape to remain present. Additionally, if the tip becomes less stiff,this might also influence the interaction with the lower mantle.

Beside the tip of the slab, the interior of the body of the slab also remains on maximum viscosity as it sinks. This high viscosity is expected as the interior of the slab is cold and viscosity increases exponential with decreasing temperature (equation 28). As the upper mantle is relatively cold and diffusion creep dominates deeper in the upper mantle around the slab, this high viscosity remains in the slab. This is in agreement with with other dynamic models that use the experimental flow laws (e.g., Čížková et al., 2002, Billen and Hirth, 2007, Garel et al., 2014). As shown in Figure 72, a highly viscous slab is also observed by Nakakuki and Mura (2013), especially when the slab hits the ULM boundary. Additionally, Billen and Hirth (2007) states that although weak slabs are more in agreement with geophysical observations, stiff slabs are better in predicting plate motions and easier to numerically model.

Figure 70b shows the viscosity field obtained by Garel et al. (2014). Similar to our result, the slab interior also reaches maximum viscosity. However, the presence of Peierls creep causes the viscosity to decrease locally at the bending points and the slab lays flat on the ULM boundary. Although Peierls creep does decrease the viscosity in our slab to a certain degree, our slabs are significantly stiffer and bending is less easily created. Especially when the slab approaches the LM under a high angle is the viscosity of the slab very high (e.g., run E_30apr, figure 60) and is the effect of Peierls creep minimal. As the slab is unable to penetrate through the ULM boundary and unable to bend, subduction ceases. Folding of the slab is only observed when an additional force in the form of an imposed SP velocity, is implemented (run E_18apr, figure 46).

When the slab approaches the LM in a more shallow angle, however, Peierls creep does decrease the viscosity locally in the slab, and some bending is observed as it sinks in the UM (e.g., run E_11jan). Closer to the surface, yielding takes over Peierls creep, which is consistent with the definitions of both deformation mechanisms (section 2). When the SP and OP are connected, yielding causes the viscosity to decrease at the contact zone between the plates, creating a low viscosity zone that makes it possible for the slab to move along the OP down into the mantle (e.g., Figure 23). With the presence of Peierls creep, yielding is only the dominant deformation mechanism in this low viscosity zone and in the weak oceanic crust before Peierls creep takes over.

In setup 2, however, the presence of these strain localizing deformation mechanisms cause slab break-off at the hinge. This is observed in e.g., run E_29mrch (Figure 35), where the SP is constant in age and the OP is continental. By leaving out Peierls creep as a deformation mechanism (run E_6apr), we found that this prevents break-off and is thus the main cause of this break-off. Without an additional ridge push force, however, the slab is still unable to sink further. Even without the presence of Peierls creep it thus seems that only slab pull is not enough to create successful subduction as seen in the model of Quinquis et al. (2011) by Quinquis et al. (2011). By implementing a ridge push force in the form of an imposed velocity (run E_18apr) or the implementation of a ridge (run E_21apr), subduction was able to continue until the ULM boundary. This force thus appears crucial, which is consistent to the result of Garel et al. (2014). Without the presence of Peierls creep, however, the subducting slab appeared stiff and highly viscous (Figure 54). Implementing Peierls creep we found that the additional force of the ridge push prevented slab break-off at the hinge and the slab sunk as far as the ULM boundary. The presence of Peierls creep caused the viscosity and the stiffness of the slab to decrease, as seen in Figure 55 (run E_27apr).

Apart from the chance of break-off at the hinge, the presence of Peierls creep is thus of great importance for the behaviour of the slab. Without Peierls creep the slab is extremely stiff and will not bend as the slab sinks, while the presence of Peierls creep causes the slab to bend while it sinks. Compared to the result of Garel et al. (2014) (Figure 70), our slab bending is, however, still limited. For further research the the rheological parameters of Peierls creep should be further investigated.

Instead of implementing Peierls creep, other authors (e.g., Billen and Hirth, 2007) used yield strength as a weakening mechanism in the mantle. By decreasing the maximum yield strength, deformation could be accommodated by plastic deformation in the mantle. Garel et al. (2014) experimented with various maximum yield strengths and found that a maximum yield strength as low as 300 MPa is needed to obtain similar subduction dynamics as when Peierls creep is implemented. Additionally, it has been stated that yield strength is merely dominant for shallow depths (see section 2). Experimenting with a decreased yield strength as a weakening mechanism is thus an option for further research, but not preferred.

Overall, the experimental flow laws result in a plausible viscosity field. It has been shown that Peierls creep is an important deformation mechanism in the slab and should tuned to increase its effect on the flexibility of the slab. Additionally. dislocation creep should be more dominant in the upper mantle, especially around the slab. To achieve this, fine tuning of the rheological parameters of Peierls creep and dislocation is necessary.

5.5 Further research

To be able to use ELEFANT to investigate the dynamics of subduction of the Sandwich Trench, some crucial problems have to be fixed first.

Firstly, the boundary between the upper and lower mantle should be properly defined. It should be investigated why the ULM boundary is deformable and does not remain fixed on a horizontal position. Then it should be investigated why the boundary is impermeable and how a permeable or semi-permeable boundary can be created. This is probably closely linked to the rheological parameters imposed on the various materials and the temperature field prescribed and these should be thoroughly investigated.

Secondly, the SP should be able to decouple from the surface and create full rollback when detached from the OP. To do so the crustal wedge at the trench should be further investigated, as this might be the cause of the obstruction of further rollback. Additionally, the rheological parameters of the SP and the oceanic crust should be investigated further, as they are likely to have a strong effect on this trench locking.

Last, the surface oscillations have to be prevented. One option is to use the stabilization approach of Rose et al. (2017) instead of Kaus et al. (2010).

If these problems are fixed, attempts can be made to reconstruct the evolution of the Sandwich Trench as mentioned in the introduction. Comparing the obtained slab evolution to the proposed slab styles could support their proposed regime diagrams or counteract their conclusions based on this geological supported reconstruction. It can also put constrains on the rheological parameters and the properties of the weak zone needed to construct such a slab evolution.

6 Conclusions

In this research I aimed to create a fully functioning two-dimensional numerical subduction subduction model in the finite element code ELEFANT, with as final goal to simulate a subduction model representing the evolution of the South Sandwich subduction zone as it was reconstructed by Kosters et al., 2015. As I ran into multiple unexpected problems along the way, I was not able to create a fully functioning subduction model and the final goal was not reached. Instead this thesis describes our journey through two-dimensional subduction modelling and discusses various runs and the problems I were faced with. Last, I proposed possible solutions for these problems for further research.

In section 1 of this research an intra-oceanic subduction system was created with a setup similar to that of Garel et al., 2014. By the creating of ridges on both the SP and the OP I was able to create a subduction evolution where the SP sinks below the OP while rolling back. When hitting the ULM boundary, the slab flattened on top of the ULM boundary and deforming it as it does. I was able to implement a velocity on the side which accelerated the subduction velocity and altered the style of subduction.

In the section 2 an ocean-contental subduction system, similar to a two-dimensional representation of the South Sandwich system was created. As the OP is continental, a ridge was unable to form in the OP so subduction could only evolve if the SP would detach from the OP. The detachment was created by implementing a wide low viscosity zone between the SP and OP. This allowed mantle material to flow towards the surface between the plates, causing the slab to sink and the trench to roll back in the first few Myrs. After a maximum of 250 km, however, rollback ceased and further subduction was prevented.

The only way to promote further subduction was by adding a ridge push force to the SP by implementing an age gradient towards the trench. This caused subduction to continue, but without further motion of the trench. Research has to be done to be investigate this trench locking and create further rollback.

This trench locking could possibly be linked to the behaviour of the ULM boundary when our slab approaches the LM. Instead of penetrating through the ULM boundary or lying flat on top of the ULM boundary, our slab indents the boundary. When the slab approaches the ULM from a steep angle this causes subduction to cease, while a lower angle forces the slab to flatten on top of the ULM boundary, deforming it as it does. In both situations does the slab never touch the LM, a narrow zone of highly viscous UM material always remains in between, which could be the cause of the problem. Tuning the rheological properties of the slab and the upper and lower mantle so far did not change this phenomenon and more research is needed to find the solution to this problem. A solution would be to change the temperature field, which is strongly correlated with the rheological parameters. Additionally, dislocation creep should be present deeper in the mantle, which could prevent this narrow zone of highly UM material to be present between the slab and the LM.

Another problem which has to be tackled is the destabilization of the surface. This destabilization is seen in some runs at the surface near the trench where the mantle material hits the surface and the overall velocity is low. An option is to implement a new stabilization technique of Rose et al., 2017.

Last, I experimented with the effect of Peierls creep, the deformation mechanism believed to be dominant at high strain and low temperatures. Clearly without implementing this mechanism, the slab was significantly more viscous and was unable to change shape as it sank. However, the absence of Peierls creep does prevent slab break-off at the hinge as it prevents the viscosity to decrease fast on places where strain localizes. Apart from this, Peierls creep is an essential deformation mechanism for subduction systems as it allows for deformation of the slab as it sinks. More research thus has to be done to correctly implement Peierls creep without hinge break-off at the hinge.

Overall, although I have created reasonably functioning two-dimensional numerical subduction systems, some essential problems remain which have to be solved before a proper two-dimensional numerical subduction system can be created. Only then we can be able to correctly simulate the evolution of the South Sandwich Trench.

7 Acknowledgements

I would like to thank my supervisor dr. Cedric Thieulot for all his help during my thesis, for inaugurating me in the world of subduction modelling and for using his code for this project. Secondly, I would like to thank prof. dr. Wim Spakman for his help, input and enthusiasm during my thesis. I would like to thank dr. Hana Cizkova for commenting on my thesis and for her suggestions for further work. She made me realize that not obtaining a fully functioning model is not a failure but is just a first year PhD in subduction modelling. Last, I would like to thank my fellow master students for their daily support and my friends and family for their mental support when I needed it. Without these people this thesis will not have been completed.

8 References

[1] P.R. Amestoy et al. "MUMPS: a general purpose distributed memory sparse solver". In: *International Workshop on Applied Parallel Computing*. Springer. 2000, pp. 121–130.

[2] A.Y. Babeyko and S.V. Sobolev. "High-resolution numerical modeling of stress distribution in visco-elasto-plastic subducting slabs". In: *Lithos* 103.1 (2008), pp. 205–216.

[3] M. Baes, R. Govers, and R. Wortel. "Subduction initiation along the inherited weakness zone at the edge of a slab: Insights from numerical models". In: *Geophysical Journal International* 184.3 (2011), pp. 991–1008.

[4] S. Beauchesne and J.P. Poirier. "In search of a systematics for the viscosity of perovskites: creep of potassium tantalate and niobate". In: *Physics of the earth and planetary interiors* 61.3-4 (1990), pp. 182–198.

[5] M.I. Billen. "Modeling the dynamics of subducting slabs". In: *Annu. Rev. Earth Planet. Sci.* 36 (2008), pp. 325–356.

[6] M.I. Billen and G. Hirth. "Rheologic controls on slab dynamics". In: *Geochemistry, Geophysics, Geosystems* 8.8 (2007).

[7] M. Chertova, W. Spakman, and M. Faccenda. "Predicting SKS-splitting from 35 Myr of subduction and mantle flow evolution in the western Mediterranean". In: *EGU General Assembly Conference Abstracts*. Vol. 19. 2017, p. 12362.

[8] H. Čížková et al. "The viscosity of Earth's lower mantle inferred from sinking speed of subducted lithosphere". In: *Physics of the earth and Planetary Interiors* 200 (2012), pp. 56–62.

[9] H. Čızková et al. "The influence of rheological weakening and yield stress on the interaction of slabs with the 670 km discontinuity". In: *Earth and Planetary Science Letters* 199.3 (2002), pp. 447–457.

[10] W. Dai and R. Nassar. "A finite difference scheme for solving the heat transport equation at the microscale". In: *Numerical Methods for Partial Differential Equations* 15.6 (1999), pp. 697–708.

[11] I.W.D. Dalziel et al. "The Scotia Arc: genesis, evolution, global significance". In: *Annual Review of Earth and Planetary Sciences* 41 (2013), pp. 767–793.

[12] Thieulot C. De Laat J.I. "Towards a two-dimensional numerical subduction model". In: *Guided Research* Utrecht University (2016).

[13] Y.H.P. Djomani et al. "The density structure of subcontinental lithosphere through time". In: *Earth and Planetary Science Letters* 184.3 (2001), pp. 605–621.

[14] D.C. Drucker and W. Prager. "Soil mechanics and plastic analysis or limit design". In: *Quarterly of applied mathematics* 10.2 (1952), pp. 157–165.

[15] G. Eagles et al. "Tectonic evolution of the west Scotia Sea". In: *Journal of Geophysical Research: Solid Earth* 110.B2 (2005).

[16] M. Faccenda et al. "Fault-induced seismic anisotropy by hydration in subducting oceanic plates". In: *Nature* 455.7216 (2008), pp. 1097–1100.

[17] C. Faccenna et al. "Predicting trench and plate motion from the dynamics of a strong slab". In: *Earth and Planetary Science Letters* 257.1 (2007), pp. 29–36.

[18] D. Forsyth and S. Uyeda. "On the relative importance of the driving forces of plate motion". In: *Geophysical Journal International* 43.1 (1975), pp. 163–200.

[19] A.M. Forte and J.X. Mitrovica. "New inferences of mantle viscosity from joint inversion of long-wavelength mantle convection and post-glacial rebound data". In: *Geophysical Research Letters* 23.10 (1996), pp. 1147–1150.

[20] F. Garel et al. "Interaction of subducted slabs with the mantle transition-zone: A regime diagram from 2-D thermo-mechanical models with a mobile trench and an overriding plate". In: *Geochemistry, Geophysics, Geosystems* 15.5 (2014), pp. 1739–1765.

[21] T. Gerya. *Introduction to numerical geodynamic modelling*. Cambridge University Press, 2009.

[22] C. Goetze and B. Evans. "Stress and temperature in the bending lithosphere as constrained by experimental rock mechanics". In: *Geophysical Journal International* 59.3 (1979), pp. 463–478.

[23] M. Gurnis, C. Hall, and L. Lavier. "Evolving force balance during incipient subduction". In: *Geochemistry, Geophysics, Geosystems* 5.7 (2004).

[24] A.L. Hales et al. "P-wave station anomalies and the structure of the upper mantle". In: *Journal of Geophysical Research* 73.12 (1968), pp. 3885–3896.

[25] C.E. Hall et al. "Catastrophic initiation of subduction following forced convergence across fracture zones". In: *Earth and Planetary Science Letters* 212.1 (2003), pp. 15–30.

[26] G. Hirth and D. Kohlstedt. "Rheology of the upper mantle and the mantle wedge: A view from the experimentalists". In: *Inside the subduction Factory* (2003), pp. 83–105.

[27] A.F. Holt, T.W. Becker, and B.A. Buffett. "Trench migration and overriding plate stress in dynamic subduction models". In: *Geophysical Journal International* 201.1 (2015), pp. 172–192.

[28] E. Ito and H. Sato. "Aseismicity in the lower mantle by superplasticity of the descending slab". In: *Nature* 351.6322 (1991), pp. 140–141.

[29] M. Kameyama, D.A. Yuen, and S.-I. Karato. "Thermal-mechanical effects of low-temperature plasticity (the Peierls mechanism) on the deformation of a viscoelastic shear zone". In: *Earth and Planetary Science Letters* 168.1 (1999), pp. 159–172.

[30] S.-I. Karato. *Deformation of earth materials: an introduction to the rheology of solid earth*. Cambridge University Press, 2012.

[31] S.-I. Karato. "Rheology of the deep upper mantle and its implications for the preservation of the continental roots: A review". In: *Tectonophysics* 481.1 (2010), pp. 82–98.

[32] S.-I. Karato and H. Jung. "Effects of pressure on high-temperature dislocation creep in olivine". In: *Philosophical Magazine* 83.3 (2003), pp. 401–414.

[33] S.-I. Karato and D.C. Rubie. "Toward an experimental study of deep mantle rheology: a new multianvil sample assembly for deformation studies under high pressures and temperatures". In: *Journal of Geophysical Research: Solid Earth* 102.B9 (1997), pp. 20111–20122.

[34] S.-I. Karato and P. Wu. "Rheology of the upper mantle: A synthesis". In: *Science* 260.5109 (1993), pp. 771–778.

[35] S.-I. Karato, S. Zhang, and H.-R. Wenk. "Superplasticity in Earth's Lower Mantle: Evidence from Seismic Anisotropy". In: *Science* 270 (1995), p. 20.

[36] B.J.P. Kaus, H. Mühlhaus, and D.A. May. "A stabilization algorithm for geodynamic numerical simulations with a free surface". In: *Physics of the Earth and Planetary Interiors* 181.1 (2010), pp. 12–20.

[37] T. Kawazoe et al. "Shear deformation of dry polycrystalline olivine under deep upper mantle conditions using a rotational Drickamer apparatus (RDA)". In: *Physics of the Earth and Planetary Interiors* 174.1 (2009), pp. 128–137.

[38] S. Kim and S.J. Karrila. *Microhydrodynamics: principles and selected applications*. Courier Corporation, 2013.

[39] J. Korenaga and S.-I. Karato. "A new analysis of experimental data on olivine rheology". In: *Journal of Geophysical Research: Solid Earth* 113.B2 (2008).

[40] M. Kosters et al. "South-Sandwich subduction initiated without plate convergence". In: *Master Thesis* Utrecht University (2015).

[41] K. Lambeck and P. Johnston. "The viscosity of the mantle: evidence from analyses of glacial rebound phenomena". In: *The Earth's Mantle: Composition, Structure, and Evolution* (1998), pp. 461–502.

[42] L. Li et al. "Deformation of olivine at mantle pressure using the D-DIA". In: *European Journal of Mineralogy* 18.1 (2006), pp. 7–19.

[43] P. Li, S.-I. Karato, and Z. Wang. "High-temperature creep in fine-grained polycrystalline CaTiO3, an analogue material of (Mg, Fe) SiO3 perovskite". In: *Physics of the earth and planetary interiors* 95.1-2 (1996), pp. 19–36.

[44] M. Maffione et al. "Dynamics of intraoceanic subduction initiation: 1. Oceanic detachment fault inversion and the formation of supra-subduction zone ophiolites". In: *Geochemistry, Geophysics, Geosystems* 16.6 (2015), pp. 1753–1770.

[45] D.P. McKenzie. "The initiation of trenches". In: *Island arcs, deep sea trenches and back-arc basins* (1977), pp. 57–61.

[46] C. Meade, P.G. Silver, and S. Kaneshima. "Laboratory and seismological observations of lower mantle isotropy". In: *Geophysical Research Letters* 22.10 (1995), pp. 1293–1296.

[47] J.X. Mitrovica and A.M. Forte. "A new inference of mantle viscosity based upon joint inversion of convection and glacial isostatic adjustment data". In: *Earth and Planetary Science Letters* 225.1 (2004), pp. 177–189.

[48] T. Nakakuki and E. Mura. "Dynamics of slab rollback and induced back-arc basin formation". In: *Earth and Planetary Science Letters* 361 (2013), pp. 287–297.

[49] K. Nikolaeva, T.V. Gerya, and F.O. Marques. "Subduction initiation at passive margins: numerical modeling". In: *Journal of Geophysical Research: Solid Earth* 115.B3 (2010).

[50] W.R. Peltier. "Global sea level rise and glacial isostatic adjustment". In: *Global and Planetary Change* 20.2 (1999), pp. 93–123.

[51] A. Putnis. *An introduction to mineral sciences*. Cambridge University Press, 1992.

[52] M.E.T. Quinquis and S.J.H. Buiter. "Testing the effects of basic numerical implementations of water migration on models of subduction dynamics". In: *Solid Earth* 5.1 (2014), p. 537.

[53] M.E.T. Quinquis, S.J.H. Buiter, and S. Ellis. "The role of boundary conditions in numerical models of subduction zone dynamics". In: *Tectonophysics* 497.1 (2011), pp. 57–70.

[54] G. Ranalli. "Mantle rheology: radial and lateral viscosity variations inferred from microphysical creep laws". In: *Journal of Geodynamics* 32.4 (2001), pp. 425–444.

[55] G. Ranalli. "The microphysical approach to mantle rheology". In: *Glacial isostasy, sea-level and mantle rheology*. Springer, 1991, pp. 343–378.

[56] G. Ranalli and B. Fischer. "Diffusion creep, dislocation creep, and mantle rheology". In: *Physics of the earth and planetary interiors* 34.1-2 (1984), pp. 77–84.

[57] M.A. Richards et al. "Role of a low-viscosity zone in stabilizing plate tectonics: Implications for comparative terrestrial planetology". In: *Geochemistry, Geophysics, Geosystems* 2.8 (2001).

[58] I. Rose, B. Buffett, and T. Heister. "Stability and accuracy of free surface time integration in viscous flows". In: *Physics of the Earth and Planetary Interiors* 262 (2017), pp. 90–100.

[59] L.H. Royden and L. Husson. "Trench motion, slab geometry and viscous stresses in subduction systems". In: *Geophysical Journal International* 167.2 (2006), pp. 881–905.

[60] W.P. Schellart. "Kinematics and flow patterns in deep mantle and upper mantle subduction models: Influence of the mantle depth and slab to mantle viscosity ratio". In: *Geochemistry, Geophysics, Geosystems* 9.3 (2008).

[61] H. Schmeling et al. "A benchmark comparison of spontaneous subduction models—Towards a free surface". In: *Physics of the Earth and Planetary Interiors* 171.1 (2008), pp. 198–223.

[62] G. Schubert. *Treatise on geophysics*. Elsevier, 2015.

[63] W. Sharples et al. "Overriding plate controls on subduction evolution". In: *Journal of Geophysical Research: Solid Earth* 119.8 (2014), pp. 6684–6704.

[64] D.R. Stegman et al. "A regime diagram for subduction styles from 3-D numerical models of free subduction". In: *Tectonophysics* 483.1 (2010), pp. 29–45.

[65] B. Steinberger and A.R. Calderwood. "Models of large-scale viscous flow in the Earth's mantle with constraints from mineral physics and surface observations". In: *Geophysical Journal International* 167.3 (2006), pp. 1461–1481.

[66] R.J. Stern and S. H. Bloomer. "Subduction zone infancy: examples from the Eocene Izu-Bonin-Mariana and Jurassic California arcs". In: *Geological Society of America Bulletin* 104.12 (1992), pp. 1621–1636.

[67] R.L. Stocker and M.F. Ashby. "On the rheology of the upper mantle". In: *Reviews of Geophysics* 11.2 (1973), pp. 391–426.

[68] C. Thieulot. "ELEFANT: a user-friendly multipurpose geodynamics code." In: *Solid Earth Discussions* 6.2 (2014).

[69] C. Thieulot. "FANTOM: Two-and three-dimensional numerical modelling of creeping flows for the solution of geological problems". In: *Physics of the Earth and Planetary Interiors* 188.1 (2011), pp. 47–68.

[70] C. Thieulot. *Manual ELEFANT*. Utrecht University, 2016.

[71] N. Tosi et al. "A community benchmark for viscoplastic thermal convection in a 2-D square box". In: *Geochemistry, Geophysics, Geosystems* 16.7 (2015), pp. 2175–2196.

[72] J. Toth and M. Gurnis. "Dynamics of subduction initiation at preexisting fault zones". In: *Journal of Geophysical Research B* 103.B8 (1998), pp. 18053–18067.

[73] V.P. Trubitsyn. "Rheology of the mantle and tectonics of the oceanic lithospheric plates". In: *Izvestiya Physics of the Solid Earth* 48.6 (2012), pp. 467–485.

[74] D.L. Turcotte and G. Schubert. *Geodynamics*. Cambridge University Press, 2002.

[75] D.L. Turcotte, W.F. Haxby, and J.R. Ockendon. "Lithospheric instabilities". In: *Island arcs, deep sea trenches and back-arc basins* (1977), pp. 63–69.

[76] Z. Wang and S. Ji. "Diffusion creep of fine-grained garnetite: Implications for the flow strength of subducting slabs". In: *Geophysical Research Letters* 27.15 (2000), pp. 2333–2336.

A Appendices

A.1 Movies

The following movies contain additional visualization of the nummerical subduction systems as they are presented in sections 4.1 and 4.2.

A.1.1 Movie E_11jan

A.1.2 Movie $tuningUMandLMviscosity$

A.1.3 Movie E_19jan

A.1.4 Movie E_3feb

A.1.5 Movie E_7apr

A.1.6 Movie E_11apr

A.1.7 Movie E_19apr

A.1.8 Movie E_21apr

A.1.9 Movie E_27apr

A.1.10 Movie E_30apr

A.1.11 Movie E_1may